Dispersions and Solutions of Single Walled Carbon Nanotubes

By

Shane D Bergin

A thesis submitted for the degree of
Doctor of Philosophy
in the University of Dublin.

School of Physics,
Trinity College Dublin,

2008
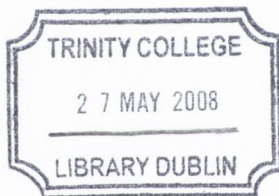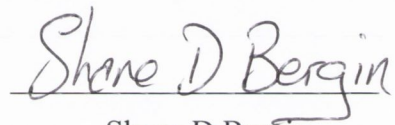
Declaration

I declare that the work in this thesis has not been previously submitted as an exercise for a degree to this or any other university.

The work described herein is entirely my own, except for the assistance mentioned in the acknowledgements and the collaborative work mentioned in the list of publications.

I agree that Trinity College Library may lend or copy this thesis on request.

Shane D Bergin

to my parents, brothers
& grandparents

Between my finger and my thumb
The squat pen rests.
I'll dig with it.

Digging
Seamus Heaney

In all affairs it's a healthy thing now and then to hang a question mark on the things you have long taken for granted.

Bertrand Russell

Life is like a cup of tea: it's how you make it

Anon.

Abstract

Large scale exfoliation of single walled carbon nanotubes (SWNTs) has been shown in various media. Debundling of SWNTS has been demonstrated by dilution of nanotube dispersions. On making the initial dispersions, large aggregates (~100s of microns) are removed by a mild centrifugation step resulting in an isotropic phase containing bundles of nanotubes. The root mean square bundle diameter, of bundles in this isotropic phase, has been shown to be concentration dependent. Such debundling has been demonstrated in the solvents N-methyl-2-pyrrolidone (NMP) and for the narcotic drug γ-Butyrolactone, sometimes referred to as 'liquid ecstasy'. After centrifugation, the dispersions are stable against sedimentation and further aggregation for a period of weeks at least. Atomic-force-microscopy studies on deposited films reveal that the bundle diameter distribution decreases dramatically as concentration is decreased. Detailed data analysis suggests the presence of an equilibrium bundle number density and that the dispersions self-arrange themselves to always remain close to the dilute/semi-dilute boundary. A population of individual nanotubes is always observed which increases with decreasing concentration until almost seventy percent of all dispersed objects are individual nanotubes at a concentration of 0.004 mg/ml in the NMP dispersions and for γ-Butyrolactone forty percent of all dispersed objects are individual nanotubes at a concentration of 6×10^{-4} mg/ml. The presence of individual nanotubes in NMP dispersion was confirmed by photoluminescence spectroscopy. Concentration dependence of the photoluminescence intensity confirms that the AFM measurements reflect the diameter distributions in-situ. In addition, Raman spectroscopy confirms the presence of large quantities of individual nanotubes in the deposited films.

Building on the experimental evidence garnered from studying the dispersive effects of NMP, we demonstrate *spontaneous* exfoliation of single-walled carbon nanotubes on dilution of nanotube dispersions in NMP. The components contributing to the thermodynamics of mixing of this system are presented. Due to their size and rigidity, dissolution cannot be driven by a large mixing entropy. Thus, their mixing enthalpy would have to be small or negative to result in a solution. Light-scattering measurements show the enthalpy of mixing to be approximately zero and hence the free-energy of mixing to be negative, confirming athermal solubility. STM measurements show that NMP is sequestered inside bundles even after drying. Annealing removes this NMP and yields pristine tubes, indicating that the large solvent-nanotube interfacial energy required for solubility is solely due to dispersion type interactions. Experiments, supported by a simple

model, show that successful solvents for nanotubes are those with surface tensions close to that of graphite – vital information for the implementation of debundled SWNTs in various applications.

The debundling by dilution seen in the two phase media above has been shown for dispersions of SWNTs in the surfactant sodium dodecylbenzene sulphonate (SDBS). The same sonication/dilution/mild-centrifugation approach results in a concentration dependent bundle diameter distribution which saturates at $D_{rms}{\sim}2nm$ for concentrations, $C_{NT}{<}0.05$ mg/mL. Significantly, this method does not require an ultracentrifugation processing step which results in more efficient use of the SWNTs used. The total bundle number density increases with concentration, saturating at ~6 bundles per $\mu m3$ for $C_{NT}{>}0.05$ mg/mL/. As the concentration is reduced the number fraction of individual nanotubes grows, approaching 50% at low concentration. In addition, partial concentrations of individual SWNTs approaching 0.01 mg/mL can be realised. These values are far superior to those for solvent dispersions due to repulsion stabilisation of the surfactant coated nanotubes.

To conclude, a robust, repeatable and relatively straightforward method for the exfoliation of SWNTs in simple two phase media has been reported. Associated with this, clear guidelines have been outlined for choosing appropriate solvents for such exfoliation. This has resulted in a massive increase in the number of known 'good solvents' for debundling SWNTs. The debundling by dilution central to this work has been applied to a surfactant based dispersion for comparative reasons, but also outlining a much more straightforward method of producing dispersions rich in individual SWNTs.

Acknowledgements

What can you learn in four years? In that time I have come to realise that a scientist is only as good as the team he works with. A written thesis is but a drop in the sea of knowledge on which one sails whilst in college. To that end, clichéd and all as it sounds I could not have done it without the support of others, but more than that I ask the question what point is there in doing it without others to share the journey with you.

To begin I wish to thank the newly appointed Professor Johnny Coleman for his consistent, vigilant and enthusiastic supervision. Questions were answered, answers were questioned. Special thanks to Valeria for her tireless efforts to help me with many aspects of the slog that is experimental work! To Prof Werner Blau, I express my gratitude for support and giving me an opportunity to work in a dynamic and indeed unique group. To the school of Physics and the many members of staff I have dealt with both as a under- and post-graduate, I would like to thank you for all your support. The technical and administrative group are the oil that keeps the engine running: thanks to John K, safety Joe, Jemmer, Mick, Ken, Gillian, Rebecca, Úna, Pat and Gordon.

Intel have proved themselves truly interested in my project since I began working with them and this has not diminished as they continued to support me financially and otherwise through my studies. Thanks to my mentor Carlos Martinez for all his help. The work presented in this thesis could not have been produced without the assistance of our collaborators (as outlined in the appendix): my thanks to you all.

How should I thank my colleagues, many of whom are now my friends? I think anyone who has had a positive experience of our group will agree getting in their and getting involved has been the key. To the original crew (the Doolin crowd) that welcomed me to the fold; Adam, Andy, Anna, Chris K, Colin, David (francais), Denis, Eimhín, Emer, Fiona, Gordon, Grace, Helen, James, Keith, Kevin, Manuel, Margaret, Martin Cadek, Martin Djiango, Nacho, Patrick, Ramesh, Rebekah, Rob, Roberto, Ronan, Rory, Sandy, Sharon, Silvia, Sonia, Stephen (Slipper), Tadgh, Takeyuki, and Valeria. To the various 'newbees' that have arrived since; Chris, Darren, David (Richard), Denise, Donal, Eleni, Eva, Evelyn, Ian, Javier, Jun, Karen, Les, Marjo, Niall, Paula, Phil, Shweta, Sukanta, Trevor, Umar, Yenny, Zhenyu, and of course Aaron & Michele (honorary members). Special thanks to those of you that helped with correcting my thesis. We all comment on how the group has changed all the time, but I think the element of fun that attracted me to the group in the first place is still at the core of what we do – and we do it well! During my time as a postgraduate I had to pleasure of working with many undergraduates as summer

Table of Contents

CHAPTER 5: DEBUNDLING OF SINGLE-WALLED NANOTUBES BY DILUTION: OBSERVATION OF LARGE POPULATIONS OF INDIVIDUAL NANOTUBES IN AMIDE SOLVENT DISPERSIONS

CHAPTER 6: EXFOLIATION IN ECSTASY: LIQUID CRYSTAL FORMATION AND CHIRALITY DEPENDENT DEBUNDLING OBSERVED FOR SINGLE WALLED NANOTUBES DISPERSED IN THE LIQUID DRUG γ-BUTYROLACTONE

CHAPTER 7: LARGE POPULATIONS OF INDIVIDUAL SINGLE WALLED NANOTUBES IN SURFACTANT-BASED DISPERSIONS WITHOUT THE NEED FOR ULTRACENTRIFUGATION

CHAPTER 8: CONCLUSIONS   (140)

CHAPTER 9: APPENDIX

Chapter 1

Motivation and Thesis Outline

1.1 Motivation

Materials have always played an integral part in human history and have allowed us to repeatedly develop, innovate and evolve. Indeed, throughout our history the ages of man have been labelled by the primary material of the era: from stone, to metal, to the technological age we live in today. The materials that forge this change and shape tomorrow's world continue to present new and remarkable phenomena associated with them. One of the major areas of interest of late has been nanotechnology. Richard Feynman famously foretold in 1959 of the possibilities in nano-materials claiming 'There's plenty of room at the bottom' but he was only able to discuss what was possible in principle as he said 'we have not got round to it yet'[1]. The ability today to manipulate, process, and harness the properties of materials on this scale has recently seen the number of publications on nano-materials increase rapidly[2, 3].

One example of a material on this scale is the carbon nanotube: a one dimensional cylindrical macromolecule. Since their discovery[4, 5], they have attracted massive amounts of research funding[6] and scientific interest as their superlative properties[7] could see them play a pivotal role in the materials of tomorrow[3]. Applications ranging from a carbon nanotube space-elevator[8] to transparent conductive films[9] and much more have been heralded proving the worth of these materials but also highlighting the many issues that must be resolved before realising their full potential.

The single walled carbon nanotube (SWNT) is found to aggregate, forming rope like bundles that are held together by Van der Waals interactions between adjacent nanotubes[10]. When in these bundles the nanotubes lose their potential for many of their possible applications; problems such as inter tube slippage diminish the overall mechanical

properties of nanotubes; also the variety of electrical types of nanotubes present in the bundle blurs their electrical properties. Thus, one of the major obstacles to be addressed in this field is the debundling of single walled carbon nanotubes and that is the subject of this thesis.

1.2 Thesis Outline

Chapter 2 – Materials and Background will begin with a discussion on the element carbon. Specifically, I will focus on the allotrope of carbon that is of interest to us in this work: the carbon nanotube. An outline of the structure, properties, methods of preparation, applications and limitations of carbon nanotubes will be presented. This will be followed by a brief overview of the various dispersive techniques that result in the debundling of SWNTs.

Chapter 3 – Theory and Characterisation Methods will begin by outlining the thermodynamic criteria for a solution. These criteria will be relevant when considering the spontaneous exfoliation of SWNTs in chapter 5. A brief overview of the interaction of light with matter is presented with specific reference to the optical phenomena observed elsewhere for SWNTs. Many of these phenomena are observed by the various spectroscopic techniques employed in this work. The experimental set up for these techniques have been briefly described in this chapter. Finally, the operation and theoretical background of the atomic force microscopy are outlined emphasising the imaging of one dimensional objects, such as SWNTs.

Chapter 4 – Debundling of Single Walled Nanotubes by Dilution: Observation of Large Populations of Individual Nanotubes in Amide Solvent Dispersions. Large scale debundling of single-walled nanotubes has been demonstrated by dilution of nanotube dispersions in the solvent N-methyl-2-pyrrolidone (NMP). This chapter will present results clearly outlining the exfoliating effect of NMP on bundles of SWNTs. The dilution dependent debundling effect will be characterised and the factors that make NMP and other reported 'good solvents' a dispersant for SWNTs will be discussed.

Chapter 5 – Towards Solutions of Single Walled Carbon Nanotubes in Common Solvents. The aim of this chapter is to demonstrate spontaneous exfoliation of single-walled carbon nanotubes on dilution of nanotube dispersions in N-methyl-pyrrolidone (NMP). SWNTs are shown to be solubilised in NMP, i.e. the free-energy of mixing, ΔG_{Mix}, is negative.

Chapter 6 – Exfoliation in Ecstasy: Liquid Crystal Formation and Chirality Dependent Debundling Observed for Single Walled Nanotubes Dispersed in the Liquid Drug γ-Butyrolactone. This chapter will present results on the dispersion of SWNTs in γ-Butyrolactone. This liquid, sometimes referred to as "liquid ecstasy", is well known for its narcotic properties. At high concentrations the dispersions form an anisotropic, liquid crystalline phase which can be removed by mild centrifugation. At lower concentrations an isotropic phase is observed with a biphasic region at intermediate concentrations. The nature of these phases will be discussed in this chapter, outlining vital advantages and limitations for the implementation of SWNTs into composites.

Chapter 7 – Large Populations of Individual Single Walled Nanotubes in Surfactant-Based Dispersions without the need for Ultracentrifugation. This chapter will demonstrate stable dispersions of single walled carbon nanotubes that been produced using the surfactant sodium dodecylbenzene sulphonate (SDBS). Crucially, it will be shown that on dilution of these dispersions, the nanotubes exfoliate from bundles, resulting in a concentration dependent bundle diameter distribution. Thus, the requirement of the cumbersome ultracentrifuge procedure, used for other surfactant based dispersions, will be shown to be superfluous.

Chapter 8 – Conclusions. Here, a brief synopsis of the findings of this thesis will be presented. Some aspects of on-going and future work will be discussed also.

Chapter 9 – Appendix. A brief overview of colloidal dispersions is presented. Also, a list of the relevant publications is outlined.

1.3 References

1. Feynman, R. The Feynman Lectures on Physics (Pearson/Addison-Wesley, London).
2. Scientific-American. The Nanotech Revolution (The Rosen Publishing Company, New York, 2007).
3. Baughman, R. H., Zakhidov, A. A. & de Heer, W. A. Carbon nanotubes - the route toward applications. Science 297, 787-792 (2002).
4. Iijima, S. Helical Microtubules of Graphitic Carbon. Nature 354, 56-58 (1991).
5. Iijima, S. & Ichihashi, T. Single-Shell Carbon Nanotubes of 1-Nm Diameter. Nature 363, 603-605 (1993).
6. Correia, A., Perez, M., Saenz, J. J. & Serena, P. A. Nanotechnology applications: a driving force for R&D investment. Physica Status Solidi a-Applications and Materials Science 204, 1611-1622 (2007).
7. Dresselhaus, M. S. Carbon Nanotubes: Synthesis, Structure, Properties and Applications (Springer-Verlag, Berlin, 2001).

8.   Aravind, P. K. The physics of the space elevator. American Journal of Physics 75, 125-130 (2007).

9.   Wu, Z. et al. Transparent, Conductive Carbon Nanotube Films. Science 305, 1273-1276 (2004).

10.   Giordani, S. et al. Debundling of single-walled nanotubes by dilution: Observation of large populations of individual nanotubes in amide solvent dispersions. Journal of Physical Chemistry B 110, 15708-15718 (2006).

Chapter 2

Materials and Background

2.1 Materials

This chapter will discuss the element carbon – specifically its allotrope the carbon nanotube. The suite of properties associated with these nano materials is outlined, showing the advantages and drawbacks to using these materials in a host of possible applications. The second section of this chapter aims to provide a background to the various techniques that have been implemented recently for the dispersion of single walled carbon nanotubes. This should provide the reader with a general understanding to the alternative approaches for the dispersion of nanotubes and also elucidate where the motivation for many of the ideas incorporated this work originated.

2.1.1 Carbon

Carbon is truly a unique element: It occupies the favoured position of having exactly four valence electrons and hence requires four bonds to make a closed shell. Thus carbon has the capacity to share electrons with as many as four different atoms, including other carbon atoms. As a result, carbon has the ability to form a vast array of compounds[1], proving itself to be perhaps the most versatile element, being the single most important element responsible for the creation of life. Carbon's ability to bond with other carbon atoms, as well as the ability to form strong π-bonds, means that only carbon is stable as an extended covalently bonded elemental 2-D structure[2].

The electronic configuration of the carbon atom allows it to form a number of hybridized atomic orbitals. Carbon-carbon covalent bonds have directional properties. These two facts give carbon the ability form various molecular and crystalline structures[3].

The nature of the bonds between the carbon atoms underlies the varied chemical and physical properties of the carbon allotropes. Historically, two allotropes of solid carbon were known: diamond and graphite. Diamond, an electrical insulator, has a 3D lattice crystal structure where each carbon adopts an sp^3 hybridisation and is σ-bonded to four other carbon atoms in a tetrahedral conformation, as shown in figure 2.1(a). The strength of these covalent bonds results in diamond being the hardest known material to mankind[4].
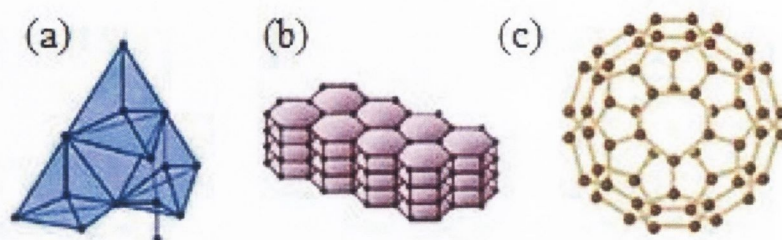
Figure 2.1

Three common allotropes of carbon[5] (a) Diamond where each carbon is sp^3 hybridised, (b) Graphite comprised of layers of sp^2 hybridised carbon, and (c) the Buckminster fullerene or C_{60}.

The lowest energy state of elemental carbon, at ambient pressure and temperature, is graphite. Graphite consists of individual graphene layers, in which each carbon is covalently bonded to three other carbons within a plane, forming an extended hexagonal structure, as shown in figure 2.1(b). A fourth orbital (π-orbital), from each carbon atom, lies perpendicular to the σ-bond plane, and it overlaps with its neighbours forming an extended sheet-like bonding state. Graphite is a conducting material. Normally, strong atomic potentials and covalent bonding imply the existence of a large band-gap. However, due to the hexagonal array of the sp^2-bonded carbon atoms and the resulting potential, the structure cannot distinguish between the π and $π^*$ states at the Fermi level. Thus, they remain equal in energy and the two bands formed, from the $2p_z$ orbitals, touch at the Fermi level[2]. A graphene sheet can therefore be described as a semi-metal.

In 1985 an experiment aimed at understanding the mechanisms by which long chained carbon molecules are formed in interstellar space and circumstellar shells, lead to the discovery of the third allotrope of carbon; the Buckminster fullerene[6]. This is comprised of sixty carbon atoms, each with sp^2 hybridisation, with hexagons and pentagons arranged to form the Buckyball shape – the structure of which is shown in figure 2.1(c). Their discovery lead to a new field of carbon chemistry that resulted in the

unearthing of the multi walled carbon nanotube (MWNT)[7] in 1991 by Iijima et al. A MWNT can be visualised as graphene layers rolled up to form concentric tubular structures, each capped at both ends with half a fullerene, as illustrated in figure 2.2(a). In 1993, Iijima and his team continued their groundbreaking work by imaging a single walled carbon nanotube (SWNT)[8]. This can be thought of as one graphene sheet rolled to form a tube, as shown in figure 2.2(b).
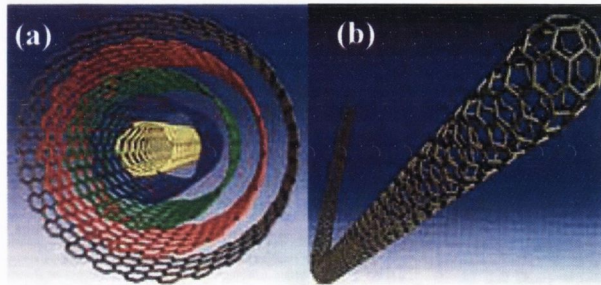
Figure 2.2[5]

(a) Cross-sectional pictorial representation of a multi-walled carbon nanotube. (b) Single-walled carbon nanotube.

Since their discovery carbon nanotubes have promised to play a leading role in the nanotechnology revolution. Their truly amazing properties have gripped the imagination of scientists from many diverse fields. This thesis begins by outlining the structure and properties associated with these unique macromolecules.

2.1.2 Structure of Single-Walled Carbon Nanotubes

A SWNT can be described as a graphene sheet rolled into a cylindrical shape. The structure is one dimensional with axial symmetry, and in general exhibiting a spiral conformation, called chirality[9]. Images of SWNTs show them to be one dimensional, with diameters of 0.7 – 10.0nm[8]. It should be noted that the fatter nanotubes are seen to collapse. They typically have aspect ratios of approximately 1000:1. A crucial point about the structure of a SWNT is the orientation of the six-membered carbon ring in the honeycomb lattice relative to the axis of the nanotube. Depending on how one imagines rolling a graphene sheet to construct a tube, as shown in figure 2.3, achiral and chiral SWNTs result.
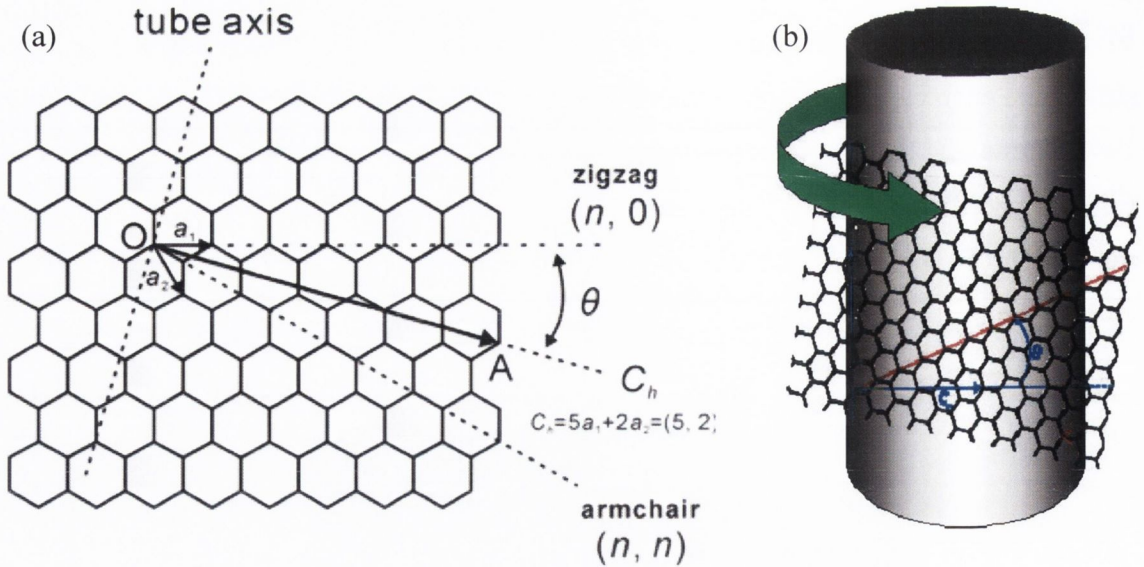
Figure 2.3[10]

(a) The unrolled honeycomb lattice of a SWNT. The chiral vector, C_h, is defined by $\overrightarrow{OA}$ and is expressed in terms of integers (n,m). θ is the chiral angle where $0°\leq\theta\leq30°$. The diagram shows the construction of a (5,2) SWNT. (b) Pictorial representation of the various ways a graphene sheet can be rolled to form a SWNT.

The structure of a SWNT can be classified according to a pair of (n,m) integers that define the rolling or chiral vector, C_h[11]. The chiral vector can be expressed in terms of the real space vectors $\mathbf{a_1}$ and $\mathbf{a_2}$ of the hexagonal lattice.

$$C_h = n\mathbf{a}_1 + m\mathbf{a}_2 \equiv (n,m) \tag{2.1}$$

SWNTs with the specifications (n,0) and (n,n) are achiral and are labelled as *zigzag* and *armchair* respectively. These correspond to a chiral angle, θ, (as illustrated in figure 2.3) value of 0° and 30° respectively. All other (n,m) chiral vectors, for $0° < \theta < 30°$, correspond to chiral SWNTs. The diameter of the SWNT, d, can be given by L/π, where L is the circumferential length of the SWNT.

$$d = L/\pi, \quad L = |C_h| = \sqrt{C_h.C_h} = a\sqrt{n^2 + m^2 + nm} \tag{2.2}$$

2.1.3 Electronic Properties of SWNTs

The simplest way to comprehend the electronic structure of a carbon nanotube is by considering its parent material graphite[12]. Bulk graphite has electronic σ bands that are responsible for the strong in-plane covalent bonds within the two-dimensional (2D)

8

graphene sheets, while the π bands are responsible for weak van der Waals interactions between such sheets in graphite. In contrast to the σ bands, the π bands are close to the Fermi level, so that electrons can be excited from the valence (π) to the conduction (π^*) band optically. Figure 2.4a shows the electronic dispersion for the π and π^* bands of 2D graphite (i.e. a graphene layer) in the first Brillouin zone, obtained with the tight binding (TB) method[9]. The optical transitions occur close to the edges of the hexagonal Brillouin zone, at the K points, where the valence and conduction bands touch each other.

When a sheet of a graphene is rolled up to form a carbon nanotube, the wave vectors along the circumferential direction become quantized due to periodic boundary conditions ($\mathbf{k}_x = jK_1$, where $K_1 = 2/d_t$, where d_t is the tube diameter, and j is an integer), while the wave vectors $\mathbf{k}_y$ along the tube axis direction and K_2 remain continuous ($\mathbf{k}_y = \alpha K_2$, α is real number, $|\alpha| < 1/2$). K_1 and K_2 are the basis vectors for the nanotube Brillouin zone. The resulting lines of allowed wave vectors in the carbon nanotube reciprocal space can be represented in the 2D graphene-sheet Brillouin zone by cutting lines of allowed wave vectors, as shown in figure 2.4a by solid lines with dots[13]. The electronic band structure of the nanotube can then be obtained, as shown in figure 2.4b, by superimposing the 1D cutting lines on the 2D electronic constant-energy surfaces. The SWNT electronic structures in figures 2.4a and 2.4b are given for a (4,2) SWNT, chosen here for illustrative purposes. The (4,2) designation represents the (n,m) indices used to define the nanotube structure: diameter d_t and chiral angle θ.
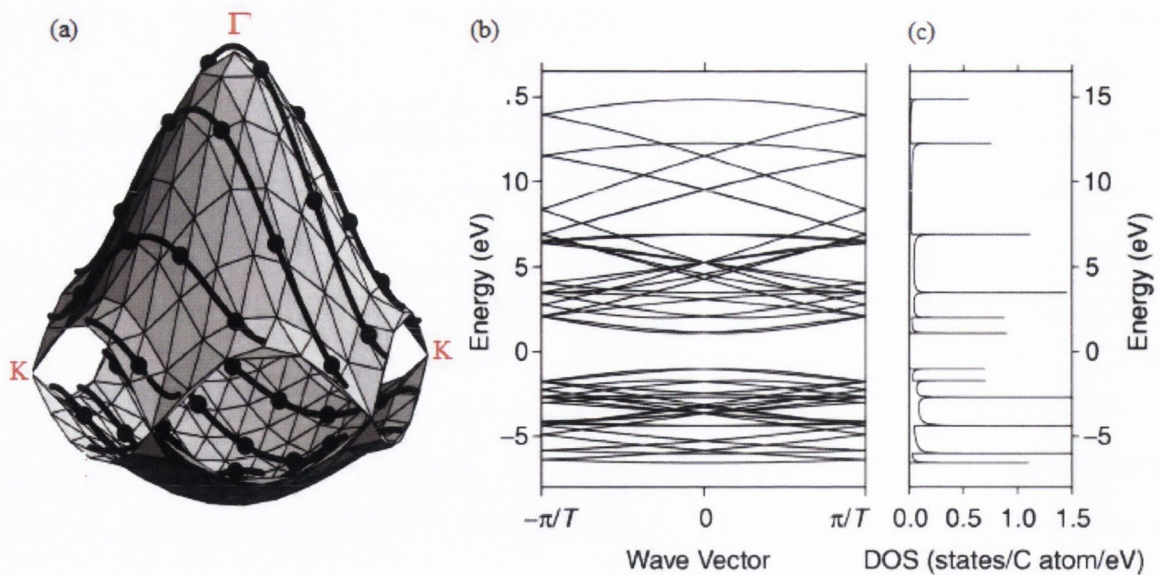
Figure 2.4

(a) The calculated constant-energy contours for the conduction and valence bands of a graphene layer in the first Brillouin zone using the π-band nearest-neighbour tight-binding model[9]. Solid curves with dots show the cutting lines for the (4,2) nanotube[13]. (b) Electronic energy band diagram for the (4,2) nanotube obtained by zone-folding from (a). T gives the length of the nanotube unit cell along the tube axis. (c) Density of electronic states for the band diagram shown in (b).

The 1D electronic band structure for the (4,2) SWNT can be further simplified by considering the electronic density of states (DOS), as shown in figure 2.4(c). The absorption and emission rates in SWNTs are related directly to the electronic states at the van Hove singularities. These singularities are a direct result of the 1D nature of SWNTs[11]. The distance between two cutting lines, as shown in figure 2.4(a), can be related to the SWNT diameter through $K_1 = 2/d_t$. It can be clearly seen that the direction of these cutting lines is dependent on the chiral angle, θ, or rolling direction. Thus for each (n,m) SWNT type the resulting electronic structure will be different. If the cutting lines pass through the K points, the SWNT will display metallic behaviour and in between these points of degeneracy, the SWNTs will have band-gaps of varying proportions. To recap, all armchair, (n,n), nanotubes display metallic behaviour. For zigzag (n,0) SWNTs, when n is a multiple of 3, they are metallic. In the case of chiral SWNTs, the tube will be metallic if the cutting lines, as shown in figure 4.4(a), pass through a K point. Thus, SWNTs where n-m = (multiple of 3), the SWNTs are metallic, whereas the SWNTs are semiconducting for

other chiralities[14]. This diversity of structure hints at the unlocked potential that SWNTs have to offer the electrical world but also, at the difficulties in realising this potential.

2.1.4 Physical Properties of SWNTs

SWNT production yields a mixture of semiconducting and metallic tubes. The conduction mechanism for metallic SWNTs is similar to that of graphite[15] – based on delocalised π-bonds. Ballistic conduction (i.e. no scattering) through individual SWNTs has been reported[16, 17] allowing them to carry large currents with effectively no heating. Phonons also propagate easily through carbon nanotubes, with thermal conductivities of 1750-5800 W/m-K reported[18] greater than that of either diamond or basal plane graphite (2000 W/m-K[19]).

SWNTs are quite stiff and exceptionally strong, meaning they have a high Young's modulus and a high tensile strength[20]. Salvetat et al.[21] observed a Young's modulus of ~1TPa. Yu et al. investigated nanotube bundles and reported tensile strengths between 10 and 50GPa. Failure was seen to occur at 5.3% elongation yielding a toughness of 770 J/g. Impressively, the density normalised modulus and strength of a typical SWNT is reported as being ~19 and ~56 times that of steel wire[22]. These numbers will only be realised on an application platform when the properties of individual SWNTs can be transferred to the macro scale by incorporation into fibres and sheets – as bundling related issues, such as inter-tube slippage, acts as the major limiting factor for harnessing the full mechanical capabilities of SWNTs[20].

2.1.5 Production of SWNTs

SWNTs can by produced by carbon-arc discharge, laser ablation of carbon, or chemical vapour deposition (CVD) (onto catalytic particles)[23]. The SWNTs used in this work were made using the 'High-Pressure Carbon Monoxide', or HiPCo[24], method – a CVD method. Synthesis methods for SWNTs typically result in significant concentrations of impurities. Carbon-coated metal catalyst particles contaminate the nanotubes produced via all routes (including the HiPCO route). All production methods result in a mix of SWNT types. However, no route to substantial quantities of SWNTS, of any one type, has been reported yet.

2.1.6 Applications and Limitations of SWNTs

Since their discovery, many possible applications[22] have been imagined for nanotubes, each built on their wealth of unique properties: conductive and high strength composites[25]; energy storage and energy conversion devices[26-28]; field emission displays[29, 30]; nanometre semiconducting devices[31, 32]; probes and interconnects[33, 34].

However, the full potential of SWNTs is still to be unlocked as there remain a number of significant barriers for the field to overcome. Impurities as a result of the production process, scaling up the production methods, cost of production and lack of chirality control include some of the major obstacles to using SWNTs in applications[22, 35]. Furthermore, SWNTs bundle together via Van der Waals forces[36]. This causes slipping between adjacent nanotubes diminishing their mechanical properties and also results in a 'blurred' electronic structure. The mechanical, thermal, and electronic properties unique to SWNTs can only be fully harnessed when they are isolated from one another. As discussed, SWNTs aggregate into bundles or ropes, by van der Waals interactions, due to their relatively high surface energy[37]. These bundles can be tens of nanometers in diameter and many micrometers long and contain huge numbers of both metallic and semiconducting SWNT tubes. As a consequence, dispersed, isolated SWNTs are rarely available to scientists at realistic concentrations for applications. In the following paragraphs, I will outline the various techniques reported in the literature for attaining debundled, dispersed SWNTs. Short reviews, relevant to the work presented in this thesis, will also be presented at the beginning of each results chapter.

2.2 Background - Dispersion of SWNTs

2.2.1 Acid Based Dispersions

SWNTs have been dispersed in superacids by direct protonation[38-40]. Optically homogeneous mixtures with concentrations as high as 80mg/mL have been observed. The dispersed nanotubes were seen to exist in solution as individual polycarbocations in an isotropic phase at very low concentrations and were seen to transform to a nematic mesophase at high concentrations. The intrinsic alignment of SWNTs in the liquid crystalline mesophase was seen to be preserved in the solid SWNT aggregates upon precipitation followed by the removal of the acid. It is felt that such a phase holds great potential in applications such as fibres and films but questions have to be asked about the

integrity of the SWNTs structure, and hence its properties, following the reaction which such strong acids.

2.2.2 Noncovalent Attachment – Polymer Wrapping

In 2001, Smalley et al.[41] reported SWNTs had been reversibly dispersed, in the mg/mL SWNT concentration range, by noncovalently associating them with a variety of linear polymers such as polyvinyl pyrrolidone (PVP) and polystyrene sulphonate. They demonstrated that the association between the polymer and the SWNT is robust, not dependent on the presence of excess polymer in solution, and is uniform along the sides of the tubes.

Extensive work from the School of Physics, here at Trinity College Dublin, was carried out on SWNT-polymer composites, specifically a derivative of PVP - poly(m-phenylenevinylene-co-2,5-dioctoxy-p-phenylenevinylene)(PmPV)[42]. This work concentrated primarily on the incorporation of polymer into SWNT composites leading to a dramatic enhancement of the composites properties. It was also shown that PmPV acted as a filter when incorporated with nanotubes and that the luminescent properties of PmPV were enhanced by their inclusion in the composite[43]. Microscopical analysis showed the polymer to wrap itself around the nanotube lattice[44, 45]. Building on this work PmPV was successfully used to wrap around SWNTs on account of stabilising noncovalent bonding interactions between the polymer and nanotubes[46]. This work showed that it is possible to noncovalently functionalise SWNTs without destroying the electronic character of the SWNTs themselves. More recently, work by Coleman et al.[47] developed a method for the controlled debundling of SWNTs based on their interaction with poly[m-phenylenevinylene-co-(1,5-dioctyloxy-2,6-naphthylene vinylene)] (mpNV), as well as an indirect method for measuring the polymer-nanotube binding energy. This method relies on the luminescence of the polymer being quenched whilst associated with a SWNT. The polymer-SWNT mixture was diluted and sonicated, allowing the nanotubes to be wrapped and prevent re-bundling. As the concentration lowered, the total surface area of the SWNTs increased due to them debundling allowing more polymer to bind to the SWNTs. Thus the level of polymer quenching was used as a measure of the debundling. Dispersions containing stable individual SWNTs, confirmed with atomic force microscopy (AFM), were seen for SWNT concentrations of $\approx 1 \times 10^{-4}$ mg/mL.

2.2.3 Noncovalent Attachment – Biomolecules

The novel properties of SWNTs have potential biological applications ranging from sensors to tissue supports to artificial muscles[48, 49]. As with other potential applications the bundling of SWNTs acts as a limiting factor. Much work has been carried out with respect to dispersing SWNTs in a biologically friendly environment: this has yielded important information on the dispersibility of SWNTs.

DNA is a naturally occurring polymer that plays a pivotal role in biology. Nakashima[50] and Zheng[51] have shown that the inorganic substrate-binding properties of DNA can be harnessed by reporting DNA-assisted dispersion and separation of SWNTs. Bundled SWNTs were effectively dispersed in water by their sonication in the presence of single-stranded DNA. Later work showed the dispersion to be dependent on the specific DNA sequence forming a basis for SWNT diameter and type separation[52]. Work at this laboratory recently reported the spontaneous debundling of SWNTs in DNA based dispersions[53]. Similar to results shown in this thesis, the mean bundle diameter was shown to be concentration dependent. Partial concentrations of individual SWNTs of 6.2% were measured showing this debundling technique to be very promising for the implementation of SWNTs in biological applications.

Dieckmann and co workers have investigated the interaction of SWNTs with amphiphilic peptide helices[54, 55]. The peptide in question folds into an amphiphilic α-helix, in which apolar residues from the other face facilitate the dispersion of SWNTs. They also demonstrate, with AFM, isolated individual peptide wrapped SWNTs that are connected end to end into long fibrillar structures. More recent work has shown that by controlling the length of reversible cyclic peptides, diameter-selective dispersion of SWNTs has been achieved (spectroscopically and microscopically)[56]. They describe a class of peptides that covalently close around the circumference of the nanotube. Once the peptides encircle the SWNTs, they do not dissociate from them leading to very stable dispersions. By tailoring the length of the peptide in question nanotubes of specific diameter can be dispersed. This is quite significant but the use of high speed centrifugation results in a low yield of mono-dispersed SWNTs. In a similar approach to the debundling of SWNTs by dilution, described above for DNA based systems, work in this group at the moment is investigating debundling by dilution for peptide based systems[57]. This method would negate the use of the ultra centrifugation step that severely limits the final yield.

2.2.4 Noncovalent Attachment - Surfactants

Perhaps the most successful dispersion technique to date, in terms of harnessing the full potential from debundled SWNTs has been through the noncovalent attachment of surfactants[58]. Surfactants have been found to form micelles around SWNTs, following a high power sonication step, forming a protective sheath around the SWNTs that shields them from the solvent and thus prevents rebundling of the SWNTs that normally occurs due to the large surface energy difference between surface and solvent[59]. Bundles surrounded by micelles of surfactant are removed by ultra centrifugation due to their higher specific gravity. These dispersions, rich in individual SWNTs, lead to the observation of fluorescence from semiconducting individual SWNTs by Weisman et al.[59]. The same group went on to observe distinct electronic absorption and emission transitions for more than 30 semiconducting nanotube species. By combining the fluorescence results with resonance Raman spectra, each optical transition was mapped to a specific (n,m) nanotube structure[60]. The strength of this technique is twofold; firstly, as the E_{11} and E_{22} energy gaps for a semiconducting SWNT are dependent on its diameter and chiral angle, the excitation and emission wavelength peaks seen in this experiment can be directly linked to the (n,m) chirality of the corresponding nanotubes; secondly, as approximately one in three nanotubes is metallic, bundles of three or more SWNTs will contain, on average, a metallic nanotube that will quench any fluorescence – thus making this technique an excellent measure of SWNT dispersion.

Employing the dispersion technique outlined by Weisman above, the dispersive effects of various anionic, cationic, and non-ionic surfactants on SWNTs were investigated[61]. The various dispersions were characterised spectroscopically and then compared. Sodium dodecylbenzene sulphonate (SDBS) was found to give the most resolved spectral features for ionic surfactants. In the case of the non-ionic systems, surfactants with higher molecular weights were found to suspend more SWNTs and to display more profound spectral features. The nature of the interaction between surfactant and nanotube has been examined by Resasco and co workers[62]. Their analysis of adsorption isotherms of the anionic surfactant SDBS on SWNTs indicates that the interactions between the surfactant molecules and the nanotube walls are mostly hydrophobic in nature and that only at pH values far from the point of zero charge do Coulombic forces come into play. Their adsorption study also showed that at saturation, each nanotube is covered by a monolayer of surfactant, in which the molecules rest with tails orientated vertically on the surface. Thus the SWNTs are thought to be *suspended* by the surfactant monolayer and are not thought to be solubilised in the interior of the micelle.

2.2.5 Mono – Dispersion of SWNTs

One of the major road blocks to the implementation of SWNTs in electrical devices is the inability to separate nanotubes by type, or metallicity to any significant degree. A number of reports have been published of late evidencing various methods that are giving limited but promising results. The organisation of surfactant amines and single stranded DNA onto SWNTs have provided among the highest metal from semiconducting separation (as high as 92%) along with the ability to enrich according to diameter[52, 63, 64]. Papadimitrakopoulos et al. have carried out considerable work in this field. In 2003, they reported the first methodology for the bulk enrichment of acid – functionalised SWNTs. Semiconducting SWNTs were retained in the supernatant as a result of stronger octadecylamine adsorption on their sidewalls[65]. A further report outlined an argument linking the redox characteristics of SWNTs to their diameter and metallicity enrichment[66]. Combining this technique with SWNT samples of narrow diameter distribution[67], the authors believe this to be a reliable method to fractionate nanotube types.

2.2.6 Conclusions

As it stands, the research to date on the exfoliation of nanotubes is quite broad in its approach. As the primary goal of this research is to yield stable debundled SWNTs at high concentrations, with a view to implementing them into countless possible applications, we must consider the requirements of such applications. The most obvious factor when considering the implantation of SWNTs into any composite is processibilty. With that in mind, a simple two-phase approach to the dispersion of SWNTs would be most favourable – i.e. SWNTs dispersed in a simple solvent. Furthermore, a solid understanding of the factors controlling the exfoliation of SWNTs in any such solvent would be crucial to maximising any dispersive effect as well as acting as a guide for other possible dispersant solvents. Another processing factor that must be considered is the interaction of the SWNTs with other materials in possible composites. Different composites will require the interaction of the debundled SWNTs with various materials and the different dispersion techniques described above will allow some flexibility with this. Thus, for example, SWNTs debundled by their interaction with DNA could allow SWNTs to be inserted into biological environments. Similarly, good stress transfer between a polymer-filler and SWNTs in a mechanically strong composite would dictate the dispersant used. An excellent dispersant could shield the debundled nanotubes from tertiary interactions diminishing the properties of any related composite. Thus, it is felt that this field should be

striving towards controlled dispersions of SWNTs consisting of high concentrations of individual, defect free, nanotubes. These dispersions should be simply made, stable, repeatable, and have the end user in mind.

2.3 References:

1. Mannion, A. M. Carbon and Its Domestication (Springer).
2. Ventra, M. D. Introduction to Nanoscience and Technology (Academic Publishers, 2004).
3. Jones, L. & Atkins, P. Chemistry; Molecules, Matter, and Change (W.H. Freeman and Company, New York, 2000).
4. Pierson, H. O. Handbook of Carbon, Graphite, Diamond and Fullerenes; Properties, Processing and Applications (Noyes Publications).
5. http://www.azonano.com/work/LRvdj693G7BEO7Uz47XE_files/image003.jpg.
6. M.S.Dresselhaus, Dresselhaus, G. & Eklund, P. Science of Fullerenes and Carbon Nanotubes (Academic Press).
7. Iijima, S. Helical Microtubules of Graphitic Carbon. Nature 354, 56-58 (1991).
8. Iijima, S. & Ichihashi, T. Single-Shell Carbon Nanotubes of 1-Nm Diameter. Nature 363, 603-605 (1993).
9. Saito, R. D., M.S. Physical Properties of Carbon Nanotubes (Imperial College Press, London, 2001).
10. http://cobweb.ecn.purdue.edu/~agoyal/nano/chiral1.jpg.
11. Loiseau, A., Launois, P., Petit, P., Roche, S. & Salvetat, J. Understanding Carbon Nanotubes; From Basics to Applications (Springer, New York, 2006).
12. Charlier, J. C., Gonze, X. & Michenaud, J. P. First-principles study of the electronic properties of graphite. Physical Review B 43, 4579 (1991).
13. Samsonidze, G. G. et al. The concept of cutting lines in carbon nanotube science. Journal of Nanoscience and Nanotechnology 3, 431-458 (2003).
14. Wildoer, J. W. G., Venema, L. C., Rinzler, A. G., Smalley, R. E. & Dekker, C. Electronic structure of atomically resolved carbon nanotubes. Nature 391, 59-62 (1998).
15. Wallace, P. R. The Band Theory of Graphite. Physical Review 71, 622 (1947).
16. Bachtold, A. et al. Scanned Probe Microscopy of Electronic Transport in Carbon Nanotubes. Physical Review Letters 84, 6082 (2000).
17. Liang, W. et al. Fabry - Perot interference in a nanotube electron waveguide. Nature 411, 665-669 (2001).
18. Hone, J., Whitney, M., Piskoti, C. & Zettl, A. Thermal conductivity of single-walled carbon nanotubes. Physical Review B 59, R2514 (1999).
19. Kim, P., Shi, L., Majumdar, A. & McEuen, P. L. Thermal Transport Measurements of Individual Multiwalled Nanotubes. Physical Review Letters 87, 215502 (2001).
20. Coleman, J. N., Khan, U. & Gun'ko, Y. K. Mechanical Reinforcement of Polymers Using Carbon Nanotubes. Advanced Materials 18, 689-706 (2006).
21. Salvetat, J.-P. et al. Elastic and Shear Moduli of Single-Walled Carbon Nanotube Ropes. Physical Review Letters 82, 944 (1999).
22. Baughman, R. H., Zakhidov, A. A. & de Heer, W. A. Carbon nanotubes - the route toward applications. Science 297, 787-792 (2002).
23. Baddour, C. & Briens, C. Carbon nanotube synthesis: A review. International Journal of Chemical Reactor Engineering 3 (2005).
24. Nikolaev, P. et al. Gas-phase catalytic growth of single-walled carbon nanotubes from carbon monoxide. Chemical Physics Letters 313, 91-97 (1999).

25.   Coleman, J. N., Khan, U., Blau, W. J. & Gun'ko, Y. K. Small but strong: A review of the mechanical properties of carbon nanotube-polymer composites. Carbon 44, 1624-1652 (2006).

26.   An, K. H. et al. Electrochemical Properties of High-Power Supercapacitors Using Single-Walled Carbon Nanotube Electrodes. Advanced Functional Materials 11, 387-392 (2001).

27.   Chunming, N., Enid, K. S., Robert, H., David, M. & Howard, T. High power electrochemical capacitors based on carbon nanotube electrodes. Applied Physics Letters 70, 1480-1482 (1997).

28.   Baughman, R. H. et al. Carbon Nanotube Actuators. Science 284, 1340-1344 (1999).

29.   de Heer, W. A., Châtelain, A. & Ugarte, D. A Carbon Nanotube Field-Emission Electron Source. Science 270, 1179-1180 (1995).

30.   Lee, N. S. et al. Application of carbon nanotubes to field emission displays. Diamond and Related Materials 10, 265-270 (2001).

31.   Yao, Z., Postma, H. W. C., Balents, L. & Dekker, C. Carbon nanotube intramolecular junctions. Nature 402, 273-276 (1999).

32.   Tans, S. J., Verschueren, A. R. M. & Dekker, C. Room-temperature transistor based on a single carbon nanotube. Nature 393, 49-52 (1998).

33.   Wong, S. S., Joselevich, E., Woolley, A. T., Cheung, C. L. & Lieber, C. M. Covalently functionalized nanotubes as nanometre- sized probes in chemistry and biology. Nature 394, 52-55 (1998).

34.   Kim, P. & Lieber, C. M. Nanotube Nanotweezers. Science 286, 2148-2150 (1999).

35.   Smalley, R. E. et al. Single Wall Carbon Nanotube Amplification: En Route to a Type-Specific Growth Mechanism. J. Am. Chem. Soc. 128, 15824-15829 (2006).

36.   Thess, A. et al. Crystalline Ropes of Metallic Carbon Nanotubes. Science 273, 483-487 (1996).

37.   Nuriel, S., Liu, L., Barber, A. H. & Wagner, H. D. Direct measurement of multiwall nanotube surface tension. Chemical Physics Letters 404, 263-266 (2005).

38.   Ramesh, S. et al. Dissolution of pristine single walled carbon nanotubes in superacids by direct protonation. Journal of Physical Chemistry B 108, 8794-8798 (2004).

39.   Rai, P. K. et al. Isotropic-nematic phase transition of single-walled carbon nanotubes in strong acids. Journal of the American Chemical Society 128, 591-595 (2006).

40.   Davis, V. A. et al. Phase Behavior and rheology of SWNTs in superacids. Macromolecules 37, 154-160 (2004).

41.   O'Connell, M. J. et al. Reversible water-solubilization of single-walled carbon nanotubes by polymer wrapping. Chemical Physics Letters 342, 265-271 (2001).

42.   Curran, S. A. et al. A composite from poly(m-phenylenevinylene-co-2,5-dioctoxy-p-phenylenevinylene) and carbon nanotubes: A novel material for molecular optoelectronics. Advanced Materials 10, 1091-+ (1998).

43.   Curran, S. et al. Evolution and evaluation of the polymer/nanotube composite. Synthetic Metals 103, 2559-2562 (1999).

44.   McCarthy, B. et al. Observation of site selective binding in a polymer nanotube composite. Journal of Materials Science Letters 19, 2239-2241 (2000).

45.   Mc Carthy, B. et al. Spectroscopic investigation of conjugated polymer/single-walled carbon nanotube interactions. Chemical Physics Letters 350, 27-32 (2001).

46.   Alexander Star et al. Preparation and Properties of Polymer-Wrapped Single-Walled Carbon Nanotubes. Angewandte Chemie International Edition 40, 1721-1725 (2001).

47. Coleman, J. N. et al. Binding kinetics and SWNT bundle dissociation in low concentration polymer-nanotube dispersions. Journal of Physical Chemistry B 108, 3446-3450 (2004).

48. A. Bianco, M. P. Can Carbon Nanotubes be Considered Useful Tools for Biological Applications? Advanced Materials 15, 1765-1768 (2003).

49. Baughman, R. H. Materials Science: Playing Nature's Game with Artificial Muscles. Science 308, 63-65 (2005).

50. Nakashima, N. & Okuzono, S. DNA Dissolves Single-Walled Carbon Nanotubes in Water. Chemistry Letters 32, 456 (2003).

51. Zheng, M. et al. DNA-assisted dispersion and separation of carbon nanotubes. Nature Materials 2, 338-342 (2003).

52. Zheng, M. et al. Structure-Based Carbon Nanotube Sorting by Sequence-Dependent DNA Assembly. Science 302, 1545-1548 (2003).

53. Cathcart, H. et al. Spontaneous Debundling of Single-Walled Carbon Nanotubes in DNA-Based Dispersions. J. Phys. Chem. C 111, 66-74 (2007).

54. Dieckmann, G. R. et al. Controlled Assembly of Carbon Nanotubes by Designed Amphiphilic Peptide Helices. J. Am. Chem. Soc. 125, 1770-1777 (2003).

55. Zorbas, V. et al. Preparation and Characterization of Individual Peptide-Wrapped Single-Walled Carbon Nanotubes. J. Am. Chem. Soc. 126, 7222-7227 (2004).

56. Ortiz-Acevedo, A. et al. Diameter-Selective Solubilization of Single-Walled Carbon Nanotubes by Reversible Cyclic Peptides. J. Am. Chem. Soc. 127, 9512-9517 (2005).

57. Nicolosi, V., Cathcart, H., Dalton, A. B., Dieckmann, G. R. & Coleman, J. N. Spontaneous Exfoliation of Single Walled Carbon Nanotubes Dispersed Using Synthetic Peptides. In Preparation (In Prep).

58. Liu, J. et al. Fullerene Pipes. Science 280, 1253-1256 (1998).

59. O'Connell, M. J. et al. Band gap fluorescence from individual single-walled carbon nanotubes. Science 297, 593-596 (2002).

60. Bachilo, S. M. et al. Structure-assigned optical spectra of single-walled carbon nanotubes. Science 298, 2361-2366 (2002).

61. Moore, V. C. et al. Individually suspended single-walled carbon nanotubes in various surfactants. Nano Letters 3, 1379-1382 (2003).

62. Matarredona, O. et al. Dispersion of single-walled carbon nanotubes in aqueous solutions of the anionic surfactant NaDDBS. Journal of Physical Chemistry B 107, 13357-13367 (2003).

63. Maeda, Y. et al. Large-Scale Separation of Metallic and Semiconducting Single-Walled Carbon Nanotubes. J. Am. Chem. Soc. 127, 10287-10290 (2005).

64. Ge, G. S. et al. Quantitative evaluation of the octadecylamine-assisted bulk separation of semiconducting and metallic single-wall carbon nanotubes by resonance Raman spectroscopy. Applied Physics Letters 85, 1006-1008 (2004).

65. Chattopadhyay, D., Galeska, I. & Papadimitrakopoulos, F. A Route for Bulk Separation of Semiconducting from Metallic Single-Wall Carbon Nanotubes. J. Am. Chem. Soc. 125, 3370-3375 (2003).

66. Kim, S. N., Luo, Z. T. & Papadimitrakopoulos, F. Diameter and metallicity dependent redox influences on the separation of single-wall carbon nanotubes. Nano Letters 5, 2500-2504 (2005).

67. Bachilo, S. M. et al. Narrow (n,m)-Distribution of Single-Walled Carbon Nanotubes Grown Using a Solid Supported Catalyst. J. Am. Chem. Soc. 125, 11186-11187 (2003).

Chapter 3

Theory and Characterisation Methods

In this chapter I will briefly overview some of the theory pertinent to my thesis and profile the experimental techniques used. The primary aim of this work has been to observe and characterise the exfoliation of SWNTs in various media. Therefore, I begin this chapter by outlining the thermodynamic criteria for a 'solution'. A gamut of various spectroscopies was employed in my work to probe various aspects of SWNTs in various media. Thus, I present a short review on the interaction of light with matter. Finally I outline the experimental techniques used in this thesis. The various components of each instrument are presented along with some relevant theory.

3.1 Thermodynamic Theory[1]

"Thermodynamics has something to say about everything but does not tell us everything about anything."

Martin Goldstein and Inge F. Goldstein, "The Refrigerator and the Universe"

"In this house, we obey the laws of thermodynamics!"

Homer J. Simpson

Thermodynamics is mainly concerned with transformations of heat into work and the opposite transformations of work into heat. Modern science has shown us that heat is a form of energy and can be changed into other forms of energy. Before this, scientists believed that heat was some sort of fluid whose total amount was invariable. The heating of a body and analogous processes was interpreted as the transfer of this fluid. On the basis of this heat-fluid model Carnot showed the limitations involved in the transformation of

20

the heat into work – essentially the second law of thermodynamics. A short time later Mayer discovered the equivalence of heat and mechanical work, and announced the principle of the conservation of energy; i.e. the first law of thermodynamics.

We know today that the equivalence of heat and dynamical energy is based on a kinetic interpretation that reduces all thermal phenomena to the disordered motions of atoms and molecules. The mechanics of such a large set of particles would be superfluous and as such only average values are considered. This is known as *statistical thermodynamics*, which has been developed principally through the work of Maxwell, Boltzmann, Gibbs and others. Coupling this with pure thermodynamics we are armed with empirically based postulates where conclusions are drawn from them without involving the kinetic mechanism of the phenomena, but a kinetic interpretation can be applied.

3.1.1 First Law of Thermodynamics[1, 2]

The first law of thermodynamics deals with the conservation of energy. It has been shown experimentally that the internal energy of a system can be changed by either doing work on the system or heating it. Furthermore, heat and work are equivalent ways of changing a system's internal energy – we may know how the energy transfer has occurred but the system is blind to the mode employed. Experimentally, it has also been shown that if a system is isolated from its surroundings, then no change in internal energy takes place. These observations can be summarized as follows, for a closed system;

$$\Delta U = q + w \tag{3.1}$$

Where ΔU is the change in the systems internal energy, q is the energy transferred to the system as heat, and w is the work done on the system. It should be noted that the change in internal energy is not equal to the heat supplied when the system is free to change its volume. In this case, some of the energy supplied as heat to the system is returned to the surroundings as expansion work. In this circumstance the heat supplied to the system at constant pressure is equal to the enthalpy, H;

$$H = U + pV \tag{3.2}$$

where p and V are the pressure and volume of the system respectively. As U, p, and V are all state functions, the enthalpy is a state function and thus the change in enthalpy, ΔH, between any two states is independent of the path between them. It is shown that when a system is subjected to a constant pressure and only expansion work can occur, the change in enthalpy is equal to the energy supplied as heat. i.e:

$$dH = dq \tag{3.3}$$

3.1.2 Second Law of Thermodynamics[1, 2]

The natural tendency of systems to proceed toward a state of equilibrium is exhibited in many familiar forms. A hot object placed near a colder one will reach a common temperature. Common sense tells us that we never see two bodies in contact, which have the same temperature, spontaneously attain a state in which one has a high temperature and the other a lower temperature. Thus it is desirable to have some measure of the tendency to change and of the direction in which the change can occur. This leads us to the second law of thermodynamics which is used to identify the signpost of spontaneous change. The second law can be expressed in terms of another state function, the entropy, S. Entropy allows to asses whether one state is accessible from another by spontaneous change. So to clarify, the first law uses the internal energy to identify permissible changes and the second law uses entropy to identify the spontaneous changes among those permissible changes. Entropy is a measure of the disorder of a system. The second law of thermodynamics may be defined in terms of entropy as 'the entropy of an isolated system increases in the course of a spontaneous change':

$$\Delta S_{Tot} > 0 \tag{3.4}$$

Heat stimulates disorderly motion in the surroundings. Work, which stimulates uniform motion of atoms in the surroundings, does not change the degree of disorder, and thus does not change the entropy. Thus, the thermodynamic definition of entropy is based on the expression

$$dS = \frac{dq_{rev}}{T} \tag{3.5}$$

If we consider a nonreversible system, any change of state is accompanied by a change in entropy of the system, dS, and the entropy of the surroundings, dS_{Surr}, such that a the total change in entropy will follow

$$dS + dS_{Surr} \geq 0 \tag{3.6}$$

Taking equation (3.5) where the heat is supplied to the system (i.e. $dq_{Surr} = -dq$) from the surroundings, it follows that

$$dS \geq \frac{dq}{T} \tag{3.7}$$

This is known as the Clausius inequality.

3.1.3 Helmholtz and Gibbs Free Energies[2]

Entropy acts as the most basic concept for considering the direction of natural change, but in order to use it one would have to analyse changes in both the system and its surroundings. There also exists a simple method for automatically taking into account the entropy of the surroundings, which focuses attention on the system and is the foundation of many applications of chemical thermodynamics; the Gibbs and Helmholtz free energies. We are able to develop the Clausis inequality in two ways: constant volume or constant pressure. If we consider the constant volume case, we can say, in the absence of non-expansion work, that $dq_V=dU$. Thus,

$$dS - \frac{dU}{T} \geq 0 \qquad (3.8)$$

which can be rearranged to

$$TdS \geq dU \qquad (3.9)$$

At either constant internal energy ($dU=0$) or constant entropy ($dS=0$), this expression becomes

$$dS_{U,V} \geq 0 \quad \text{or} \quad dU_{S,V} \leq 0 \qquad (3.10)$$

i.e. in a system at constant volume and constant internal energy, the entropy increases in a spontaneous change. In a similar system at constant volume and constant entropy, the internal energy of a system decreases in a spontaneous change.

If we now consider the case where heat is transferred at constant pressure, and there is no work done other than expansion work, we can write $dq_P=dH$ and obtain

$$TdS \geq dH \qquad (3.11)$$

which at either constant enthalpy or constant entropy becomes

$$dS_{H,p} \geq 0 \quad \text{or} \quad dH_{S,p} \leq 0 \qquad (3.12)$$

which can be interpreted in a similar manner to equation (3.10). Equations (3.9) and (3.11) can be further simplified by introducing two new thermodynamic quantities. We define the Helmholtz energy, F, as

$$F = U - TS \qquad (3.13)$$

which for a changing system at constant temperature becomes:

$$dF = dU - TdS \qquad (3.14)$$

And the Gibbs energy, G, as

$$G = H - TS \qquad (3.15)$$

which for a changing system, at constant temperature, becomes:

$$dG = dH - TdS \qquad (3.16)$$

Incorporating the criteria for spontaneity (as given by equations (3.10) and (3.12)) we arrive at:

$$dF_{T,V} \leq 0 \quad \& \quad dG_{T,p} \leq 0 \tag{3.17}$$

As most chemical reactions occur at constant pressure where the volume is free to change, the Gibbs energy, or Gibbs free energy, is the most commonly known of these thermodynamic terms. Thus, the spontaneity of any reaction of interest (where pressure and temperature are constant) can be assessed by the change in Gibbs energy for that reaction.

3.1.4 Thermodynamic Description of Mixtures[3, 4]

Mixtures are systems consisting of two or more different chemical species. Whether an equilibrium state of a mixture is homogeneous or heterogeneous is determined by the composition dependence of the entropy and energy changes on mixing. Entropy will always favour mixing, but energetic interactions between the component species can either promote or inhibit mixing.

3.1.4.1 Entropy of Binary Mixing

If we consider the mixing of two small molecules of equal molecular volume, A and B, where the total volume upon mixing is unchanged, as is shown in figure 1, the volume fractions of the components can be expressed as

$$\phi_A = \frac{V_A}{V_A + V_B} \quad \& \quad \phi_B = \frac{V_B}{V_A + V_B} = 1 - \phi_A \tag{3.18}$$
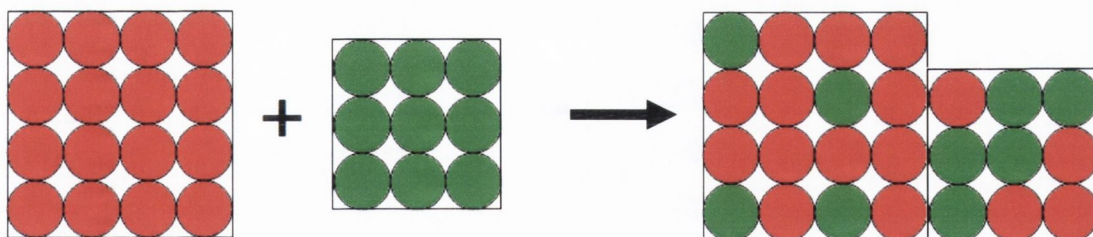
Figure 3.1

Mixing two species, A & B, with no volume change.

The smallest unit defines the lattice site volume v_0 and thus we can say that species A has a molecular volume

$$v_A = N_A v_0 \qquad (3.19)$$

where N_A is the number of lattice sites occupied by A. For this system, $N_A = 1 = N_B$. Using a similar approach for species B, we can say that the total number of lattice sites occupied by the system of volume $V_A + V_B$ is

$$n = \frac{V_A + V_B}{v_0} \qquad (3.20)$$

Using Boltzmann's equation for entropy,

$$S = k \ln \Omega, \qquad (3.21)$$

where $\Omega_{AB} = n$ (i.e. the number of possible states available to the system), and k is the Boltzmann constant, we can express the entropy of mixing for this system as

$$\Delta S_{Mix} = n_A \Delta S_A + n_B \Delta S_B \qquad (3.22)$$

$$\Rightarrow \Delta S_{Mix} = n_A k \ln\left(\frac{n_A + n_B}{n_A}\right) + n_B k \ln\left(\frac{n_A + n_B}{n_B}\right)$$

$$\Rightarrow \Delta S_{Mix} = -k(n_A \ln \phi_A + n_B \ln \phi_B)$$

where $n_A = n\phi_A / N_A$

This can be extended to more complex systems, such as the mixing of polymers. Here, the lattice site volume, v_0, is defined by the smallest units (i.e. solvent units or monomers), and larger molecules occupy connected lattice sites. The molecular volume of such a species is given by equation (3.19). For such a system, the intrinsic entropy of mixing, per lattice site ($\overline{\Delta S_{Mix}} = \Delta S_{Mix} / n$) is given by

$$\overline{\Delta S_{Mix}} = -k\left[\frac{\phi_A}{N_A} \ln \phi_A + \frac{\phi_B}{N_B} \ln \phi_B\right] \qquad (3.23)$$

Systems dealt with in this thesis can be considered similar to a polymer based solution in which $N_A = N$ and $N_B = 1$. As N is such a large number, the first term in equation (3.23) can be considered negligible.

3.1.4.2 Energy of Binary Mixing.

Utilising the simplified lattice model, as per the Flory-Huggins theory[5] [Ψ], we are dealing with a system where the volume is kept constant: the spontaneity of our reaction will concern its Helmholtz energy. The energy of mixing can either be positive (oppose mixing) or negative (promote mixing). The energy of interaction will be given in terms of three pair-wise interactions; u_{AA}, u_{BB}, and u_{AB} between adjacent lattice sites occupied by the two species. A mean field is used to give the average pair-wise interaction U_A of a monomer of species A occupying one lattice site with a neighbouring monomer on one of the adjacent sites. The probability of this neighbour being a monomer of species A is assumed to be the volume fraction ϕ_A of these molecules. The average interaction of an A-monomer with its neighbours as a volume fraction weighted sum of interaction energies;

$$U_A = u_{AA}\phi_A + u_{AB}\phi_B \tag{3.25}$$

B can be treated in a similar manner. The average interaction of an A monomer with all its neighbours is zU_A, where z is the coordination number of the lattice. The average energy per monomer is half this energy due to the fact that every pair wise interaction is counted twice. Taking the number of sites occupied by the species A as $n\phi_A$ and treating B in a similar fashion after summing all the interactions we arrive at the total interaction energy of the mixture:

$$U = \frac{zn}{2}\left[U_A\phi_A + U_B\phi_B\right] \tag{3.26}$$

Combining (3.25) and (3.26) we can express the *total* interaction energy of a binary mixture with n lattice sites:

$$U = \frac{zn}{2}\left(\left[u_{AA}\phi_A + u_{AB}(1-\phi_A)\right]\phi_A + \left[u_{AB}\phi_A + u_{BB}(1-\phi_A)\right](1-\phi_A)\right)$$
$$= \frac{zn}{2}\left[u_{AA}\phi_A^2 + 2u_{AB}\phi_A(1-\phi_A) + u_{BB}(1-\phi_B^2)\right] \tag{3.27}$$

If we account for the interaction energy per site in a pure component A, before mixing as $zu_{AA}/2$, with $n\phi_A$ as the total number of monomers of species A, the total energy of species A before mixing is

---

Ψ   **Flory–Huggins theory**
     A thermodynamic theory of polymer solutions, first formulated independently by Flory and by Huggins, in which the thermodynamic quantities of the solution are derived from a simple concept of combinatorial entropy of mixing and a reduced Gibbs energy parameter, the χ *parameter*'.

$$\frac{zn}{2}u_{AA}\phi_A \tag{3.28}$$

Treating species B in an analogous manner, the total energy of both species before mixing is the sum of the energies of the two components

$$U_0 = \frac{zn}{2}\left[u_{AA}\phi_A + u_{BB}(1-\phi_A)\right] \tag{3.29}$$

If we consider the energy change on mixing per site we arrive at

$$\Delta\overline{U_{Mix}} = \frac{U-U_0}{n} = \frac{z}{2}\phi_A(1-\phi_A)(2U_{AB}-U_{AA}-U_{BB}) \tag{3.30}$$

where z is the coordination number of the species. From this we can define the Flory interaction parameter, χ, used to characterise the difference of interaction energies in a mixture;

$$\chi \equiv \frac{z}{2}\frac{(2u_{AB}-u_{AA}-u_{BB})}{kT} \tag{3.31}$$

Thus the energy of mixing can be written as

$$\Delta\overline{U_{Mix}} = \chi\phi(1-\phi)kT \tag{3.32}$$

Combining (3.32) with the intrinsic entropy of mixing, (3.23), we arrive at the Helmholtz free energy of mixing, per lattice site

$$\Delta\overline{F_{Mix}} = \Delta\overline{U_{Mix}} - T\Delta\overline{S_{Mix}}$$

$$= kT\left[\frac{\phi}{N_A}\ln\phi + \frac{1-\phi}{N_B}\ln(1-\phi) + \chi\phi(1-\phi)\right] \tag{3.33}$$

This equation is referred to as the Flory – Huggins equation[6]. It combines the various entropic and enthalpic factors in terms of a lattice site model. For any reaction to be spontaneous, equation (3.33) must be negative. One of the main aims of this project has been to ascertain whether or not single walled carbon nanotubes can be considered soluble when mixed with particular solvents. To that end, it would have to be shown that the free energy of mixing for the system in question was negative and that the mixed phase was the phase with minimum free energy. As the first two terms in equation (3.33) have entropic origin, they will always be seen to favour mixing (this term may be small for relatively long objects such as polymers). The final term has energetic origins and can be positive (promote mixing), zero (indicating an ideal mixture), or negative (oppose mixing) depending on the sign on the interaction parameter, χ.

If there is a net attraction between species, corresponding to $\chi<0$, a single phase mixture is favourable for all compositions. However, the more common case is for a net repulsion between the species ($\chi>0$). In this case, the equilibrium state of the mixture does

not just depend on the sign of the free energy of mixing (as given by equation (3.33)), but on the functional dependence of the free energy on the composition, ϕ, for the whole range of compositions. This functional dependence, $\Delta \overline{F}_{Mix}(\phi)$, depends on the value of the interaction parameter, χ, and thus it is quite critical to know the value of this parameter. Hildebrand and Scott[7] developed a method for estimating χ for non-polar mixtures with species interacting by dispersion forces. This method is based on the solubility factor, δ, which is related to the energy of vaporisation, ΔE, of a molecule. For a molecule of species A, the solubility parameter can be expressed as

$$\delta_A \equiv \sqrt{\frac{\Delta E_A}{v_A}} \qquad (3.34)$$

where v_A is the volume of molecule A. The $\Delta E_A/v_A$ term is referred to as the cohesive energy density; i.e. the interaction energy per unit volume between the molecules in the pure state A. The interaction energy per site in pure A component A, before mixing is $zu_{AA}/2$. This can be related to the solubility parameter as follows:

$$-\frac{zu_{AA}}{2} = v_0 \frac{\Delta E_B}{v_A} = v_0 \delta_A^2 \qquad (3.35)$$

where v_0 is the volume per site. The minus sign is due to the negative interaction energy; $u_{AA} < 0$. An identical equation can be constructed for a pure B state. The cohesive energy density of interaction between molecules A and B is estimated from the geometric mean approximation[8] (as the predominant cohesive forces between both phases are similar) as being

$$-\frac{zu_{AB}}{2} = v_0 \delta_A \delta_B \qquad (3.36)$$

Subbing equations (3.34) and (3.36) into the definition of the Flory interaction parameter (equation (3.31)) allows it to be expressed in terms of solubility parameter difference[7]

$$\chi \approx v_0 \frac{[\delta_A^2 + \delta_B^2 - 2\delta_A \delta_B]}{kT} = \frac{v_0}{kT}(\delta_A - \delta_B)^2 \qquad (3.37)$$

Consequently, when considering a solvent/solute system, matching the solubility parameter of the solvent and solute would minimise the value in (3.37). This in turn would result in a favourable enthalpic contribution in (3.31) and thus should be conducive to producing a solution. Alternatively, if the solubility parameter difference is too large, the positive heat of mixing contribution to the free energy of mixing is larger then negative entropic contribution. This forms the basis of the 'like dissolves like' concept in chemistry[9]. The solubility parameters of most common solvents are well known[10].

3.2 Interaction of Light with Matter

3.2.1 Introduction[11]

Light can interact with matter in a multitude of ways leading to a vista of optical phenomena that illuminate the world around us. The wide ranging optical properties observed in solid state materials can be classified into a small number of phenomena as shown in figure 1.
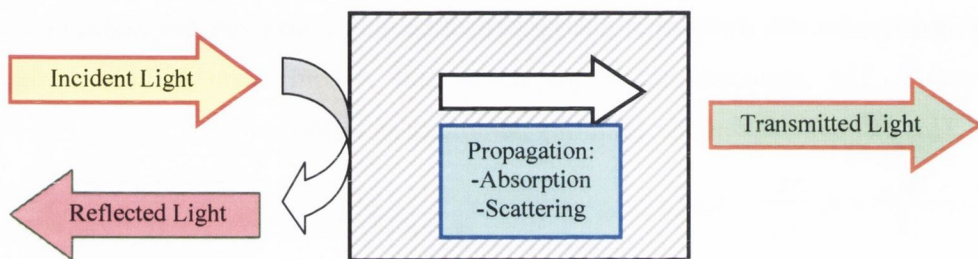
Figure 3.2

Reflection, propagation and transmission of a light beam incident on an optical medium.

A wealth of processes can occur while the light propagates through the medium. The light can be refracted, i.e. the light propagates with a lower velocity than in free space resulting in the light rays bending as described by Snell's Law[12]. If the frequency of the incident light matches the transition frequencies of the atoms in the medium, absorption may occur, resulting in attenuation of the beam. Luminescence may take place following the promotion of the atoms into their excited states. Luminescence is the name given to the de-excitation process that results in the spontaneous emission of light by an excited atom. The light is emitted in all directions with a frequency lower than that of the incident beam. Scattering of the incident beam may also happen as it propagates through the medium. This phenomenon occurs when the light changes direction after interacting with the medium. The total number of photons is unchanged, but the number going in the forward direction decreases as the light dissipates in various other directions. Scattering can be elastic, wherein the frequency of the scattered light is unchanged, or inelastic which is associated with a change of frequency.

3.2.2 Beer-Lambert Law

The ratio of the intensity of light transmitted through a medium, I, to the incident intensity, I_0, at a given frequency is called the transmittance, T. It has been shown empirically[2] that the transmitted light varies with the length, l, of the sample and the concentration, C, of the absorbing species according to the Beer-Lambert law:

$$I = I_0 10^{-\alpha Cl} \qquad (3.38)$$

where α is known as the extinction coefficient (or the molar absorption coefficient). Figure 3 shows the attenuation of an beam of light through a cuvette, due to absorption as outlined by the Beer-Lambert law.
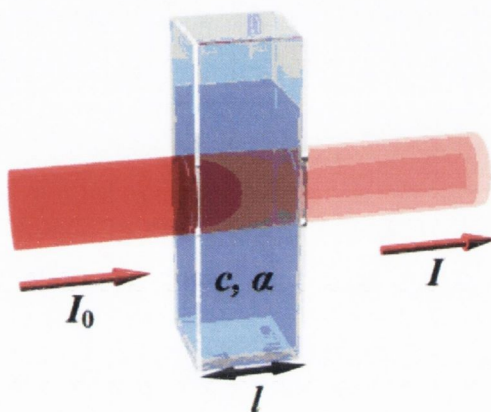
Figure 3.3

Representation[13] of Beer-Lambert law, showing the various components as outlined in equation (3.38).

The absorbance, A, can be defined as

$$A = \log \frac{I_0}{I} \qquad (3.39)$$

and so the Beer-Lambert law takes its usual form

$$A = \alpha Cl \qquad (3.40)$$

showing the absorbance in a sample to be reliant on the concentration of the sample and the thickness of the sample that the light is transmitted through.

3.2.3 Electronic Bands & Density of States[14]

Within a solid, the atoms are packed very close to one another such that the typical inter-atomic separation is of the order of one atom. This results in the outer orbitals of the atoms interacting with one another. This then broadens the discrete energy levels,

associated with electrons in individual atoms, into bands. Optical transitions can take place between electronic bands if they are allowed by the selection rules (which shall be discussed below). Interband absorption is thus possible over a large range of wavelengths determined by the lower and upper energy limits of the bands. The continuum of states associated with these bands leads to continuous absorption and emission bands. From this we can express the number of states within a given energy range as

$$\text{Number of states in range } E \rightarrow (E + dE) = g(E)dE \qquad (3.41)$$

This is known as the density of states. This can be also expressed as

$$g(E) = g(k)\frac{dk}{dE} \qquad (3.42)$$

Where k is the wave number $\left(k \equiv \frac{2\pi}{\lambda} = \frac{p}{\hbar} = \frac{\sqrt{2mE}}{\hbar} \right)$ (for free/nearly-free electrons) thus

$g(E)$ can be evaluated from knowledge of the E-k relationship for the electrons or phonons.

3.2.4 Interband Absorption[11, 15]

The energy level diagram of isolated atoms consists of series of states with discrete energies. Optical transitions between these lines give rise to sharp lines in the absorption and emission spectra and can be described well by the classical oscillator model. However, the classical model has difficulty in dealing with the continuous bands associated with the solid state. Figure 3.4 shows a simplified energy diagram of two separate bands in a solid.
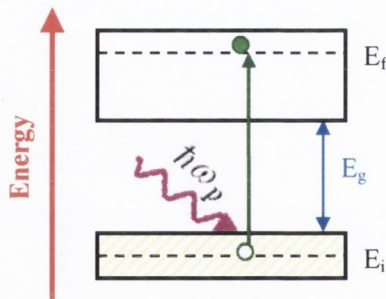
Figure 3.4

Interband optical absorption of photon (of energy $\hbar\omega_p$) causes a transition between an initial state of energy E_i, in an occupied lower band and a final state at energy E_f in an empty upper band. The bandgap, E_g, is shown for completion.

The optical absorption coefficient is determined by the quantum mechanical transition rate $W_{i \to f}$ for exciting an electron in an initial quantum state ψ_i to a final state ψ_f by absorption of a photon of angular frequency ω. This transition rate is given by Fermi's golden rule[11, 16]:

$$W_{i \to f} = \frac{2\pi}{\hbar} |M|^2 g(\hbar\omega) \tag{3.43}$$

where $g(\hbar\omega)$ is the density of states. $|M|^2$ can be expressed as

$$|M|^2 = |eE_0(\omega) \bullet r_{fi}|^2 = |E_0(\omega)|^2 |D_{fi}(\omega)|^2 \tag{3.44}$$

Where $D_{fi}(\omega)$ is a matrix element of the component of the dipole moment operator parallel to the electric field: r is the position vector, e the magnitude of the electron charge and E_0 the electric field.

The concept of 'selection rules'[2] for atomic transitions can also be extended to larger systems. These rules serve to determine whether or not a transition is forbidden or allowed. As outlined above, the semi-classical idea is that, for a molecule to be able to interact with the electromagnetic field and absorb or create a photon of frequency, ν, it must posses a dipole oscillating at that frequency. This transient dipole moment is expressed in equation (3.44). The size of the transition dipole can be regarded as a measure of the charge redistribution that accompanies a transition: a transition will be active (i.e. generate or absorb photons) only if the accompanying charge is dipolar. Fermi's golden rule leads us to selection rules, as only a transition with a nonzero moment can contribute to the spectrum. Thus, in order to identify specific selection rules, the conditions for which $M \neq 0$ must be established[11].

Absorbance spectroscopy thus probes the interaction of electromagnetic radiation with matter. This is accomplished by monitoring the transmittance through a sample as a function of wavelength of the incident light. The resulting spectrum acts as a molecular plan of the sample as various molecular components will be active at differing wavelengths.

3.2.5 Absorbance of One Dimensional Objects[17]

One dimensional materials, such as carbon nanotubes, have sharp peaks in their density of states known as Van Hove singularities[18]. Figure 3.5 shows the density of electronic states for a (4,2) carbon nanotube. These features are characteristic of the dimensionality of such objects and give rise to sharp peaks in resulting absorbance spectra

due to the narrowing of the bands[19]. Each (n,m) carbon nanotube exhibits a different set of van Hove singularities in its valence and conduction bands and hence a different set of electronic transition energies between its valence- and conduction-band van Hove singularities. For this reason optical experiments can be employed to determine the (n,m) structure of a given carbon nanotube.
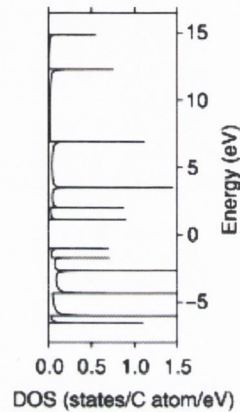
Figure 3.5

Density of electronic states for a (4,2) carbon nanotube[17].

Despite the large number of van Hove singularities in the valence and conduction bands of the carbon nanotube shown in figure 3.5 very few optical transitions are allowed when selection rules are considered[20, 21]. As described previously[19], the circumferential wave vector in a carbon nanotube is given by $\mathbf{k}_x = 2J/d$, where d is the diameter of the nanotube and J is the quantised angular momentum and serves as the sub-band index (J = 1,2,....N, where N= number of hexagons that lie within the nanotubes unit cell). Selection rules for the angular momentum involve the polarisation direction. For the case where the incident electric field is parallel to the tube axis, $\Delta J=0$. This means that only the vertical transitions from the π to π^* sub-bands of the same J values are permitted. Furthermore, if the field is perpendicular to the tube axis, excitations are restricted to sub-bands that satisfy $\Delta J=\pm 1$. Another selection rule arises when we consider the unit wave vector along the nanotube axis, $\mathbf{k}_y$: for any permissible transition, $\Delta k_y=0$ (conservation of momentum). SWNTs can be classified in three different groups according to whether mod(2n+m,3)= 0, 1, or 2 (i.e. the remainder when 2n+m is divided by 3). Mod 1 and Mod 2 nanotubes are semiconducting, whilst Mod 0 nanotubes are metallic at room temperature. It should be remembered that n=m nanotubes are truly metallic. Transitions of the type E_{ii} (where E is

the energy of the transition and i= integer, J) account for most of the absorption spectra due to the strong anisotropy of the optical absorption. Figure 3.6 shows a typical absorption spectrum recorded and analysed by Hagen et al[21] where $E_{11}^{Semiconducting}$, $E_{22}^{Semiconducting}$, and $E_{11}^{Metallic}$ are highlighted as regions A, B, and C respectively.
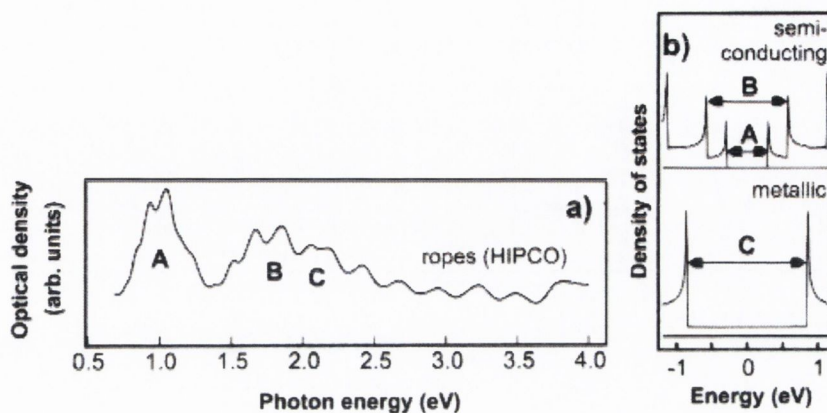
Figure 3.6

(a) UV-Vis-NIR Absorption spectrum of SWNTs[21] where features A, B and C are attributed to symmetric transitions between the lowest sub-bands in semiconducting (A & B) and metallic (C) nanotubes. (b) The corresponding density of states (DOS) for such transitions.

3.2.6 The Fate of Electronically Excited States - Luminescence[11]

Following the creation of an electronically excited state, we must consider its fate. The most common outcome for such states is nonradiative decay in which the excess energy is transferred into the vibration, rotation, and translation of the surrounding molecules. This thermal degradation converts the excitation energy into thermal motion of the environment, i.e. heat. A radiative decay process is also possible in which a molecule spontaneously discards its energy as a photon. Figure 3.7 outlines the main processes involved in the decay of excited states.
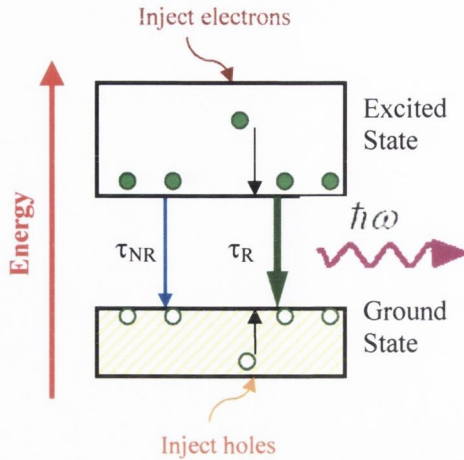
Figure 3.7

General scheme for radiative and nonradiative decay in a solid. Electrons are injected into the excited state band and relax to the lowest available level before dropping down to empty levels in the ground state. The diagram shows a photon, of energy $\hbar\omega$ being emitted. Both the radiative and nonradiative recombination rates are determined by their respective lifetimes τ_R and τ_{NR}.

A photon is emitted when an electron in an excited state drops down into an empty state in the ground state band. In order for this to occur, electrons must be first injected into the excited state (by a process such as absorption) and correspondingly holes must be injected into the ground state (otherwise the Pauli exclusion principle would be violated, as we cannot put two electrons into the same level). The spontaneous emission rate for radiative transitions is determined by the Einstein A coefficient[22]. Thus, if the upper level has a population N at a time t, the radiative decay is given by:

$$\left(\frac{dN}{dt}\right)_{Radiative} = -AN \tag{3.45}$$

This shows us that the number of photons emitted in a given time is proportional to both the Einstein A coefficient and the population of the upper level. Furthermore, it can be shown that the Einstein A coefficient is directly proportional to the B coefficient, that determines the absorption probability[11]. This means that the transitions which have large absorption coefficients also have high emission probabilities and short radiative lifetimes. It should be noted that the fact that absorption and emission probabilities are closely linked does not imply that the absorption and emission rates are the same. The difference can be seen by the population term in equation (3.45) which implies that a transition might have a

high emission probability, but no light will be emitted unless the upper level is populated. We can summarise these factors by stating the luminescent intensity I, at frequency v, as:

$$I(hv) \propto |M|^2 g(hv) \times level \: occupancy \: factors \qquad (3.46)$$

Where the occupancy factors give the probabilities that the upper level is occupied and the lower level is empty. The first two terms are the matrix element and density of states as given by Fermi's golden rule, equation (3.43).

As outlined above, the absorption of a photon by an interband transition in a semiconductor or insulator creates an electron in the conduction band and a hole in the valence band. The oppositely charged particles are created at the same point in space and can attract each other through their mutual Coulomb interaction. This attractive interaction increases the probability of the formation of an electron hole pair, and thus increases the optical transition rate. If the right conditions are met a bound electron hole pair can be formed: this is known as an exciton. Excitons can have a strong influence on the optical properties of molecular materials.

3.2.7 Carbon Nanotube Luminescence

The observation of luminescence from isolated single-walled carbon nanotubes (SWNTs)[23, 24] has made possible the observation of the $E_{11}^{Semiconducting}$ energy gap for semiconducting SWNTs. 3D plots such as that shown in figure 3.8 can be constructed showing the spectral interdependence of the excitation and emission energies. The absorption/emission intensity is given on the vertical axis, and the intense peaks, indicating strong optical absorption at a given E_{ii} and emission at E_{11}, are each related to one specific (n,m) SWNT chirality. Excitons in one-dimensional semiconductors have been shown to significantly lower the optical transition energies by a substantial amount[25]. Optical excitation of semiconducting single SWNTs generates relatively strongly bound excitons whose spatial dimensions are predicted to be a few nanometers. Furthermore, light emission from carbon nanotubes has been shown to be dominated by excitonic recombination[26, 27]. Thus, significant consideration should be given to such excitonic systems when considering the luminescence of SWNTs, particularly with regard to quenching.
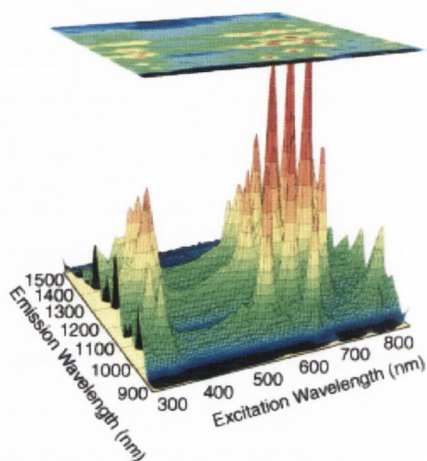
Figure 3.8

Fluorescence intensity versus excitation and emission wavelengths for SWNTs in an aqueous sodium do-decyl sulphate suspension.[24] Each peak corresponds to absorption/emission of a single (n,m) SWNT.

3.3 Experimental Methods

3.3.1 Uv-Vis-NIR Absorbance Spectrometry[2, 28]

UV-Vis-NIR absorbance spectroscopy was used in this work to probe electronic transitions between the energy levels of SWNTs, the nature of which have been described earlier in this work. A Cary 6000i instrument was used to that end. A diagram outlining the various components of an absorbance spectrometer is shown in figure 3.9. A beam of light from a broad spectrum source (Xe lamp) is separated into its component wavelengths by a monochromator. A slit at the entrance to the monochromator results in a regulated spot-size of collominated light being incident on the diffraction grating. When the polychromatic beam reaches the grating, diffraction effects take place so that the angle at which each spectral component is reflected depends on its particular wavelength. The actual relationship between the reflected angle and the wavelength is given by the characteristics of the grating used, or the groove density. Consequently, for a fixed position of the grating only one wavelength of in the incoming beam will reach the exit slit. The grating pivots relative to the broad-spectrum incident light resulting in monochromatic beams being reflected off its grooved surface. This reflected light is again passed through an exit slit (both slits act to control the spectral dependence of the monochromator). Each monochromatic beam, in turn, is split into two equal intensity beams by a half-mirrored device. One beam is passed through a reference cell filled with the solvent to be used whilst the other is passed through the sample. The intensities of both beams are measured, having passed through the cells, as I_0 and I respectively. The amount of light absorbed at a particular wavelength is deduced from the Beer-Lambert law as described previously in this thesis. The monochromator scans through a wide range of wavelengths (from ultra violet to near infrared) allowing the absorbance of the sample to be monitored as a function of wavelength probing various optical properties of the system in question.
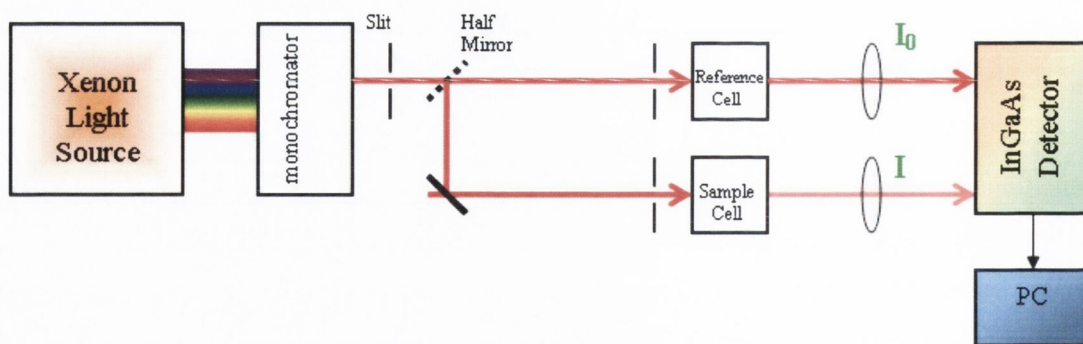
Figure 3.9

Basic outline of UV-Vis-NIR absorbance spectrometer.

3.3.2 Photoluminescence Spectroscopy[2]

The emission of light from dispersed, individual, SWNTs, as outlined in the previous chapter, was monitored in this thesis by an Edinburgh Instruments FLS900 Fluorescence Spectrometer. Photoluminescence spectra, (plotting luminescence intensity versus excitation wavelength and emission wavelength) were recorded with an experimental arrangement such as that shown in 3.10
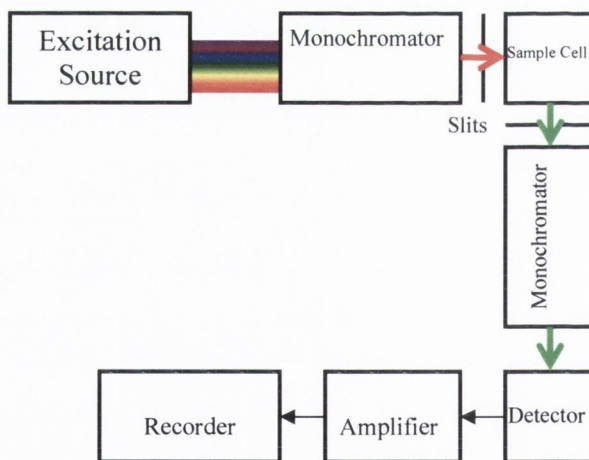
Figure 3.10

Schematic of Photoluminescence spectrometer.

A broad spectrum of light from the excitation source passes through a monochromator (or two) that selects a specific excitation wavelength and bandwidth. This is then directed through a beam splitter where a small amount of light is reflected onto a reference detector. The beam continues through an iris so the intensity of the beam can be controlled, through a slit, and finally the incident excitation beam is focused on the sample.

A portion of any emitted light from the sample is collected at 90° to the incident light, passed through another slit, and is focused on the emission monochromator. The emission monochromator selects a wavelength and spectral bandwidth of this emission and finally the beam passes into a detector. The choice of detector is governed by the wavelength of the emitted light. A cooled InGaAs detector was chosen for the experimental setup described in this work as it allows the detection of weak light in the near infrared region – the region where individual SWNTs are known to emit[23].

3.3.3 Cross Polarisation Microscopy[29]

The biphasic nature of nanotube dispersions[30] were investigated, as part of this work, with cross polarisation microscopy. Polarised light microscopy serves as an excellent method to distinguish between isotropic and anisotropic materials[31]. The technique exploits optical properties of anisotropy to reveal detailed information about the structure and composition of materials.

Isotropic materials, which include gases, liquids, unstressed glasses and cubic crystals, demonstrate the same optical properties in all directions. They have only one refractive index and no restriction on the vibration direction of light passing through them. Anisotropic materials, in contrast, which include 90% of all solid substances, have optical properties that vary with the orientation of incident light with respect to the crystallographic axes. They demonstrate a range of refractive indices depending both on the propagation direction of light through the substance and on the vibrational plane coordinates. The basic outline of the experimental setup is shown in figure 3.11. Samples in this work were monitored with a Leica Microscope fitted with a JVC colour video camera.
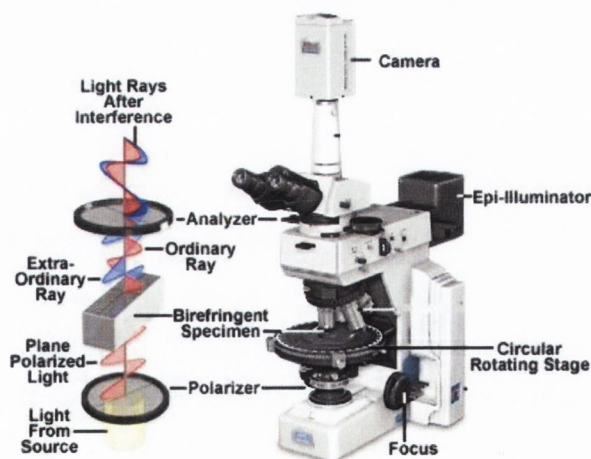
Figure 3.11

Experimental set-up for cross polarisation microscopy[32]

3.3.4 Transmission Electron Microscopy (TEM) & High-Resolution Transmission Electron Microscopy (HRTEM)[33]

The lengths of SWNT bundles were measured in this work via TEM[φ] using a Hitachi H-7000. The nature of dispersed, individual SWNTs as well as small bundles of SWNTs was investigated with HRTEM[φ]: measurements were made with a FEI Tecnai F20.

The operation of a TEM is quite similar to that of a light-microscope. The resolution of a light microscope is limited by the wavelength of the light incident on the sample. The TEM utilises electrons as its 'light source' with their much shorter wavelengths allowing resolution approximately 1000 times higher than a conventional light microscope. Figure 3.12 shows the main components in a TEM.
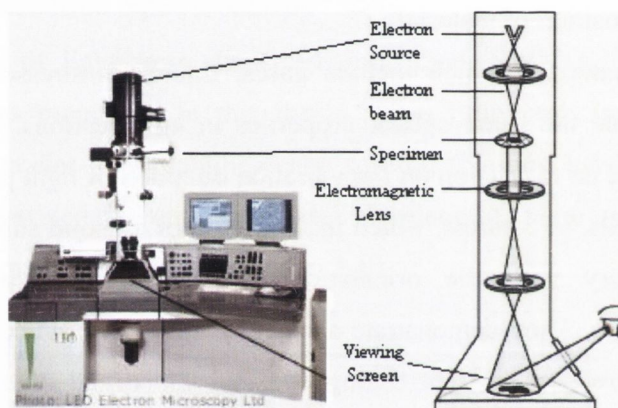
Figure 3.12
Transmission Electron Microscope[34]

The electron gun at the top of the microscope emits the electrons that travel through vacuum in the column of the microscope. Instead of glass lenses focusing the light as in the light microscope, the TEM uses electromagnetic lenses to focus the electrons into a very thin beam. The electron beam then travels through the specimen in question. Depending on the density of the material present, some of the electrons are scattered and disappear from the beam. At the bottom of the microscope the unscattered electrons hit a fluorescent screen, which gives rise to a 'shadow image' of the specimen with its different parts displayed in varied darkness according to their density. The image can be studied directly by the operator or photographed with a camera.

φ Experiments were carried out by Dr. Valeria Nicolosi, Sch. of Physics, TCD.

HRTEM can provide images with atomic resolution. As opposed to conventional microscopy, HRTEM does not use amplitudes, e.g. absorption by the sample, for image formation. Instead, contrast arises from the interference in the image plane of the electron wave with itself. The use of a larger objective aperture (or no aperture), as shown in figure 3.13, results in the formation of an image by the interference of many diffracted beams Due to our inability to record the phase of these waves, the amplitude resulting from this interference is generally measured, however the phase of the electron wave still carries the information about the sample and generates contrast in the image, thus the name 'phase-contrast imaging'.
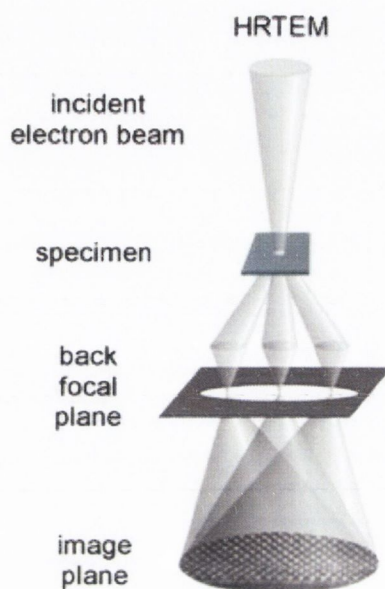
Figure 3.13
Basic outline of High Resolution Transmission Electron Microscope. Note the large aperture that allows the formation of an image by the interference of many diffracted waves.

3.3.5 Resonance Raman Spectroscopy[2, 35]

In Raman spectroscopy, the energy levels of a system are explored by examining the inelastic scattering of photons by molecules. Typically, this involves a monochromatic beam being reflected off (or passed through) a sample and the radiation that is scattered perpendicular to the beam being monitored, as seen in figure 3.14. These scattered photons are accounted for by the lower-frequency Stokes radiation from the sample. Other photons may collect energy from the molecules, if they are already excited and emerge as higher-

frequency anti-Stokes radiation. The component of radiation scattered in the forward direction is known as Rayleigh radiation. As the shifts in frequency of the scattered radiation are so small, it is very important that the incident light be monochromatic in order for the shifts to be observed. The energy shift yields information on the phonon modes in the system. For a vibration motion to be Raman active, the polarisability of the molecule must change with the vibrational direction[36]. Raman spectroscopy is commonly used in chemistry, since vibrational information is very specific for the chemical bonds in molecules. It can act as a fingerprint for the identification of molecules or specific components of larger systems. Infrared and Raman spectroscopy both measure the vibrational energies of molecules but these methods rely on different selection rules. It should be recalled that for a vibration motion to be infrared active, the dipole moment of the molecule must change. Thus, Raman spectroscopy complements infrared spectroscopy.
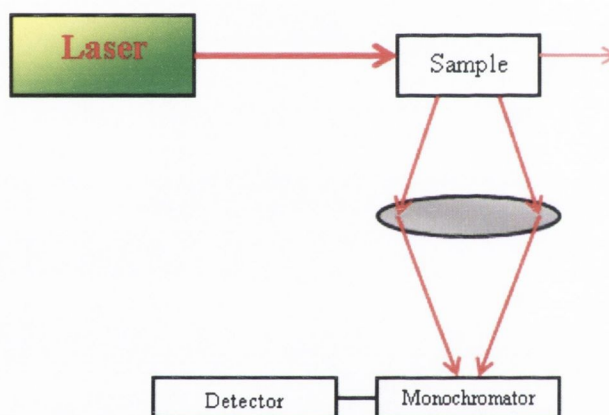
Figure 3.14

Experimental setup for Raman spectroscopy. The scattered radiation is monitored at right angles to the incident radiation.

Resonance Raman spectroscopy involves a slight modification of the procedure outlined above, whereby the incident radiation coincides with the frequency of an electronic transition, as illustrated in figure 3.15. It is characterised by a much greater intensity in the scattered radiation when compared with conventional Raman. However, as fewer vibrational modes contribute to the scattering, the spectrum is very much simplified.
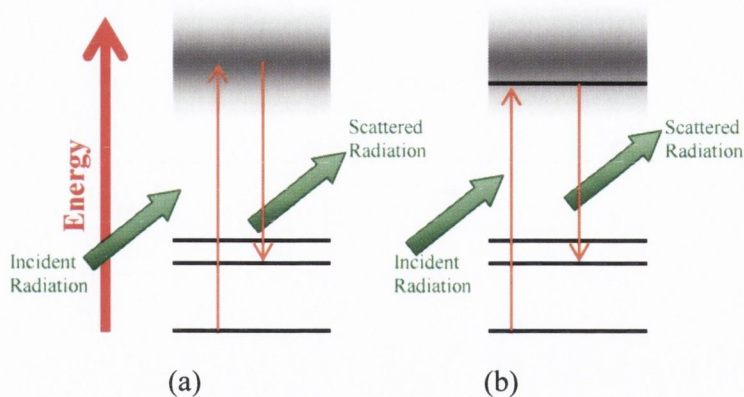
Figure 3.15

(a) In conventional Raman spectroscopy, the incident radiation does not match an absorption frequency. However, in the case of resonant Raman spectroscopy, (b), the incident radiation has a frequency that coincides with a molecular transition.

Active Raman modes have been extremely well characterised for SWNTs[37, 38] and have been employed to determine the diameter of individual SWNTs and consequently the (n,m) chirality of individual SWNTs. Furthermore, other Raman active modes have been used to monitor the degree of defects or functional groups present on SWNTs[39]. Raman spectroscopy in this thesis was carried out using a Jobin Yvon Raman system fitted with a HeNe 20 mW laser (λ = 532nm).

3.3.6 Scanning Electron Microscopy (SEM)[40]

The SEM permits the observation and characterisation of materials on a nanometre to micrometre scale. It allows topographical images of samples to be taken with relative ease. In this work, SEM was used to image the orientation of SWNT bundles, offering a step-back from the more focused AFM and TEM based images. SEM was carried out on a Hitachi S-4300.

In SEM the area to be examined is irradiated with a finely focused beam of electrons that can be rastered across the surface of the sample. Various signals can be produced from the interaction of the electron beam with the surface, but generally secondary electrons are monitored, as they vary primarily as a result of differences in surface topography. The secondary electron emission, which is confined to a very small volume near the impact beam, permits images to be obtained at a resolution approximating the size of the focused electron beam. The spatial resolution of the SEM depends on the

electron beam spot size, which in turn depends on the optics of the system. As the spot size and the interaction volume are very large compared to the distances between atoms, the SEM is not capable of atomic scale imaging (as seen with TEM).

3.3.7 Atomic Force Microscopy

The operation of the atomic force microscope (AFM) can be best described as imaging samples by 'feeling' rather than 'looking' as a blind person would build up an image in his or her head by touching a surface. This method of image does not just yield a topographical outline of the surface but also yields information on its texture.

3.3.7.1 AFM – Apparatus[41, 42]

The basic outline of the AFM apparatus is shown in figure 1[43].
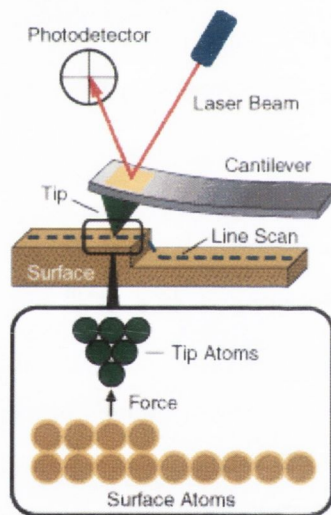
Figure 3.16

Schematic representation of the atomic force microscope showing the crucial components.

The first and most important part of the AFM is the tip which feels the surface. A tip consists of a micro-fabricated sharp spike mounted at the end of a cantilever. Its sharpness determines the resolution of the instrument and the cantilever on which it's mounted allows the tip to move vertically. The entire cantilever-tip assembly is generally made from silicon or silicon nitride as they are both hard and robust for the microfabrication method.

The second crucial feature of the AFM is the scanning mechanism. This is realised by means of a piezoelectric transducer that converts an applied potential difference into a

physical force. This motion is incredibly reproducible and sensitive such that the piezoelectric device can be made to move with an accuracy of atomic dimensions.

The final feature of the instrument is the detection mechanism. The motion of the tip as it transverses the sample must be monitored. The simplest method employed to do this is the optical lever system. Here a laser beam is focused onto the end of the cantilever, over the tip, and then reflected onto a photodiode detector. The photodiode is split into four segments. As the tip moves in response to the samples topography during scanning, the angle of the reflected beam changes in intensity in each of its quadrants. This mechanical amplifier is accurate enough to detect atomic scale movement of the tip as it rasters across the samples surface. The segments produce an electrical signal which quantifies the vertical motion of the tip, and the difference between the laser intensity in the left and right pair of segments quantifies the lateral motion of the tip.

When the sample is scanned, the topography of the sample causes the cantilever to bend as the force between the tip and the sample is changed. In the simplest operating mode, the cantilever's deflection is maintained at a constant predefined level by a control loop which moves the sample or the tip in the appropriate direction at each imaging point. Thus, the feedback mechanism is crucial to generating an image.

3.3.7.2 AFM – Theory of Operation [2, 41, 42, 44, 45]

As the AFM rasters across the surface of a sample feeling an image, it does so by the tip sensing changes in force between the tip and the surface. Depending on whether the cantilever is sensing repulsive or attractive forces, different image modes can be applied. At this scale the forces that concern us are Van der Waals. These forces are the interactions between molecules that leave their chemical identities unchanged. They include the interactions between partial charges of polar molecules. There are also repulsive interactions that prevent the complete collapse of matter, arising from the Pauli exclusion principle. With AFM, it is possible to characterise both attractive and repulsive parts of the force-distance relationship between the tip and the sample by modelling the interaction. This involves the variation of the potential energy of one particle, say at the apex of the tip, due to the interaction with a particle at the surface of the sample. As their separation (r) changes, so does the value of the potential energy, which can be described by the pair potential energy function, $E^{Pair}(r)$. A special case of the 'Mie' pair-potential energy function is used to model this behaviour called the Lennard-Jones or '6-12' function:

$$E^{Pair}(r) = 4\varepsilon\left[\left(\frac{\sigma}{r}\right)^{12} - \left(\frac{\sigma}{r}\right)^6\right] \tag{3.47}$$

which is represented in figure 3.17 where ε is the depth of the potential well and σ is approximately equal to the diameter of the atoms involved, also known as the hard-sphere diameter. The first term, $1/r^{12}$, represents repulsion accounting for the steep increase in $E^{pair}(r)$ at small seperations. The second term, $1/r^6$, is responsible for the slower change in attractive behaviour at larger separations.
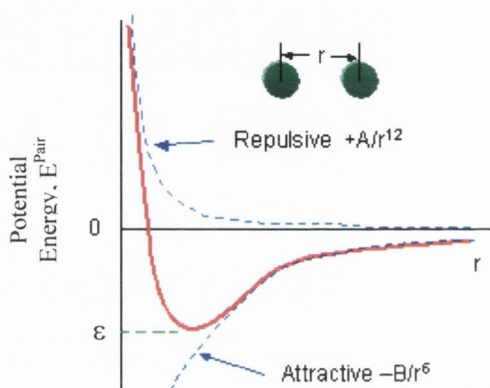
Figure 3.17

A graphical representation of the Lennard Jones Potential[46] between two atoms.

The variety of imaging modes when using AFM are differentiated by the force interaction involved in each case. The contact mode where the tip scans the sample in close contact with the surface is the most common mode used in the force microscope. The force on the tip is repulsive with a mean value of 10^{-9} N. Atomic resolution is possible using this method but problems with contact mode are caused by excessive tracking forces applied by the probe to the sample. Non-contact mode is used in situations where tip contact might alter the sample in subtle ways. In this mode the tip hovers 50 - 150 Angstrom above the sample surface. Attractive Van der Waals forces acting between the tip and the sample are detected, and topographic images are constructed by scanning the tip above the surface. Unfortunately the attractive forces from the sample are substantially weaker than the forces used by contact mode and image quality suffers as a consequence. Finally, tapping mode is a potent technique that allows high resolution topographic imaging of sample surfaces that are easily damaged, loosely held to their substrate, or difficult to image by other AFM techniques. Tapping mode overcomes problems associated with friction, adhesion, electrostatic forces, and other difficulties that an plague conventional AFM scanning

methods by alternately placing the tip in contact with the surface to provide high resolution and then lifting the tip off the surface to avoid dragging the tip across the surface. Tapping mode imaging is implemented in ambient air by oscillating the cantilever assembly at or near the cantilever's resonant frequency using a piezoelectric crystal. The piezoelectric motion causes the cantilever to oscillate with a high amplitude(typically greater than 20nm) when the tip is not in contact with the surface. The oscillating tip is then moved toward the surface until it begins to lightly touch, or tap the surface. During scanning, the vertically oscillating tip alternately contacts the surface and lifts off, generally at a frequency of 50,000 to 500,000 Hz. As the oscillating cantilever begins to intermittently contact the surface, the cantilever oscillation is necessarily reduced due to energy loss caused by the tip contacting the surface. The reduction in oscillation amplitude is used to identify and measure surface features. During tapping mode operation, the cantilever oscillation amplitude is maintained constant by a feedback loop. Selection of the optimal oscillation frequency is software-assisted and the force on the sample is automatically set and maintained at the lowest possible level. When the tip passes over a bump in the surface, the cantilever has less room to oscillate and the amplitude of oscillation decreases. Conversely, when the tip passes over a depression, the cantilever has more room to oscillate and the amplitude increases (approaching the maximum free air amplitude). The oscillation amplitude of the tip is measured by the detector and input to the controller electronics. The digital feedback loop then adjusts the tip-sample separation to maintain a constant amplitude and force on the sample.

One dimensional objects, such as carbon nanotubes have been observed[47], characterized and manipulated[48] using AFM. As with all microscopic techniques, care in sample preparation has been shown to be of paramount importance. Substrates such as mica[49], highly order pyrolytic graphite (HOPG)[50], and silicon[51] have all be shown to be suitable for SWNT imaging.

3.4 References

1. Fermi, E. Thermodynamics (Dover Publications, Inc., New York, 1936).
2. Atkins, P. W. Physical Chemistry (Oxford University Press, 1998).
3. Rubinstein, M. & Colby, R. H. Polymer Physics (Oxford University Press, Oxford, 2003).
4. Hildebrand, J. H., Prausnitz, J. M. & Scott, R. L. Regular and related solutions (Van Nostrand Reinhold Company, New York, 1970).

5.   Cowie, J. M. G. Polymers: Chemistry and Physics of Modern Materials (Nelson Thornes).

6.   Flory, P. J. Principles of Polymer Chemistry (Cornell University Press, Ithaca, New York, 1953).

7.   Hildebrand, J. H. & Scott, R. L. The Solubility of Non-electrolytes (Reinhold, New York, 1950).

8.   Girifalco, L. A. & Good, R. J. A Theory for the Estimation of Surface and Interfacial Energies. I. Derivation and Application to Interfacial Tension. J. Phys. Chem. 61, 904-909 (1957).

9.   Van-Dijk, M. A. & Wakker, A. Concepts of Polymer Thermodynamics.

10.   Brandrup, J., Immergut, E. H., Grulke, E. A., Akihiro, A. & Bloch, D. R. Polymer Handbook (1999).

11.   Fox, M. Optical Properties of Solids (Oxford University Press Inc., New York, 2001).

12.   Hecht, E. Optics (Addison-Wesley, 2002).

13.   www.answers.com.

14.   Ashcroft, N. & Mermin, N. Solid State Physics (Saunders College Publishing, 1976).

15.   Bohren, C. F. & Huffman, D. R. Absorption and Scattering of Light by Small Particles (John Wiley & Sons, 1983).

16.   Dirac, P. A. M. The Quantum Theory of Emission and Absorption of Radiation. Proceedings of the Royal Society of London Series a-Mathematical and Physical Sciences 114, 243-265 (1927).

17.   Jorio, A. et al. Carbon Nanotube Photophysics. MRS Bulletin, 276-280 (2004).

18.   Saito, R. & Fujita, M. Electronic structure of chiral graphene tubules. Applied Physics Letters 60, 2204 (1992).

19.   Dresselhaus, M. S. Carbon Nanotubes: Synthesis, Structure, Properties and Applications (Springer-Verlag, Berlin, 2001).

20.   Lin, M. F. Optical Spectra of Single-Wall Carbon Nanotube Bundles. Physics Review B 62, 153-159 (2000).

21.   Hagen, A. & Hertel, T. Quantitative analysis of optical spectra from individual single-wall carbon nanotubes. Nano Letters 3, 383-388 (2003).

22.   Hilborn, R. C. Einstein Coefficients, cross sections, f values, dipole moments, and all that. American Journal of Physics 50 (1982).

23.   O'Connell, M. J. et al. Band gap fluorescence from individual single-walled carbon nanotubes. Science 297, 593-596 (2002).

24.   Bachilo, S. M. et al. Structure-assigned optical spectra of single-walled carbon nanotubes. Science 298, 2361-2366 (2002).

25.   Pedersen, T. G. Variational approach to excitons in carbon nanotubes. Physical Review B 67, 073401 (2003).

26.   Vasili, P., Tersoff, J. & Phaedon, A. Scaling of Excitons in Carbon Nanotubes. Physical Review Letters 92, 257402 (2004).

27.   Cognet, L. et al. Stepwise Quenching of Exciton Fluorescence in Carbon Nanotubes by Single-Molecule Reactions. Science 316, 1465-1468 (2007).

28.   Cary. Cary 6000i User Manual.

29.   Murphy, D. B. Fundamentals of Light Microscopy and Electronic Imaging (Wiley, 2001).

30.   Song, W. H., Kinloch, I. A. & Windle, A. H. Nematic liquid crystallinity of multiwall carbon nanotubes. Science 302, 1363-1363 (2003).

31.   Hurt, R. H. & Chen, Z. Physics Today 53 (2000).

32. See. http://www.olympusmicro.com/primer/techniques/polarized/cx31polconfiguration. html.

33. Spence, J. C. H. High Resolution Electron Microscopy (Oxford Science Publications, 2003).

34. LED Electron Microscopes Ltd.

35. Pelletier, M. J. Analytical Applications of Raman Spectroscopy (1999).

36. Herzberg, G. Infrared and Raman Spectra of Polyatomic Molecules (Van Nostrand Reinhold, New York, 1945).

37. Dresselhaus, M. S., Dresselhaus, G., Jorio, A., Filho, A. G. S. & Saito, R. Raman Spectroscopy on Isolated Wingle Wall Carbon Nanotubes. Carbon 40, 2043-2061 (2002).

38. Dresselhaus, M. S., Dresselhaus, G., Pimenta, M. A. & Eklund, P. C. Raman Scattering in Carbon Materials (1999).

39. Strano, M. S. et al. Assignment of (n, m) Raman and Optical Features of Metallic Single-Walled Carbon Nanotubes. Nano Lett. 3, 1091-1096 (2003).

40. Goldstein, J., Newbury, D., Joy, D., Lyman, C. & Echlin, P. Scanning Electron Microscopy and X-Ray Microanalysis (Kluwer Academic / Plenum Publishers, New York, 2003).

41. Wiesendanger, R. Scanning Probe Microscopy and Spectroscopy: Methods and Applications (Cambridge University Press, 1998).

42. Chen, C. J. Introduction to Scanning Tunneling Microscopy (Oxford University Press, 1993).

43. www.molec.com/media/images/AFM-Schematic.gif.

44. Bonnell, D. Scanning Probe Microscopy and Spectroscopy: Theory, Techniques, and Applications (Wiley-VCH, New York, 2001).

45. Morris, V. J. Atomic Force Microscopy for Biologists (Imperial College Press, 2000).

46. See. http://employees.csbsju.edu/hjakubowski/classes/ch331/protstructure/ilennardjones 2.gif.

47. Hoper, R. et al. Single-Shell Carbon Nanotubes Imaged by Atomic-Force Microscopy. Surface Science 311, L731-L736 (1994).

48. Stevens, R. M. D. et al. Carbon nanotubes as probes for atomic force microscopy. Nanotechnology 11, 1-5 (2000).

49. Furtado, C. A. et al. Debundling and dissolution of single-walled carbon nanotubes in amide solvents. Journal of the American Chemical Society 126, 6095-6105 (2004).

50. Takahashi, H., Numao, S., Bandow, S. & Iijima, S. AFM imaging of wrapped multiwall carbon nanotube in DNA. Chemical Physics Letters 418, 535-539 (2006).

51. Giordani, S. et al. Debundling of single-walled nanotubes by dilution: Observation of large populations of individual nanotubes in amide solvent dispersions. Journal of Physical Chemistry B 110, 15708-15718 (2006).

Chapter 4

Debundling of Single-Walled Nanotubes by Dilution: Observation of Large Populations of Individual Nanotubes in Amide Solvent Dispersions [1]

4.1 Introduction

The purpose of this thesis is to produce, characterise and garner an understanding of stable dispersions of SWNTs. This chapter illustrates the dispersive capabilities of the amide solvent N-Methyl-Pyrrolidone (NMP). A reliable, repeatable method is outlined showing the debundling of SWNTs by dilution, yielding highly stable populations of individual SWNTs.

4.2 Background

Perhaps the most desirable scenario for the debundling of SWNTs would involve the discovery of a solvent in which nanotubes are thermodynamically soluble i.e. where the free energy of mixing is negative. Failing that, it would be advantageous to identify a solvent in which nanotubes could be dispersed down to the level of individual nanotubes or small bundles stably for reasonable periods of time. A number of reports of such solvents have appeared in recent literature[2-9]. In 1999 Liu et al showed that individual SWNT could be deposited from N,N-dimethylformamide (DMF) dispersions[7]. Shortly afterwards Ausman et al[2] demonstrated dispersion of SWNT in a number of solvents including N-methyl-2-pyrrolidone (NMP). The authors suggest that the criteria for a successful solvent were high electron pair donicity, low hydrogen bond donation parameter and high solvatochromic parameter. Bahr et al demonstrated meta-stable dispersion of SWNT in a

range of common solvents[3]. More recently Furtado et al[4] have shown that SWNT can be debundled to a significant degree in both DMF and NMP. Landi et al[6] followed this up with a quantitative study of SWNT dispersion in a range of amide solvents. In addition Maeda et al[8] showed that SWNT could be dispersed in mixtures of tetrahydrafuran with various amines.

4.3 Experimental Procedure

Purified single walled nanotubes (HiPCO) were purchased from Carbon Nanotechnologies Inc., and used as supplied (lot #PO289). Dispersions of pristine HiPCO nanotubes were prepared in N-methyl-2-pyrrolidone at a maximum nanotube concentration of 1 mg/ml. Initial dispersions were produced by sonicating for 2 minutes using a high power ultrasonic tip processor, model GEX600 (120W, 60kHz). In order to produce a dilution series this initial dispersion was then serially diluted to produce a range of dispersions with concentrations from 1 mg/ml to 0.001 mg/ml. After each dilution the dispersions were sonicated for 2 minutes by tip, followed by 4 hours in a low power ultrasonic bath (Ney Ultrasonik) and finally a 1 minute with the sonic tip. All dispersions were subsequently centrifuged at 6000 rpm (~4000g) for 90 minutes to remove any large aggregates. UV-vis-NIR absorption measurements were made before and after centrifugation using a Perkin Elmer Lambda 900 UV-vis-NIR spectrometer. For comparison purposes, HiPCO SWNT were also dispersed in an aqueous solution of sodium dodecyl benzenesulfonate (NaDDBS) (1 mg/ml HiPCO, 0.3 mg/ml NaDDBS) using an identical preparation procedure. This sample was characterised by UV-vis absorption spectroscopy and Atomic Force Microscopy (AFM).

It has been reported that sonication can damage SWNTs. In order to check for the presence of sonication induced damage, Raman spectroscopy measurements were made on the raw SWNT powder and both the sediment and supernatant recovered after centrifugation. Raman spectra, normalized to the intensity of the G line, at 1850cm^{-1}, were found to be almost totally identical for all three samples. No increase in the relative intensity of the D band was observed for either the sediment of the supernatant. As the D-band reflects the presence of amorphous or disordered carbon, this clearly shows that there was no observable damage to the SWNTs as a result of the sonication procedure.

Immediately after centrifugation a small volume from each dilution was deposited on a clean silicon substrate, under ambient conditions, and then dried at 60°C in a vacuum oven. Atomic Force Microscopy (AFM) studies were carried out in tapping mode using a

Multimode Nanoscope IIIA. POINTPROBE silicon cantilevers (typical tip radius $R_{Tip} \sim 10nm$) were used in all cases. Due to tip size effects all lateral measurements are significantly larger than the actual object size. Because of this effect all diameter measurements were made by measuring the height of the bundle above the surface. Transmission Electron Microscopy (TEM) measurements[*] were made with a Hitachi H-7000. High resolution TEM (HRTEM) was carried out using a FEI Tecnai F20. TEM grids were prepared by placing a drop of the amide dispersion on holey carbon grids (mesh size 400).

Near-infrared photoluminescence (PL) spectra of SWNT dispersions were measured[*] using a Bruker 66/S FTIR spectrometer equipped with a liquid nitrogen cooled germanium detector (sensitive in the range of ~850-1700 nm) and a monochromatised xenon lamp excitation source as described elsewhere[10]. PL spectra were typically recorded by scanning excitation wavelength in 3 nm steps between 550 and 900 nm and then combined into a map like that shown in figure 4.8. The PL intensity was corrected using the standard procedures both for the wavelength-dependent excitation intensity and instrumental response of the spectrometer and detector (in relative photon flux units). Concentration dependent measurements were carried out a number of times to ensure reproducibility. In all cases the PL intensity scaled the same way with concentration. For presentation purposes the concentration dependent PL intensity values were taken for the 1320 nm peak in the spectrum excited at 740 nm. Each set of concentration dependent measurements were normalised to the value for the highest concentration and then the intensity values at each concentration averaged to give a representative concentration dependent data set.

Raman spectra of spin-coated nanotubes on quartz substrates were acquired[*] with a Witec CMA200 confocal Raman microscope equipped with a 100x NA0.9 objective lens. The laser excitation wavelength, spectral resolution and typical excitation intensity were 633 nm, ~6 cm^{-1} and ~100 KW/cm^2, respectively. To locate deposited nanotubes, the substrate was scanned with a piezo table until a Raman signal was observed. The experimental procedure has been described in detail elsewhere[11].

---

[*] TEM & HRTEM measurements were carried out by Dr Valeria Nicolosi, *Sch. of Physics, TCD*
[*] PL measurements, for this chpt, were carried out by Sergei Lebedkin, *Universität Karlsruhe, Institut für Physikalische Chemie, 76128 Karlsruhe, Germany.*
[*] Raman measurements, for this chpt, were carried out by Sergei Lebedkin, *Universität Karlsruhe, Institut für Physikalische Chemie, 76128 Karlsruhe, Germany*

4.4 Results

Immediately after dilution and sonication it was observed that the higher concentration dispersions contained significant quantities of large nanotube aggregates with sizes of order of hundreds of microns. These aggregates did not appear in the lower concentration dispersions. In order to investigate these aggregates quantitatively, UV-vis-NIR spectra were measured for each dispersion. The dispersions were then mildly centrifuged at 6000 rpm for 90 minutes. After centrifugation it could clearly be seen that the aggregates had been removed. The supernatant was then carefully removed and UV-vis-NIR spectra re-measured. Spectra from both before and after centrifugation are shown in figure 4.1a and b. In both cases absorption peaks associated with transitions between symmetric van Hove peaks in the nanotube density of states can clearly be seen. The upper axis is plotted as the reduced transition energy, n, calculated from $E=2na_{cc}\gamma/D$ where E is the transition energy, a_{cc} is the C-C bond length (0.142 nm), γ is the C-C interaction energy (γ=3eV) and D is the nanotube diameter (taken as D=1nm)[6]. The value of this scheme lies in the fact that the transitions near n=1 are semiconductor 1-1 transitions, those near n=2 are semiconductor 2-2 transitions, while those near n=3 are metal 1-1 transitions[12].
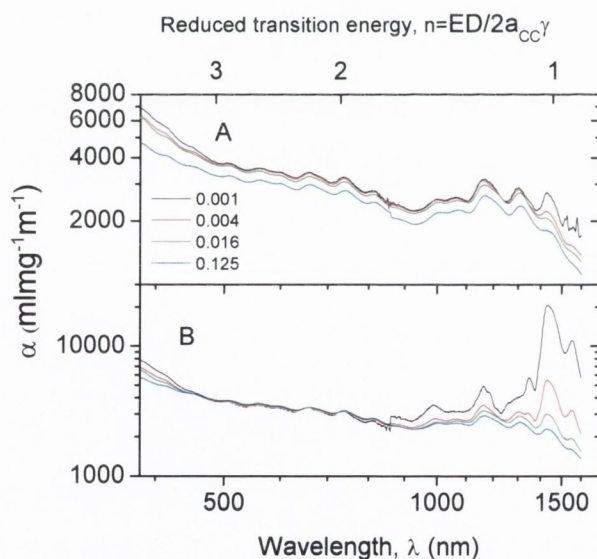
Figure 4.1

Absorption spectra of SWNT dispersed in NMP at a range of concentrations A) before and B) after centrifugation. The concentrations (mg/mL) for both parts are given in the upper panel. It should be pointed out that the increase in peak height after centrifugation between 1450-1550 nm is probably due to slight water contamination. The upper axis represents the reduced transition energy calculated using a nanotube diameter of D=1nm, a_{cc}=0.142 nm and γ=3eV.

The absorbance at 660 nm, A_{660} was measured for each sample and then divided by cell length, l, to give A_{660}/l. This data is shown in figure 4.2a. Before centrifugation, A_{660}/l scales approximately linearly with the initial concentration, C_I, over the whole concentration range, indicating that the aggregates at high concentration have a similar extinction co-efficient to the nanotubes dispersed at low concentration. We can use the Lambert Beer law to calculate the extinction co-efficient (λ=660nm) as the slope of this graph at low concentration, α_{660}=3264 mLmg^{-1}m^{-1} in reasonable agreement with Landi et al who measured values of between 3000 mLmg^{-1}m^{-1} and 3470 mLmg^{-1}m^{-1} at 700 nm for dispersions of SWNT in various amide solvents[6].

In order to further investigate the SWNT absorption coefficient, the data in figure 4.2a for the pre-centrifuged samples were divided by the initial nanotube concentration to give a plot of α_{660} before centrifugation as a function of initial concentration as shown in figure 4.2b. This graph clearly reveals variations in α_{660} as a function of concentration. At high concentrations α_{660} is low, probably because the dispersions are not optically dilute in this range. At C_I=0.1 mg/mL, α_{660}~3250 mLmg^{-1}m^{-1} and increases gradually, approaching 3500 mLmg^{-1}m^{-1} as C_I approaches 0.001 mg/mL. As shall be described below, this represents the range over which debundling is observed. It is possible that this slight increase in absorption coefficient at low concentration is associated with the increased presence of small bundles and individual nanotubes as opposed to larger bundles at higher concentrations. It should be noted that the increase in absorption coefficient is quite small reflecting the small dependence of the absorption coefficient on SWNT concentration.

After centrifugation the A_{660}/l values are significantly lower at high concentration compared to the pre-centrifugation measurements. This is due to the fact that the aggregates have been removed by centrifugation. We can use this information in conjunction with α_{660} to calculate the new concentration after centrifugation, C_F. This concentration is the true nanotube concentration after centrifugation and shall be used exclusively from this point and referred to as C_{NT}. In addition we can calculate the mass fraction of aggregates, χ_{Agg} from

$$\chi_{Agg} = \frac{A_{660,I} - A_{660,F}}{A_{660,I}} \tag{4.1}$$

Where $A_{660,I}$ and $A_{660,F}$ are the absorbance at λ=660nm before and after centrifugation respectively. This quantity is plotted in figure 4.2c as a function of the initial SWNT concentration. This plot clearly shows that aggregates dominate the dispersion at concentration above C_I=0.02 mg/ml. This concentration can be thought of as the dispersion

limit for SWNT in NMP. This compares well with the dispersion limits for SWNT in amide solvents quoted by Landi et al[6]. The observed values were between 1.6×10^{-3} and 6.3×10^{-3} mg/ml for dimethylformamide (DMF) and N,N-dimethylacetamide (DMA) respectively.
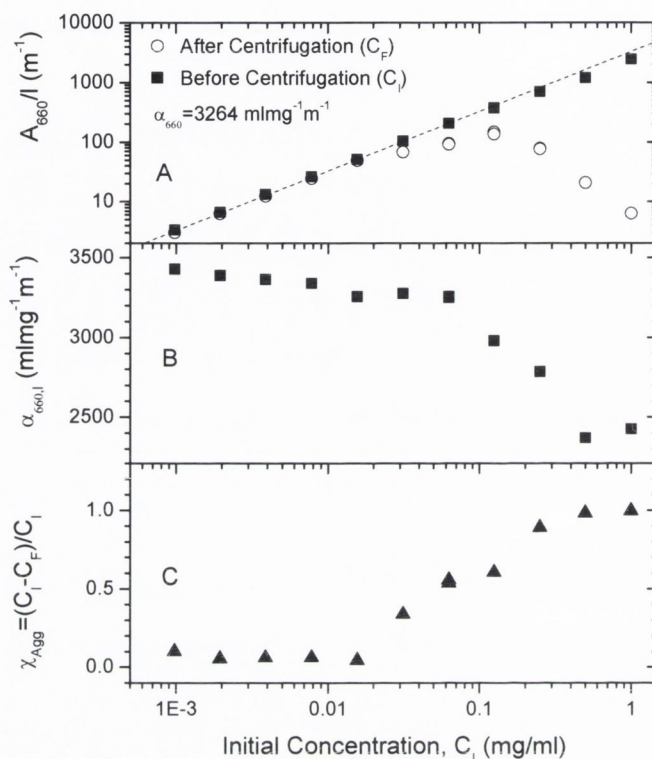
Figure 4.2

A) Absorbance per unit length measured at λ=660 nm, A_{660}/l, before and after centrifugation as a function of initial nanotube concentration. B) Absorption coefficient at λ=660 nm before centrifugation found by dividing A_{660}/l by the initial nanotube concentration, C_I. It should be noted that the y-axis is linear, as the dependence of the absorption coefficient with SWNT concentration is found to be minimal. C) Fraction of the nanotube mass contained in large aggregates as a function of initial concentration.

While it is well known that SWNTs can be dispersed in NMP, it is less clear how stable these dispersions are over time. To investigate this we performed sedimentation measurements on a dispersion of SWNTs at C_{NT} =0.015 mg/ml after centrifugation. This experiment involves the measurement of the samples absorbance (650nm) as a function of time in a custom built apparatus[13, 14], in this case over the course of 17 days as shown in figure 4.3a. The absorbance remains extremely stable over this timescale indicating that no sedimentation occurs. However, lack of sedimentation does not necessarily mean stability.

It is important to verify that no nanotube aggregation occurs over this timescale. To do this we removed a drop of the dispersion for AFM analysis immediately after centrifugation and another drop after 11 days. AFM measurements show the presence of large quantities of one-dimensional objects. In general these objects were of order of a few nanometers high and up to one micron long. As HiPCO single-walled nanotubes have a diameter of 0.8-1.3 nm, the objects observed are bundles of individual tubes. The diameters of a large quantity of these bundles were ascertained by measuring their heights above the substrate. These diameters were plotted as distributions in figure 4.3b and c and have means of 2.8 nm and 2.6 nm for the sample collected immediately and that collected after 11 days of sedimentation respectively. Statistical analysis shows that these distributions are indistinguishable within a 99.99% confidence interval. This clearly shows that not only has no sedimentation occurred but the bundles have not re-aggregated over the time scale of weeks. This suggests that the dispersion is at least quasi-stable and may in fact be at or near equilibrium.
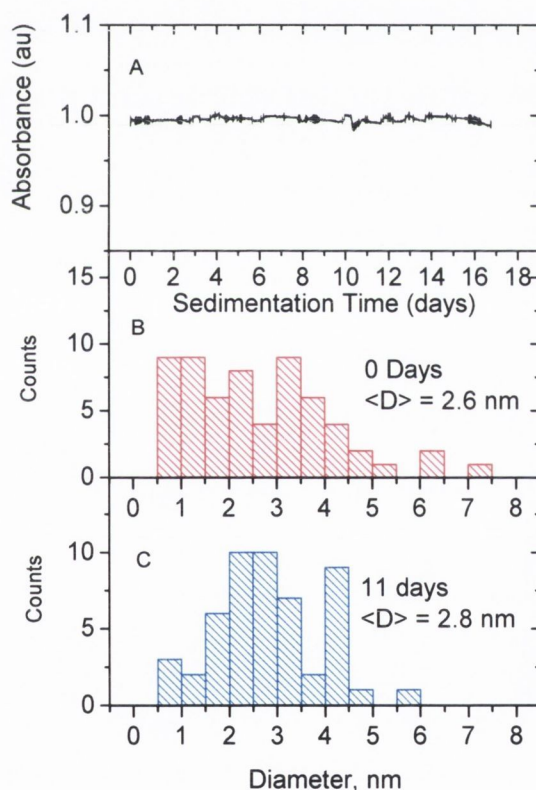
Figure 4.3

A) Sedimentation curve for C_{NT} =0.015 mg/ml after centrifugation showing stability against sedimentation. B) and C) show bundle diameter distributions for the same sample after 0 and 11 days respectively.

To study the concentration dependence of the bundle size distribution, AFM measurements were also made for a set of dispersions over the entire range of concentrations. In all images large numbers of bundles were observed. Shown in figure 4.4 are representative images for nanotubes at concentrations of 0.016 and 0.001 mg/ml.
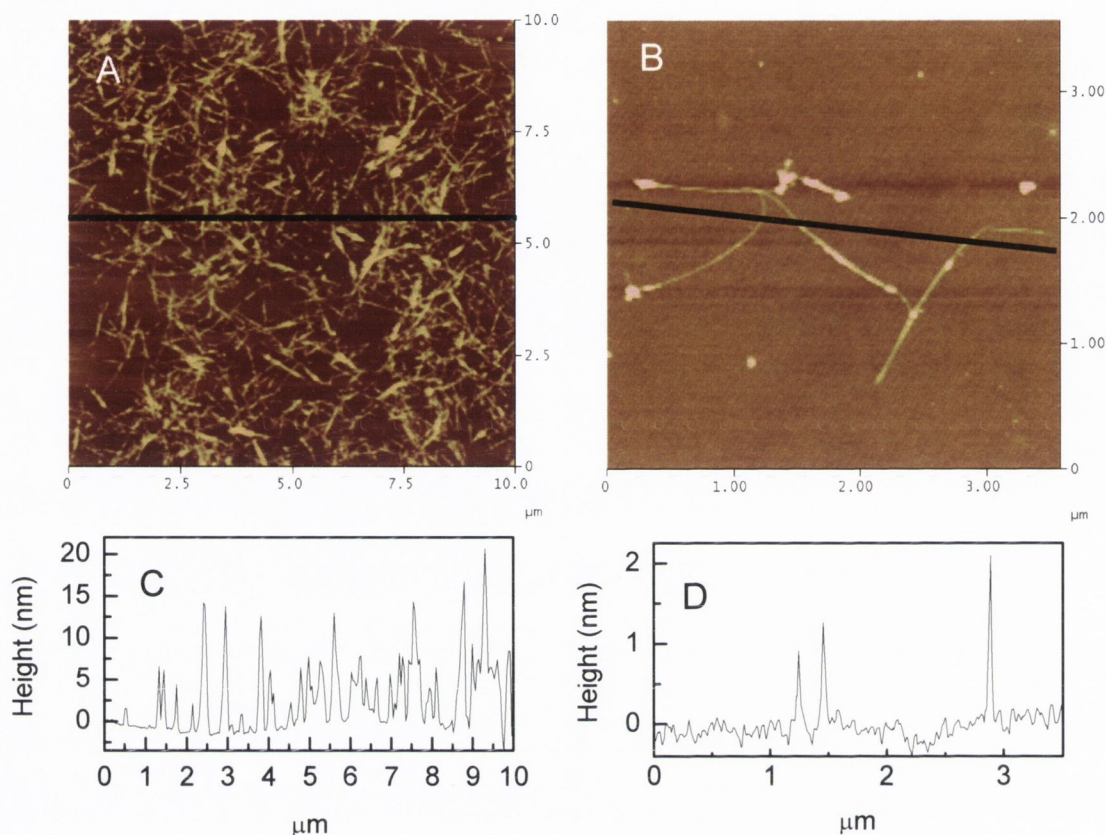
Figure 4.4

Typical AFM images for SWNT at a concentration of A) 0.016 mg/ml and B) 0.001 mg/ml. Line sections appropriate to figures A) and B) are shown in C) and D) respectively. Note that the objects in D) are much smaller than the objects in C).

In order to investigate the size distribution of the bundles, diameter measurements were made for all bundles observed in the AFM images. These were then plotted as diameter distributions for each concentration. The diameter distributions are shown in figure 4.5. The bundle length could be measured by TEM for the C_{NT}=0.024 mg/mL sample giving a value of L_{NT}=900±270 nm.

From figure 4.5 it can clearly be seen that the bundle diameters shift to lower values as the concentration is decreased. In fact at the lowest concentration studied (10^{-3}

58

mg/ml), almost 75% of bundles had diameters of less than 2 nm. In addition it can be seen that a significant population of small bundles with D<2nm exists at *all* concentrations.
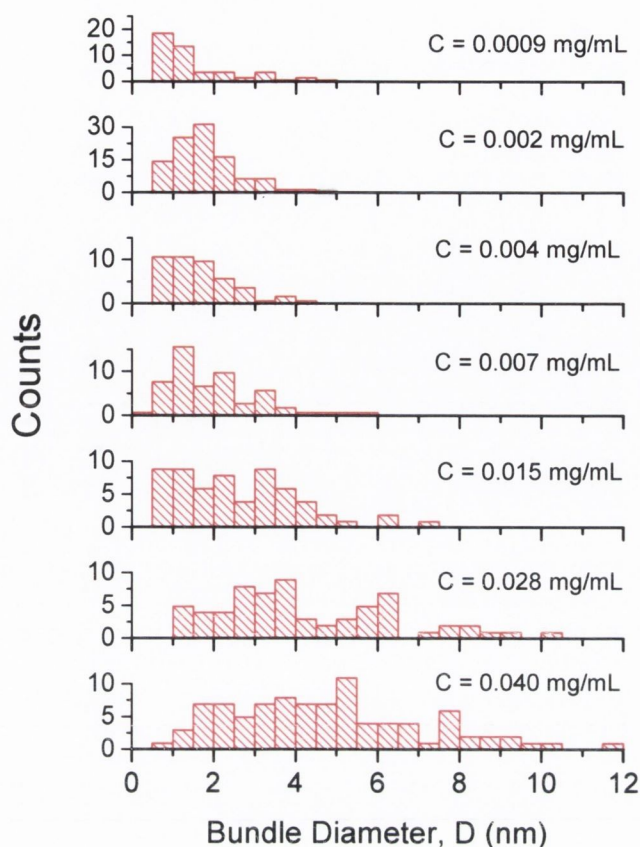
Figure 4.5

Histograms of bundle diameters for SWNTs dispersed in NMP at a range of concentrations from 0.04 mg/mL to 0.001 mg/mL. Diameters were measured from AFM images of material deposited from the dispersion immediately after sonication. Decreases in concentration are accompanied by a down-shift of the diameter distribution. Note that a population of single, isolated nanotubes is present at all concentrations.

The root mean square bundle diameter, $D_{rms}=\sqrt{<D^2>}$, as a function of concentration is shown in figure 4.6. For completeness the top axis also shows the concentration transformed into nanotube volume fraction, V_f^{NT}, using $V_f^{NT}=C_{NT}/\rho_{NT}$ where ρ_{NT} is the nanotube density (~1500 kg/m^3)[15]. The root mean square diameters tend to fall monotonically from approximately 6 nm at high concentration, to less than 2 nm at C_{NT} = 0.008 mg/ml, before saturating at this level. This sort of debundling phenomena has been previously observed for SWNT-polymer dispersions[16] and for inorganic nanowire dispersions[13].
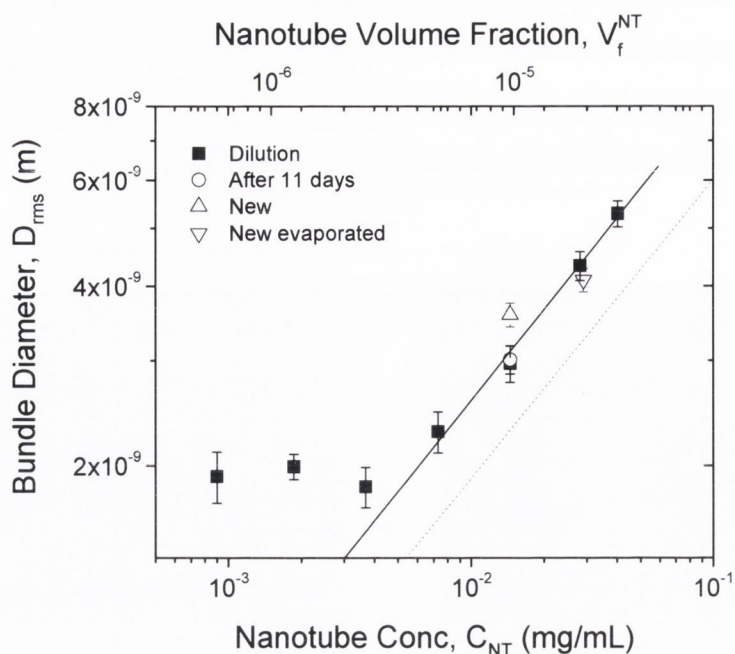
Figure 4.6

Diameter of nanotube bundles as a function of concentration as obtained from the diameter distributions (labeled "Dilution"). This is plotted as the root mean square diameter in order to facilitate analysis using 4.4. The error bars are calculated from the standard error of the distribution. The root mean square bundle diameter decreases with decreasing concentration before saturating at approximately 1.9 nm. The solid line comes from fitting equations 4.4 and 4.5. The dotted line is calculated from equation 4.5 assuming that each bundle occupies exactly its own spherical volume with L_{Bun}=900nm. The open circle shows the diameter measured after 11 days. The up triangle labeled "New" represents the dispersion made up directly at 0.015 mg/ml while the down triangle labeled "New evaporated" represents the diameter of this sample after evaporation.

This apparent dependence of bundle diameter on concentration has a number of possible explanations. One possibility is the formation of an anisotropic nanotube phase in solution due to concentration dependent steric effects. This could result in concentration dependent aggregation of the aligned nanotubes. Both Onsager and Flory calculated that such an anisotropic phase is stable only above a minimum volume fraction V_f^{MIN} which depends on the aspect ratio, x[17]:

$$V_f^{MIN}(x) = \frac{8}{x}\left(1 - \frac{2}{x}\right) \qquad (4.2)$$

60

At the highest concentration studied (C_{NT}=0.04 mg/ml, V_f^{NT} ~2.67×10^{-5}) the average bundle dimensions (quoted above) result in aspect ratios of 170 and hence values of V_f^{MIN} of 0.05. This value of V_f^{MIN} is far above the concentration range studied which means that all our nanotube dispersions are expected to be isotropic. Thus steric effects are unlikely to be responsible.

Another possibility is due to the fact that during the serial dilution, the dispersions underwent successively longer sonication with each sequential dilution. It is possible that this could result in debundling due to increased sonication and not due to reduced concentration. To test this we made up a dispersion directly at 0.015 mg/mL. This dispersion received significantly less sonication than the original 0.015 mg/mL sample prepared by dilution. The root-mean-square bundle diameter from this sample is shown on figure 4.6. This datum is close to the previous measurement (within error) showing that different sonication times do not lead to significantly different levels of debundling.

To confirm that the bundle diameter is actually controlled by concentration, we allowed the solvent to evaporate from the new 0.015 mg/mL sample resulting in an increase in concentration. Measurements of the bundle diameter distribution were made after enough NMP had evaporated to give a dispersion concentration of 0.03 mg/mL. The bundle diameters distributions were measured and the D_{rms} plotted on figure 4.6. The bundle diameters measured during this evaporation experiment are identical to those measured for equivalent concentrations during the dilution experiment. This strongly suggests that the bundle diameter distribution evolves to an equilibrium value which is controlled by nanotube concentration.

We can model the concentration dependence of the debundling process very crudely by noting that the input of sonic energy tends to drive the system toward debundling. However as debundling occurs the dispersion becomes dominated by large quantities of small bundles. This increases the probability of aggregation. This suggests that a quasi-equilibrium will be reached. We suggest that this equilibrium state is characterized by an equilibrium number density of bundles. This is equivalent to an equilibrium volume of solvent per bundle. In this case we can easily write this equilibrium number density $(N/V)_{Eq}$ in terms of the equilibrium (average) bundle volume $\langle V_{bun} \rangle$:

$$\left(\frac{N}{V} \right)_{Eq} = \frac{C_{NT}}{\rho_{NT} \langle V_{bun} \rangle} \tag{4.3}$$

where C_{NT} is the mass concentration of nanotubes and ρ_{NT} is the nanotube density. We should note that while we don't know how the average bundle volume scales with

concentration we have measured how the bundle diameter scales with concentration. If we approximate the bundle length (L_{bun}) as constant we can rearrange to get:

$$D_{rms} = \sqrt{\langle D^2 \rangle} \approx \left[\frac{4C_{NT}}{\rho_{NT} \pi L_{bun} (N/V)_{Eq}} \right]^{1/2} \qquad (4.4)$$

This expression has been fitted to the data in figure 4.6 (solid line) and represents a very good fit. Taking $\rho_{NT} = 1500$ kg/m^3 and using the value for nanotube length obtained from TEM, we can calculate the equilibrium bundle number density. This was calculated to be $(N/V)_{Eq} = (1.5 \pm 0.6) \times 10^{18}$ m^{-3}. Taking the inverse of this quantity gives the equilibrium solvent volume per bundle, V_{Sol}^{Eq}. This volume can be considered similar to the pervaded volume concept used in polymer physics[18]. This can be calculated at $V_{Sol}^{Eq} = (6.7 \pm 2.7) \times 10^{-19}$ m^3. Interestingly, this volume is close to the volume of a sphere whose diameter is defined by the average bundle length (900 nm). The volume of this sphere is $V_{Sphere} = (3.8 \pm 3.4) \times 10^{-19}$ m^3. If we consider V_{Sphere} as the volume of solvent occupied by the nanotube then, in this case, each bundle on average almost exactly occupies its own pervaded volume. In polymer physics terminology this occurs at the overlap concentration. Interestingly nanotubes dispersed in NMP appear to adjust their bundle size distribution with concentration to always be close to the overlap concentration.

Each bundle occupies exactly its own pervaded volume when $V_{Sol}^{Eq} = V_{Sphere}$. We can easily show that if this is the case then

$$D_{rms} = L_{Bun} \sqrt{\frac{2}{3} \frac{C_{NT}}{\rho_{NT}}} = L_{Bun} \sqrt{\frac{2}{3} V_f} \qquad (4.5)$$

Taking $L_{Bun} = 900$nm and with $\rho_{NT} = 1500$ kg/m^3 we can plot D_{rms} in this scenario as the dotted line in figure 4.6. This curve matches qualitatively to the experimental data for D_{rms}. The fact that the bundles have slightly larger diameters than predicted by this model suggest that in reality $V_{Sol}^{Eq} > V_{Sphere}$. Alternatively we can assume that the bundles exactly occupy their own pervaded volume and fit equation 4.5 to the data in figure 4.6 (solid line). We can then calculate L_{Bun} from the fit. This works out to be $L_{Bun} = 1275 \pm 250$ nm, slightly larger than that measured by TEM. It is not clear which of these scenarios is closer to reality.

In polymer physics, concentrations below the overlap concentration are considered dilute and inter-chain interactions can be neglected. The fact that $V_{Sol}^{Eq} > V_{Sphere}$ then suggests that the dispersions are balanced slightly below the dilute / non-dilute interface (using the value for L_{Bun} as measured by TEM). In this situation aggregation may be limited by random collisions between bundles. If each bundle is the sole occupier of its

own spherical volume, then collisions cannot occur due to random rotations (tumbling) of adjacent bundles. Collisions are then rare as they can only occur due to translational diffusion, which for nanotubes is a slow process.

This clearly suggests that the bundle size is related to the equilibrium number density. In turn this means that bundle dimensions can be related to nanotube concentration simply by considering the volume of the sphere traced out by the tips of the bundle as it tumbles through the solution. This is potentially an important tool for planning concentrations in dispersions of one-dimensional nanostructured materials.

It is known that the individual HiPCO SWNTs have diameters in the range 0.7–1.3 nm. This suggests that any object observed with height of ≤ 1.4 nm is probably an individual nanotube although it may be a small bundle of 2 or 3 nanotubes lying flat. We can calculate, from the diameter distributions, the ratio of individual tubes to the total number of objects, N_{Ind}/N_T. This quantity is shown in figure 4.7a and increases as concentration decreases, approaching 70% at $C_{NT}=0.004$ mg/ml. This shows that 70% of the objects at low concentration are individual nanotubes. This compares to measurements by Furtado et al on dispersions of acid treated nanotubes in DMF and NMP that 50-90% of objects are individual nanotubes[4]. We can use this information to calculate the absolute number of individual nanotubes per unit volume of solvent by noting:

$$\frac{N_{Ind}}{V} = \frac{N_{Ind}}{N_T} \frac{N_T}{V} \approx \frac{N_{Ind}}{N_T} \frac{4C_{NT}}{\rho_{NT} \cdot \pi \langle D^2 \rangle L_{bun}} \tag{4.6}$$

where all symbols have the same meaning as before. The number density has been calculated and is shown in figure 4.7b. For HiPCO SWNT dispersed in NMP the number density of individual nanotubes peaks around $C_{NT}=0.01$ mg/ml. This shows unambiguously that even as the concentration decreases the number of individual nanotubes can increase if the debundling process is efficient enough. Also shown as the dashed line in figure 4.7b are values of $(N/V)_{Eq}$ calculated earlier. It is clear that the maximum number of individual tubes per volume approaches the equilibrium bundle number density. This shows that $(N/V)_{Eq}$ can be thought of as a maximum bundle number density.

In addition we can estimate the mass fraction of individual nanotubes from the diameter distributions. Assuming the densities of bundle and individual nanotubes are equal and approximating the bundle length as similar to the individual tube length, we can write:

$$\frac{M_{Ind}}{M_T} = \frac{\sum\limits_{D<1.4nm} D^2 L_{Ind}}{\sum D^2 L_{bun}} \approx \frac{\sum\limits_{D<1.4nm} D^2}{\sum D^2} \tag{4.7}$$

This quantity has been calculated and is presented in figure 4.7c. The mass fraction of individual tubes increases with decreasing concentration, saturating at approximately 20%. This saturation value is of course less than that for the number density of individual tubes (figure 4.7b) as much of the mass is concentrated in the larger bundles.

We can use this data to calculate the mass of individual nanotubes per unit volume of solvent, M_{Ind}/V. This can be thought of as a partial concentration of individual nanotubes. We can calculate this using the fact that:

$$\frac{M_{Ind}}{V} = \frac{M_{Ind}}{M_T}\frac{M_T}{V} = \frac{M_{Ind}}{M_T}C_{NT} \qquad (4.8)$$

This quantity has been calculated and is presented in figure 4.7d. This data is very similar to that presented in figure 4.7b, increasing as concentration decreases to a maximum of $(M_{Ind}/V)\sim 8\times 10^{-4}$ mg/ml at total concentrations of $C_{NT} \sim 8\times 10^{-3}$ mg/ml. Interestingly enough both N_{Ind}/V and M_{Ind}/V display maxima around 8×10^{-3} mg/ml. These concentrations represent the conditions under which the total number of individual tubes is maximized. This is an unexpected result. One might naively assume that the number density of individual tubes might be maximized at high concentration or at a low concentration where all the objects are individual tubes. However the fact that the number of individual tubes is maximized at a midrange concentration where the individual tubes co-exist with a population of bundles is extremely interesting.

The ratio of M_{Ind}/V to N_{Ind}/V is just the average mass per nanotube. As these two quantities, as presented in figure 4.7b and d, are calculated in different manners we can use their ratio to calculate the average nanotube mass. This is plotted as a function of concentration in figure 4.7e as the nanotube molar mass. This value is invariant with concentration as would be expected. The average of these values is 6.8×10^5 g/mol. If we assume a mean SWNT diameter of 1nm and a density of 1500 kg/m^3, we can use this data to estimate the average nanotube length to be 960 nm in good agreement with the TEM measurements. This suggests that the bundle size distribution arranges itself such that the system exists slightly below the dilute/semi-dilute boundary as discussed above.
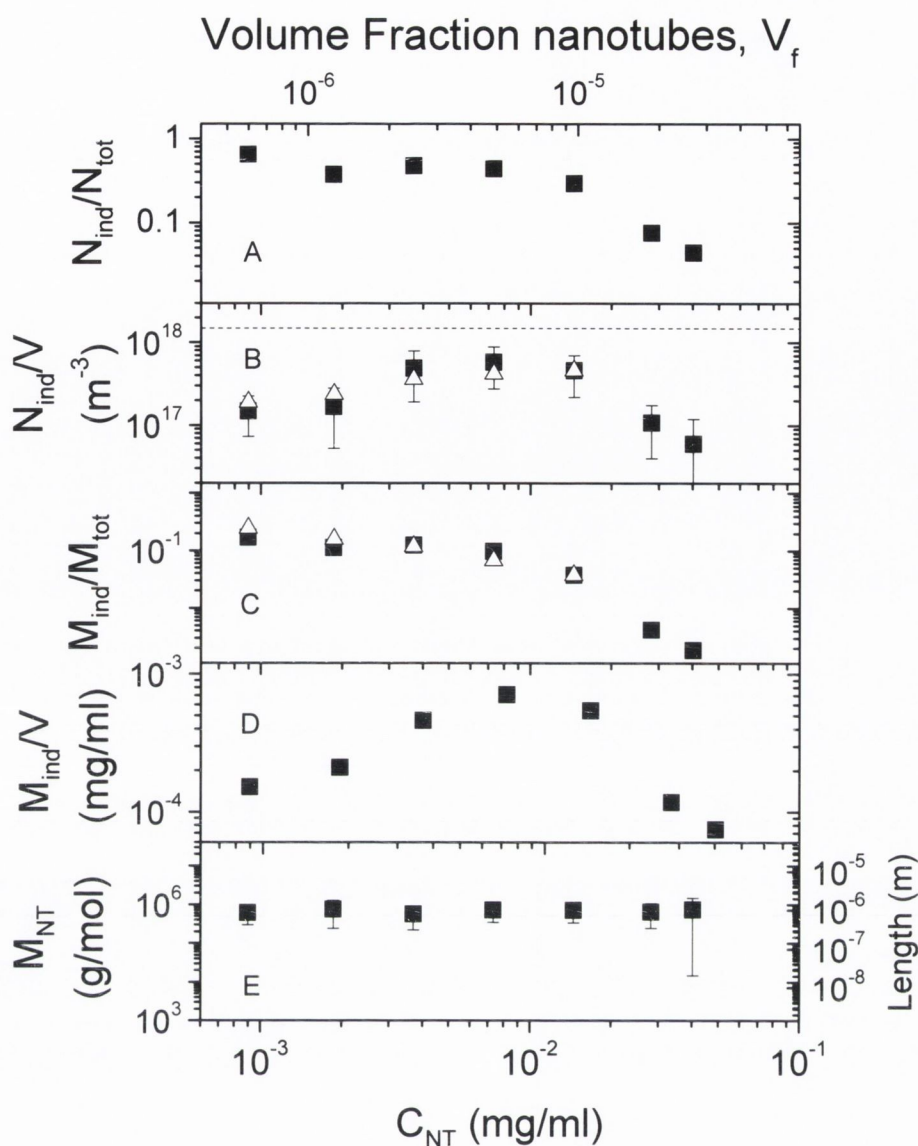
Figure 4.7

A) Number fraction of individual nanotubes as a function of concentration as obtained from the diameter distributions. B) Number of individual nanotubes per unit volume. C) Mass fraction of individual nanotubes. D) Partial concentration of individual nanotubes. E) Molar mass of individual nanotubes as calculated from the data presented in B) and D). The data represented by open triangles in B) and C) are derived from photoluminescence data.

We have been able to derive much information about the system from AFM studies of deposited bundles. However, the possibility still remains that the concentration dependence of the bundle size distributions is actually dominated by drying effects. In fact, theoretical studies have shown that concentration dependent bundling effects can actually

occur for one-dimensional objects that are mobile during drying[19]. In order to rule this possibility out we need an in-situ measurement technique that gives information about either the bundle size distribution or alternatively the population of individual nanotubes. Such a technique is infra-red photoluminescence which is sensitive only to individual nanotubes.

Near infra-red photoluminescence (PL) measurements were made on a number of concentrations of SWNT in NMP. Shown in figure 4.8a is a typical photoluminescence map measured for one of our dispersions. The PL provides additional strong evidence for the presence of a significant fraction of individual nanotubes in NMP dispersions, since the PL is almost completely quenched in large bundles of SWNTs[20]. Compared to water-surfactant dispersions of HiPco nanotubes (figure 4.8b), PL peaks are significantly red-shifted in NMP. This likely reflects a specific interaction of nanotubes with NMP molecules. The PL shifts correspond to the shifts of electronic transition energies E_{11} and E_{22} of $-(20\text{-}32)$ meV and $-(22\text{-}43)$ meV, respectively.
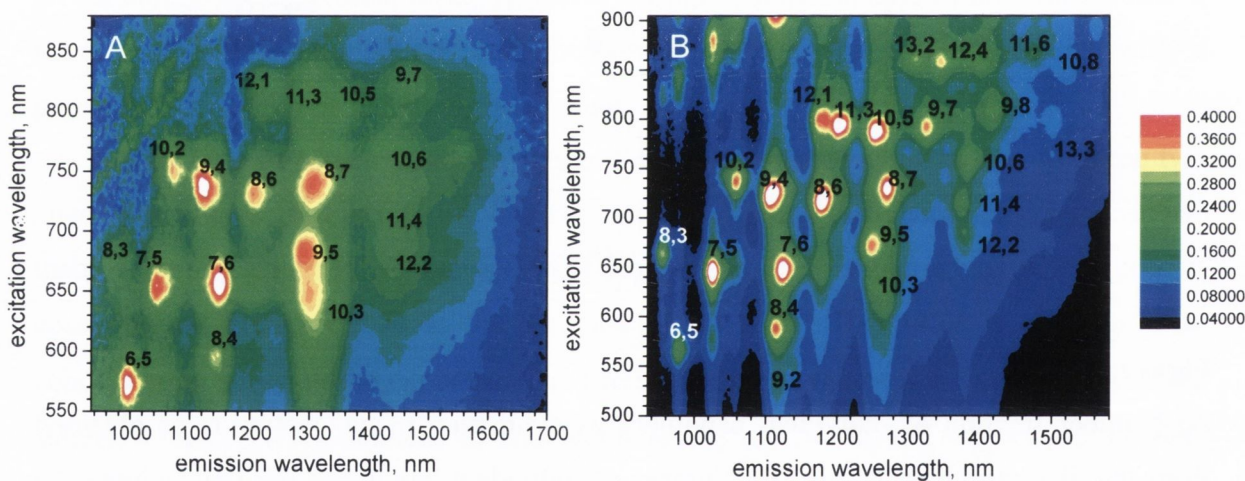
Figure 4.8

A) Photoluminescence map (emission intensity versus excitation anemission wavelengths) of HiPco nanotubes dispersed in NMP at concentration of 0.006 mg/mL. B) PL map of Hipco SWNT in SDBS/D_2O dispersion.

The number of distinct PL peaks assigned to different (n,m) nanotube species in figure 4.8 is too small to draw statistically firm conclusions as to whether the PL shifts depend on the structure (helicity) of nanotubes and in what manner. However, there seems to be a clear trend for larger red-shifts at increasing nanotube diameter (compare, for

instance, (9,7) and (10,6) tubes (d = 1.10 and 1,11 nm, respectively) with (6,5) and (7,5) tubes (d = 0.75 and 0.83 nm, respectively) in figure 4.8B). The origin of this diameter (nanotube curvature) effect is not clear at the moment.

PL emission spectra (excited at 740 nm) are shown in figure 4.9 as a function of nanotube concentration. At each concentration the spectral shape is the same, indicating no changes in populations of individual nanotube types as the overall concentration is changed. However the PL intensity falls smoothly with concentration. The PL intensity of a given peak, I_{PL}, is proportional to the total number of individual nanotubes involved in that specific optical transition. As the spectral shape is unchanged with concentration, the intensity of the peak at 1320 nm, for example, is proportional to the total number of individual nanotubes in the sample and hence $I_{PL} \propto N_{Ind}/V$.
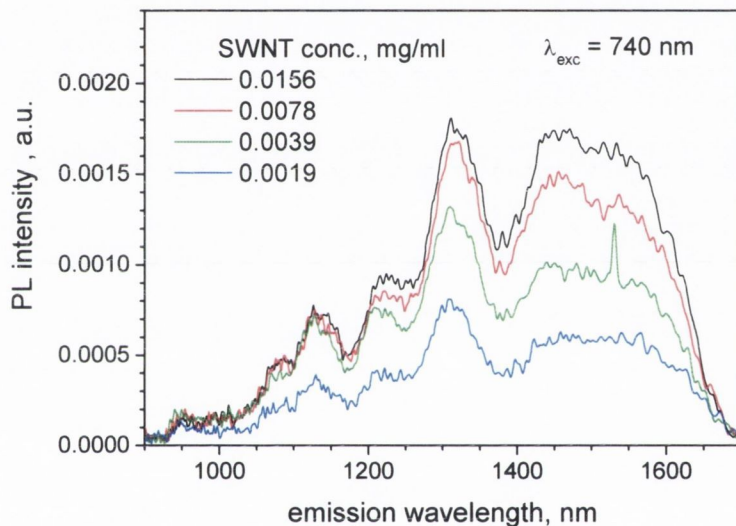
Figure 4.9

Typical concentration dependence of PL emission spectra for Hipco SWNT in NMP excited at 740 nm.

The intensity of this peak has been plotted as a function of concentration in figure 4.7b and normalised to the AFM datum at C_{NT}=0.015 mg/ml. Its concentration dependence matches the AFM data for N_{Ind}/V almost perfectly. In addition, the PL intensity can be normalised to concentration and expressed as I_{PL}/C_{NT}. It can be easily shown that this quantity is proportional to the mass fraction of individual nanotubes: $I_{PL}/C_{NT} \propto M_{Ind}/M_T$. The concentration normalised PL intensity has been plotted on fig 3.7c. Again its concentration dependence matches very well to the AFM data for M_{Ind}/M_T. This shows categorically that the statistical data for populations of individual nanotubes as a

function of concentration applies to the nanotubes in solution and not just after drying. This confirms that the concentration dependence of the bundle size distributions in-situ is a real effect.

Note that the AFM measurements have been performed on freshly prepared NMP dispersions whereas the PL measurements have been delayed by one-two weeks. A further ultrasonic treatment was found to improve the PL intensity only ~twofold at best, independent on the SWNT concentration. This suggests that the fraction of individually dispersed nanotubes is relatively stable within weeks at least in agreement with the AFM and sedimentation measurements.

The PL of nanotubes dispersed in NMP, even at very low concentrations <0.005 mg/ml is, by a factor of ~50-100, weaker compared to the water-surfactant dispersions of similar optical density at the excitation wavelength. According to the AFM, absorption as well as the above PL data, this difference cannot be explained by a smaller fraction of individual (luminescent) nanotubes in NMP. (For well-prepared water-surfactant dispersions this fraction is assumed to be over 50%[20]) Therefore we believe that the main reason for the weak PL is an intrinsically low PL efficiency for nanotubes when dispersed in NMP or similar aromatic amine solvent due to solvent-nanotube interactions.

Finally, micro-Raman measurements of HiPCo nanotubes deposited on quartz substrates by spin-coating of NMP dispersions were carried out. These also show a significant fraction of individual nanotubes in the low-concentrated dispersions. Figure 4.10 gives examples of Raman spectra recorded for substrate-deposited nanotubes. The spectra (a) and (b) show narrow, one-peak radial breathing mode (RBM) patterns which are consistent with individual nanotubes or at least small bundles with only one resonant tube type[21]. Nanotube like objects showing two or more RBM features (similar to spectrum (c) in figure 4.10) were also frequently found and assigned to small bundles of only a few nanotubes.
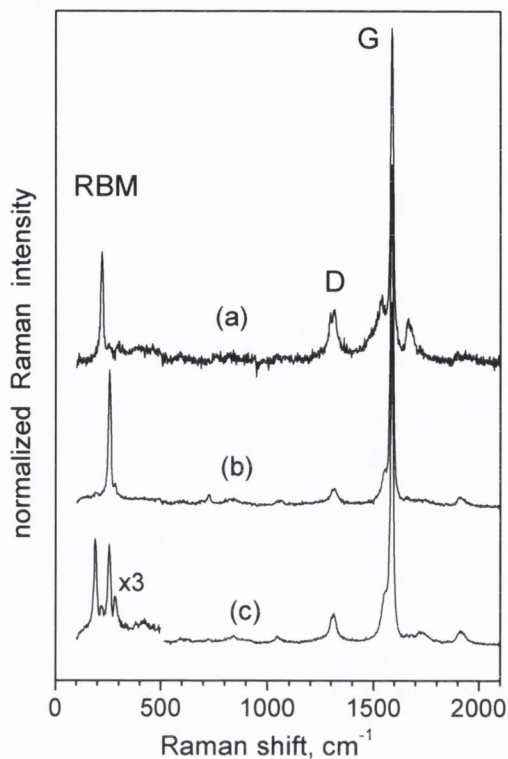
Figure 4.10

Raman spectra of nanotubes deposited from a NMP dispersion (C = 0.008 mg/mL) on a quartz substrate: (a, b) individual nanotubes assigned to (12,3) and (11,1) structures, respectively, and (c) a small nanotube bundle. Laser excitation wavelength is 633 nm. Indicated are two characteristic regions corresponding to the radial breathing (RBM) and tangential *G*-mode vibrations.

4.5 Discussion

It seems clear both from the work presented here and from the literature in general that nitrogen containing solvents such as NMP are good dispersants for carbon nanotubes. However, this poses the question which properties of these solvents are required for dispersion to occur? Firstly, it should be pointed out that, despite the casual use of the word "solution" in the literature, no direct evidence has ever been presented to show that carbon nanotubes are thermodynamically soluble in any binary system. However, whether or not the systems we are dealing with are solutions or dispersions, their properties will depend strongly on the magnitude (and sign) of the enthalpy of mixing. This parameter is a measure of the relevant strengths of solute-solute interactions versus solvent-solvent interactions versus solvent-solute interactions[18]. In colloidal dispersions the enthalpy of

mixing tends to be positive, reflecting attractive, short range inter-colloid interactions. In true solutions the enthalpy of mixing tends to be slightly positive or even negative reflecting a more favourable solute-solvent interaction. In the case of macromolecular solutions the enthalpy of mixing, ΔH_{Mix}, is given by[17]

$$\Delta H_{Mix} = z\Delta E n_1 \phi_2 \qquad (4.9)$$

where z is the coordination number, n_1 is the number of moles of solvent and ϕ_2 is the macromolecule volume fraction. The parameter ΔE is given by

$$\Delta E = -\left(E_{11} + E_{22} - 2E_{12}\right) \qquad (4.10)$$

where E_{11} is the solvent-solvent interaction energy, E_{22} is the solute-solute interaction energy and E_{12} is the solute-solvent interaction energy. This means that the more negative E_{12} becomes the smaller ΔE and hence ΔH_{Mix} become. Furthermore, if $|E_{12}|>(|E_{11}|+|E_{22}|)/2$ then ΔH_{Mix} actually becomes negative. This in order to successfully disperse carbon nanotubes in any solvent the solvent-nanotube interaction must be as strong as possible.

It has been pointed out by Ausman et al[2] and subsequently by Landi et al[6] and Furtado et al[4] that all successful nanotube dispersing solvents are characterised by high electron pair donicity. This suggests that the presence of electron lone pairs, as for solvents such as NMP, dimethylformamide (DMF), results in weak solvent-nanotube charge transfer. This would certainly be expected to result in strong solvent nanotube binding. However, this condition alone is insufficient as dimethylesulphoxide (DMSO), a poor solvent for nanotubes, contains three lone pairs. Furtado[4] suggests that the dominant interaction is the adsorption of solvent molecules on the nanotube surface stabilised by the donation of π electrons from the nanotube to the solvent. Again this should result in strong solvent nanotube binding.

In addition Landi[6] has pointed out that the presence of alkyl groups attached to the carbonyl of amide solvents tends to stabilise the double bond character in the resonance stabilised amide thus stabilising the solvent molecules dipole moment. This, they suggest, results in a stronger solvent-nanotube interaction as evidenced by higher observed dispersability of SWNT in N,N-dimethylpropanamide (DMP) compared to DMF[6]. This suggests that the interaction may depend strongly on the dipole moment of the molecule. However, it should be pointed out that other highly polar molecules such as DMSO[2] and acetonitrile[6] do not disperse SWNT. Landi[6] also suggest that π stacking of the solvent molecules on the sidewall of the nanotube may play a role in the solvent-nanotube interaction. They suggest that this interaction is optimised when solvent bond lengths and angles match the hexagonal structure of graphite. This however seems unlikely as the

symmetry breaking due to the wall curvature precludes perfect lattice matching for molecules adsorbed at the van der Waals distance from the nanotube sidewall[22].

It should not be forgotten that the concept of a perfectly hexagonal nanotube sidewall is an abstraction. All nanotubes contain defects even if the numbers are low. In addition purification of nanotubes by methods such as acid oxidation generally results in the covalent attachment of moieties such as carboxylic acid. Even after vacuum annealing one cannot be totally sure that the nanotubes contain only carbon. Thus we cannot rule out the possibility that solvents interact preferentially with defects or possibly with polar functionalities and not with the hexagonal graphitic lattice.

Finally we must recognise that non-enthalpic factors can strongly effect nanotube dispersion. Consider a situation where strong solvent-nanotube interactions result in the solvent stacking on the nanotube sidewall in a partially ordered fashion. If the interfacial layers of solvent are ordered compared to the bulk solvent this will result in a reduction in solvent configurational entropy on mixing[23], ΔS_O, where

$$\Delta S_O = \Delta S_{O,A} A \tag{4.11}$$

where $\Delta S_{O,A}$ is the reduction in entropy per unit area and A is the nanotube-solvent interfacial area. This reduction in entropy is equivalent to an enthalpic cost of

$$\Delta H_O = -T \Delta S_{O,A} A > 0 \tag{4.12}$$

which increases as the interfacial area, A, increases. This means that it costs more and more energy to create the interface as debundling proceeds. This energy cost is over and above that associated with the enthalpy of mixing. It has been shown that this effect can partly account for the insolubility of nanotubes in toluene[23]. This suggests that successful solvents do not actually π-stack on the nanotube sidewall as suggested by Landi.

Thus, it appears that the required characteristics for solvents to act as nanotube dispersants are large solvent-nanotube interaction energies relative to solvent-solvent and nanotube-nanotube interactions and the absence of ordering at the nanotube solvent nanotube interface. While most of the solvents described in the literature appear to display high lone pair donacity we cannot assume that this is indeed a prerequisite. We cannot rule out the possibility of existence of strongly interacting but disordered solvents that do not display high lone pair donacity.

While the high lone pair donacity of NMP probably plays a role in the solvent nanotube interaction, we can be certain that the total solvent-nanotube interaction has other contributions from London and dipole induced dipole interactions for example. In any case, it is certain that the total solvent nanotube interaction energy must be high, resulting

in a small (positive) or even negative enthalpy of mixing. In addition, as we know that NMP is a good dispersant, we can infer that there is no prohibitive configurational entropy penalty associated with the solvent-nanotube interface. This suggests that the interaction with the nanotube does not induce significant solvent ordering in the case of NMP.

4.6 Conclusions

In conclusion, using NMP we can routinely fabricate good quality SWNT dispersions without the need for ultracentrifugation. While at higher concentrations (C_I>0.02 mg/ml) these dispersions contain some large aggregates, these can be removed by mild centrifugation. UV-vis-NIR absorbance spectroscopy can be used to monitor these dispersions before and after centrifugation. These measurements show that the absorption co-efficient approaches 3500 mlmg^{-1}m^{-1} at low concentration with an average value of ~3250 mlmg^{-1}m^{-1} in the low concentration regime. In addition the fractional aggregate concentration increases from close to zero at C_I=0.02 mg/ml to almost 100% at C_I=0.1 mg/ml.

Sedimentation and AFM measurements show that, after mild centrifugation, the dispersions are stable against both sedimentation and aggregation. AFM further shows that the bundle diameters tend to decrease with concentration until very small bundles are found at low concentration. This can be explained by an equilibrium characterized by a maximum number density of bundles. This allows the calculation of the minimum solvent volume per bundle which is very close to the volume of solvent enclosed by the sphere whose diameter is equal to the bundle length. This suggests that the bundle diameter distribution adjusts to the concentration such that the dispersion is always close to the dilute / semi-dilute boundary.

In addition a population of individual nanotubes is present at all concentrations. The fraction of individual nanotubes increases as the concentration is decreased, approaching 70% at low concentration. We can also calculate the mass fraction of individual nanotubes, which tends to 10% at low concentration. Two related quantities are the number density and mass density of individual nanotubes. These quantities are of course related and both display a maximum at approximately C_{NT}~0.01 mg/ml. This is then the optimum concentration for finding individual nanotubes. The ratio of these quantities gives the average nanotube mass which is concentration independent as expected. The average nanotube mass is ~6.8×10^5 g/mol which corresponds to an average nanotube length of ~950nm. The presence of individual nantoubes in NMP at different

concentrations was confirmed by photoluminescence spectroscopy. Both the PL intensity and ratio of PL intensity over concentration scaled with concentration in the same way as N_{Ind}/V and M_{Ind}/M_T as measured by AFM. This confirms that the AFM measurements are representative of the dispersion as a whole and not the drying phase. Finally micro-Raman measurements carried out on spin coated films confirm the presence of large quantities of individual nanotubes.

One important point can be made that applies to dispersions of all types of one-dimensional nanostructures. In many cases dispersions consisting solely of individual nanotubes are required. The standard procedure is to prepare a dispersion at reasonably high concentration and centrifuge to remove the bundles. However our work shows that an optimum concentration exists with a maximum quantity of individual nanotubes. Thus, counter-intuitively, dispersions fabricated at this (lower) concentration and then centrifuged should have a higher concentration of individual nanotubes compared to those prepared at high concentrations. This can significantly increase the concentrations of dispersions of individual nanotubes available to researchers.

4.7 References

1.   Giordani, S. et al. Debundling of single-walled nanotubes by dilution: Observation of large populations of individual nanotubes in amide solvent dispersions. Journal of Physical Chemistry B 110, 15708-15718 (2006).
2.   Ausman, K. D., Piner, R., Lourie, O., Ruoff, R. S. & Korobov, M. Organic solvent dispersions of single-walled carbon nanotubes: Toward solutions of pristine nanotubes. Journal of Physical Chemistry B 104, 8911-8915 (2000).
3.   Bahr, J. L., Mickelson, E. T., Bronikowski, M. J., Smalley, R. E. & Tour, J. M. Dissolution of small diameter single-wall carbon nanotubes in organic solvents? Chemical Communications, 193-194 (2001).
4.   Furtado, C. A. et al. Debundling and dissolution of single-walled carbon nanotubes in amide solvents. Journal of the American Chemical Society 126, 6095-6105 (2004).
5.   Krupke, R., Hennrich, F., Hampe, O. & Kappes, M. M. Near-infrared absorbance of single-walled carbon nanotubes dispersed in dimethylformamide. Journal of Physical Chemistry B 107, 5667-5669 (2003).
6.   Landi, B. J., Ruf, H. J., Worman, J. J. & Raffaelle, R. P. Effects of alkyl amide solvents on the dispersion of single-wall carbon nanotubes. Journal of Physical Chemistry B 108, 17089-17095 (2004).
7.   Liu, J. et al. Controlled deposition of individual single-walled carbon nanotubes on chemically functionalized templates. Chemical Physics Letters 303, 125-129 (1999).
8.   Maeda, Y. et al. Dispersion of single-walled carbon nanotube bundles in nonaqueous solution. Journal of Physical Chemistry B 108, 18395-18397 (2004).

9. Umek, P. et al. An effective surfactant-free isolation procedure for single-wall carbon nanotubes. Carbon 40, 2581-2585 (2002).

10. Lebedkin, S. et al. FTIR-luminescence mapping of dispersed single-walled carbon nanotubes. New Journal of Physics 5, 140 (2003).

11. Hennrich, F. et al. Raman spectroscopy of individual single-walled carbon nanotubes from various sources. Journal of Physical Chemistry B 109, 10567-10573 (2005).

12. Lian, Y. F. et al. Assignment of the fine structure in the optical absorption spectra of soluble single-walled carbon nanotubes. Journal of Physical Chemistry B 107, 12082-12087 (2003).

13. Nicolosi, V. et al. Solubility of Mo6S4.5I4.5 nanowires in common solvents: A sedimentation study. Journal of Physical Chemistry B 109, 7124-7133 (2005).

14. Nicolosi, V. et al. Solubility of Mo6S4.5I4.5 nanowires. Chemical Physics Letters 401, 13-18 (2005).

15. Coleman, J. N. et al. Improving the mechanical properties of single-walled carbon nanotube sheets by intercalation of polymeric adhesives. Applied Physics Letters 82, 1682-1684 (2003).

16. Coleman, J. N. et al. Binding kinetics and SWNT bundle dissociation in low concentration polymer-nanotube dispersions. Journal of Physical Chemistry B 108, 3446-3450 (2004).

17. Donald, A. M. & Windle, A. H. Liquid Crystalline Polymers (Cambridge University Press, Cambridge, 1992).

18. Rubinstein, M. & Colby, R. H. Polymer Physics (Oxford University Press, Oxford, 2003).

19. Tucknott, R. & Yaliraki, S. N. Aggregation properties of carbon nanotubes at interfaces. Chemical Physics 281, 455-463 (2002).

20. O'Connell, M. J. et al. Band gap fluorescence from individual single-walled carbon nanotubes. Science 297, 593-596 (2002).

21. Duesberg, G. S. et al. Experimental observation of individual single-wall nanotube species by Raman microscopy. Chemical Physics Letters 310, 8-14 (1999).

22. Coleman, J. N. & Ferreira, M. S. Geometric constraints in the growth of nanotube-templated polymer monolayers. Applied Physics Letters 84, 798-800 (2004).

23. Grujicic, M., Cao, G. & Roy, W. N. Atomistic simulations of the solubilization of single-walled carbon nanotubes in toluene. Journal of Materials Science 39, 2315-2325 (2004).

Chapter 5

Towards Solutions of Single Walled Carbon Nanotubes in Common Solvents[1]

5.1 Introduction

Nanotubes are considered insoluble in all solvents, a fact that has greatly hindered their development. Due to their size and rigidity, dissolution cannot be driven by a large mixing entropy. It is generally expected that their mixing enthalpy is so positive as to render them insoluble in all solvents. As stated earlier, a significant improvement from the various multi-phase techniques to disperse SWNTs would be to disperse them in common solvents without the aid of a third, dispersant phase. In fact, the ideal situation would be to find a solvent in which nanotubes were thermodynamically soluble, i.e., where the free-energy of mixing, ΔG_{Mix}, is negative. The aim of this chapter is to demonstrate spontaneous exfoliation of single-walled carbon nanotubes on dilution of nanotube dispersions in a common solvent, N-methyl-pyrrolidone (NMP). Light-scattering measurements show the enthalpy of mixing to be approximately zero and hence the free-energy of mixing to be negative, confirming athermal solubility. STM measurements show that NMP is sequestered inside bundles even after drying. Annealing removes this NMP and yields pristine tubes, indicating that the large solvent-nanotube interfacial energy required for solubility is solely due to dispersion type interactions. Experiments, supported by a simple model, show that the successful solvents for nanotubes are those with surface tensions close to that of graphite.

5.2 Experimental Procedure

Sonicated Samples

Purified single walled nanotubes (HiPCO) were purchased from Carbon Nanotechnologies Inc and used as supplied (lot #PO289). Dilution series were produced by two methods. In the first case, a stock dispersion of pristine HiPCO nanotubes was prepared in N-methyl-2-pyrrolidone (10ml) at a maximum nanotube concentration of 1 mg/ml, by sonicating for 2 minutes using a high power ultrasonic tip processor, Vibra Cell CVX (150W, 60kHz). In order to produce a range of concentrations this initial dispersion was then serially diluted to produce a range of dispersions with concentrations from 1 mg/ml to 0.001 mg/ml. After each dilution, the dispersions were sonicated for 2 minutes by tip, followed by 4 hours in a low power ultrasonic bath (Branson 1510) followed by a 1 minute with the sonic tip. All dispersions were subsequently centrifuged at 5500 rpm (~2700g) for 90 minutes to remove any large aggregates[2]. These aggregates are thought to be associated with the formation of a nematic phase at higher concentration which co-exists in equilibrium with an isotropic phase[2]. Centrifugation is known to remove the nematic phase, leaving only an isotropic nanotube dispersion[2, 3]. UV-vis-NIR absorption measurements were made before and after centrifugation using a Perkin Elmer Lambda 900 UV-vis-NIR spectrometer to determine the absolute concentration after centrifugation.

In the second method, a stock dispersion of pristine HiPCO nanotubes was prepared in N-methyl-2-pyrrolidone (10m) at a maximum nanotube concentration of 1 mg/ml, by sonicating for 2 minutes using a high power ultrasonic tip processor, Vibra Cell CVX (150W, 60kHz), 4 hours in a sonic bath followed by 1 minute with a sonic tip. This dispersion was then centrifuged at 5500 rpm (~2700g) for 90 minutes to remove the nematic phase. UV-vis-NIR absorption measurements were made before and after centrifugation using a Cary 6000-i UV-vis-NIR spectrometer to determine the absolute concentration after centrifugation. This stock dispersion was *then* subsequently diluted to produce a dilution series. Both procedures gave very similar results in terms of concentration dependent diameter distributions and populations of individual nanotubes.

In order to measure the dispersibility for different solvents, dispersions of nanotubes were prepared in a range of solvents (10mL) at a nanotube concentration of 0.1 mg/ml, by sonicating for 2 minutes using a high power ultrasonic tip processor, Vibra Cell CVX (150W, 60kHz), 4 hours in a sonic bath followed by 1 minute with a sonic tip. This dispersion was then centrifuged at 5500 rpm (~2700g) for 90 minutes to remove the nematic phase. UV-vis-NIR absorption measurements were made before and after

centrifugation using a Cary 6000-i UV-vis-NIR spectrometer to determine the fraction remaining after centrifugation.

Non-Sonicated Samples.

In order to prepare these samples, the two procedures described above were employed with some slight variation. A stock sample was made, as before, by sonicating the nanotubes in NMP. This initial sonication step was the only sonication applied to these samples. This stock dispersion was diluted in two ways, as described above, to produce dilution series. However, for these samples no sonication was applied after any of the dilutions. This means that no energy was added to the dispersions after dilution to facilitate debundling.

Sample Characterisation

Immediately after preparation, each sample was deposited on chemically functionalised silicon substrate as described by Liu et al[4]. Atomic force microscopy (AFM) studies were carried out in tapping mode using a Multimode Nanoscope IIIA. POINTPROBE silicon cantilevers (typical tip radius $R_{Tip} \sim 60nm$) were used in all cases (all diameter measurements were made by measuring the height of the bundle above the surface). Near-infrared photoluminescence (PL) measurements were carried out on SWNT dispersions using an Edinburgh Instruments FLS 920 fluorescence spectrometer fitted with a liquid nitrogen cooled Hamamatsu R5509 near-infrared photo-multiplier tube and a tunable, monochromated, Xenon lamp source. For each concentration, a PL map was compiled by scanning emission spectra (900 – 1400nm, in 4nm steps) for respective excitation wavelengths in the range of 550 – 890nm (also in 4nm steps). Excitation and emission slit widths were 10nm and 15nm respectively and a dwell time of 0.5sec was used for all measurements.

5.3 Results and Discussion

Dispersion Analysis

It is known that SWNT can be dispersed[5, 6] and even exfoliated by sonication and dilution in NMP[2]. Here we suggest that these dispersions are actually solutions in the true thermodynamic sense. We begin by characterising SWNT-NMP dispersions prepared at a range of concentrations by successive dilution *and* sonication steps[2]. By casting each

77

dispersion onto SiO_2 substrates and characterising by AFM, large populations of one dimensional objects were observed as shown in figure 5.1.
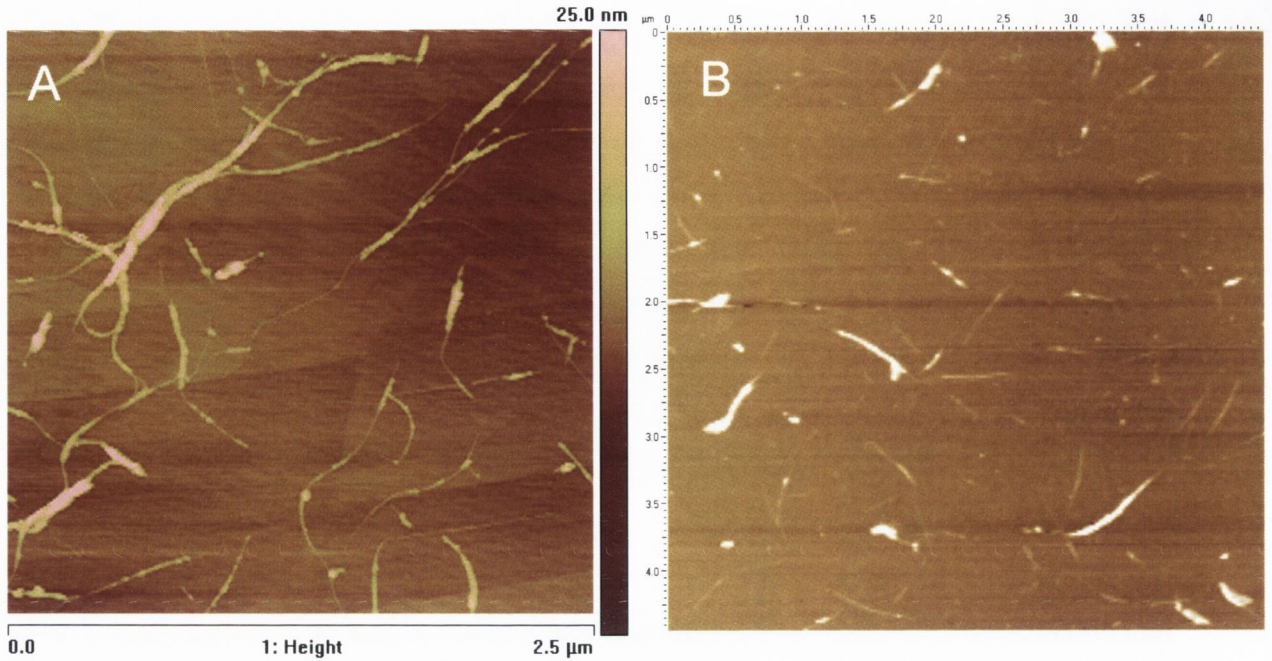
Figure 5.1

AFM images for samples dropped from SWNT dispersions with concentrations of (a) 0.00625 mg/ml and (b) 0.0011 mg/ml.

These images were analysed by measuring the diameters and lengths of the objects. For statistical analysis, any object observed with diameter less than 1.4nm was considered an individual nanotube. From this, the root-mean-square bundle diameter as shown in figure 5.2 (open diamonds) was determined. The bundle diameter tends to decrease with decreasing nanotube concentration and this can be modelled under the assumption that a concentration-independent equilibrium number-density of bundles exists, leading to a scaling relationship between diameter and concentration[2]:

$$D_{rms} = \sqrt{\left\langle D_{Bun}^2 \right\rangle} \approx \left[\frac{4C_{NT}}{\rho_{Bun} \pi L_{bun} (N/V)_{Eq}} \right]^{1/2} \tag{5.1}$$

where D_{Bun}, L_{Bun} and ρ_{Bun} are the bundle diameter, length and density, C_{NT} is the nanotube concentration (mg/ml) and $(N/V)_{Eq}$ is the equilibrium bundle number density. This equation provides an excellent fit to the data in figure 5.2 (dashed line) until low concentration when debundling ceases as the dispersions become dominated by individual nanotubes.

Figure 5.2

Root mean square bundle diameter distributions (with standard error) as a function of nanotube concentration in NMP. Samples were prepared by sonicating after every dilution step (open diamonds) but also by dilution *without sonication* (WS) from a stock solution. Non-sonicated samples were measured immediately after dilution (red triangles) and at equilibrium (168 hours after dilution) (black squares). The non-sonicated equilibrium dispersions were prepared by two different methods (see Experimental Procedure).
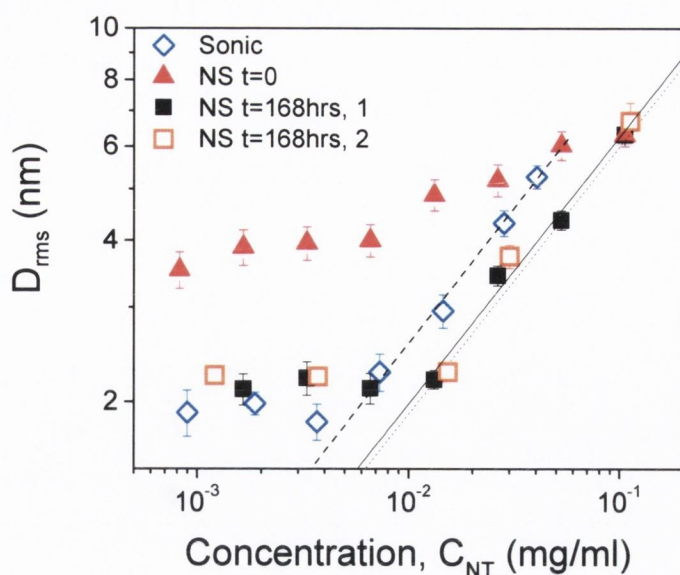
While we might expect such concentration dependent exfoliation to be accelerated by sonication, a stable equilibrium number-density can only occur as a result of a dynamic equilibrium, with nanotubes constantly adsorbing and desorbing from the bundle surface long after sonication has ceased[7]. Such equilibrium requires nanotubes to be soluble *in a thermodynamic sense*. Thus, a dynamic equilibrium must eventually be established even in the absence of sonication.

In order to investigate this we made a set of samples, at a range of concentrations by dilution from a stock dispersion *without additional sonication*. Drops were deposited *immediately* after dilution for AFM analysis, bundle diameter distributions measured and D_{rms} calculated. If nanotubes form a colloidal dispersion (Colloidal dispersions are homogeneous suspensions of extremely small particles in fluids[8]), as is generally thought, the mean bundle diameter should be constant for all concentrations in the absence of sonication.

The results plotted in figure 5.2, show a reduction in D_{rms} as C_{NT} is decreased, indicating spontaneous exfoliation. That D_{rms} does not immediately scale with $\sqrt{C_{NT}}$ is unsurprising as it may take time to reach equilibrium. To check this, a range of fresh

samples were diluted without sonication and the bundle diameters measured as a function of time by removing small aliquots and analyzing with AFM. The results in figure 5.3a show a steady reduction in bundle diameter as a function of time, saturating after ~170 hours. This is a clear demonstration of the approach to equilibrium by spontaneous exfoliation.
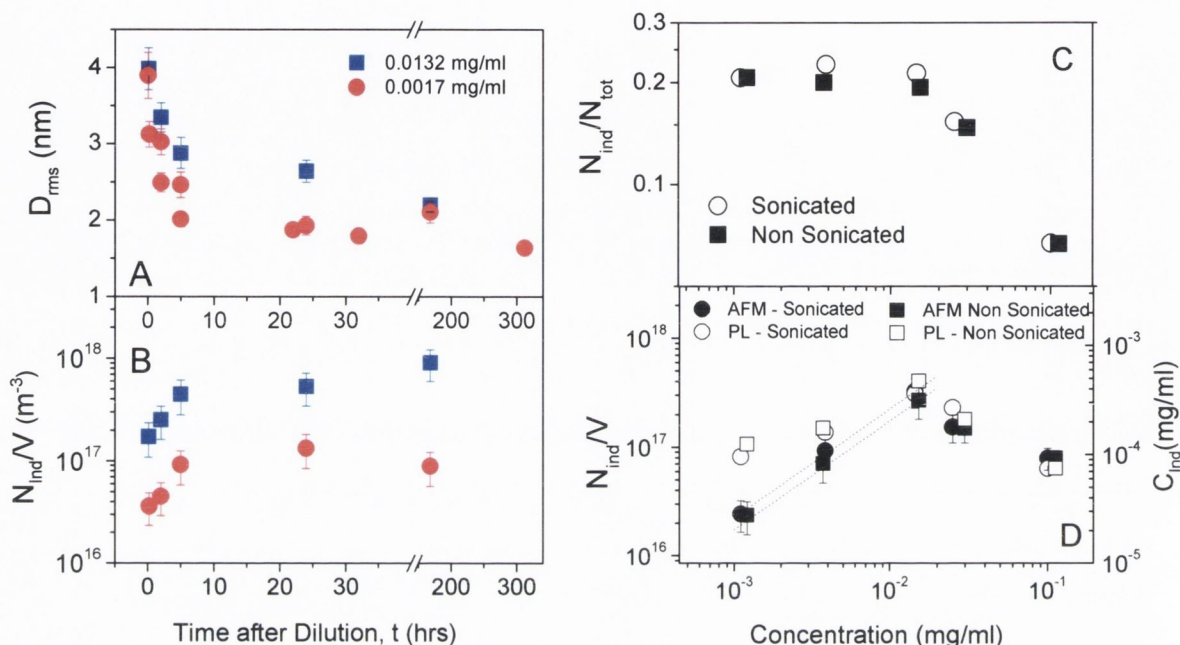
Figure 5.3

(a) and (b) D_{rms} (with standard error) and number density of individual nanotubes as a function of time after dilution for samples diluted from 0.1 mg/ml to two concentrations, 0.0132 mg/ml and 0.0017 mg/ml. (c) and (d) Fraction of individual nanotubes and number density of individual nanotubes as a function of concentration for the samples prepared with sonication after every dilution step (open circles) and without sonication and measured 168 hours after dilution (black square). The right axis in (d) shows the concentration of individual SWNTs. Also shown are measurements of nanotube photoluminescence intensity as a function of intensity

Measurements of D_{rms} versus C_{NT} for the non-sonicated samples following 168 hr equilibration time are also shown in figure 5.2 (black squares). It can clearly be seen that, at equilibrium, D_{rms} decreases strongly with decreasing concentration before saturating at a C_{NT}~0.01 mg/ml, in similar fashion to the sonicated samples. The solid line is a fit to equation 5.1 showing that the equilibrium is also characterised by a fixed equilibrium bundle number-density.

Diameter distributions for each dispersion were measured using NANOSCOPE V613B21 software by tracing cross sections. For each concentration, diameters were measured for 150 nanotubes from different parts of the substrate. These data are presented in figure 5.4 as a histogram for each concentration 168hours after the samples were made without sonication. The raw data contained in these histograms could be used to do further statistical analysis as described by Giordani et al[2] and demonstrated in previous chapters.
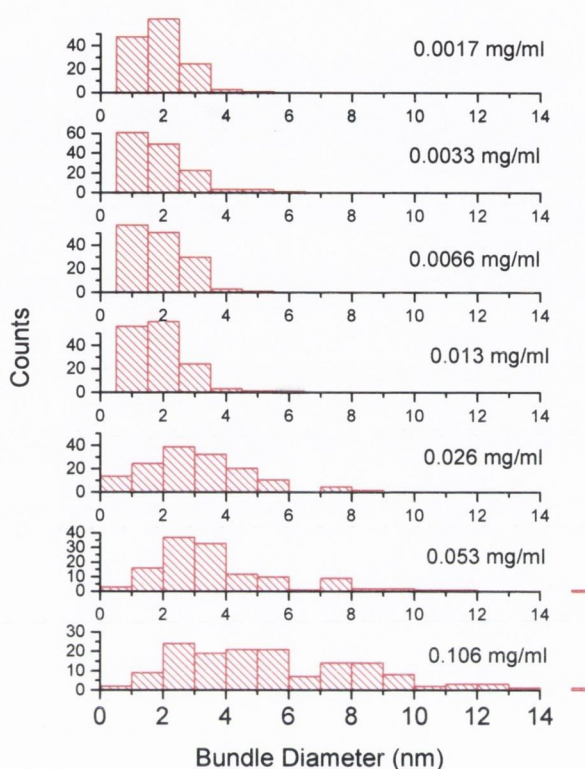
Figure 5.4

Diameter distributions as a function of concentration for the non-sonicated sample deposited 168 hours after dilution.

In addition, length measurements were calculated using Image Tool software. Mean and standard deviations were calculated from a sample of 50 lengths. Of these 50, 25 were bundles while 25 were individual nanotubes (D<1.4nm). Both bundle and nanotube lengths were found to be concentration independent. In the non-sonicated samples the individual and bundle lengths were found to be: $<L_{Ind}>$=1.2±0.1µm and $<L_{Ind}>$=2.4±0.2µm. In the sonicated samples the individual and bundle lengths were found to be: $<L_{Ind}>$=1.1±0.1µm and $<L_{Ind}>$=2.1±0.2µm.

We suggest that after dilution, spontaneous desorption of nanotubes from bundles combined with coalescence of individual nanotubes with bundles as well as with other nanotubes leads to equilibrium. The equilibrium will be concentration dependent due to the

concentration dependence of the coalescence rate. This model also predicts more individual nanotubes at lower concentrations. The fraction of individual nanotubes in the sample can be estimated from the AFM data[2] and plotted for both the sonicated and non-sonicated samples in figure 5.3c. In each case, the fraction of individual nanotubes increases with dilution, saturating at ~20% at low concentration. The absolute number density of individual nanotubes and hence the concentration of individuals can also be estimated from the AFM data[2] (figure 5.3d). The initial increase, with decreasing concentration, is indicative of efficient exfoliation on dilution. The linearity of this curve at low concentration represents the saturation of the population of individual nanotubes at low concentration.

We can also use these statistics to monitor the kinetics. The number-density of individual nanotubes was measured as a function of time, after dilution (without sonication) from the AFM data (figure 5.3b) and confirms that the approach to equilibrium is accompanied by an increase in the population of individual nanotubes.

To rule out the influence of drying effects on the AFM data we measured nanotube photoluminescence spectra as a function of concentration. Figure 5.5 shows a typical PL map for SWNT dispersed in NMP at C=0.01 mg/ml. While the PL is relatively weak compared to that generally measured for surfactant dispersed nanotubes[9], a number of peaks can clearly be observed. As the PL comes predominately from individual nanotubes, the PL intensity is expected to display similar concentration dependence to that of N_{Ind}/V^2. This is demonstrated in figure 5.3d confirming the validity of the AFM statistics. In fact we observe that the PL intensity is proportional to the measured N_{Ind}/V for both the sonicated and non-sonicated samples as shown in figure 5.6.
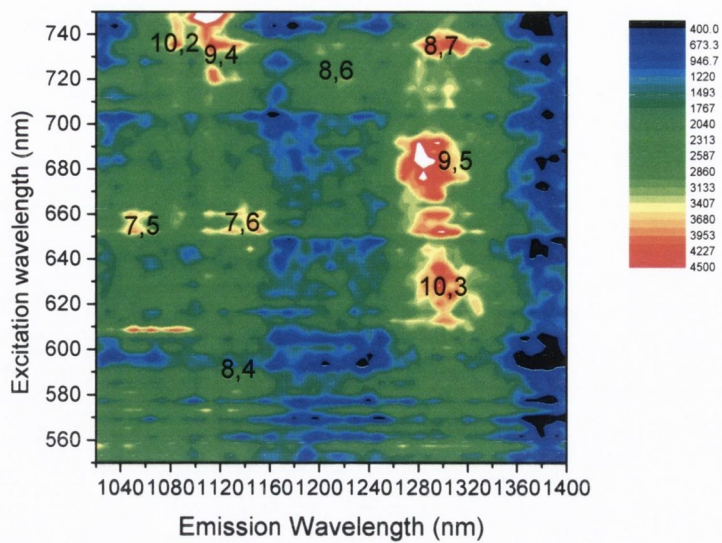
Figure 5.5

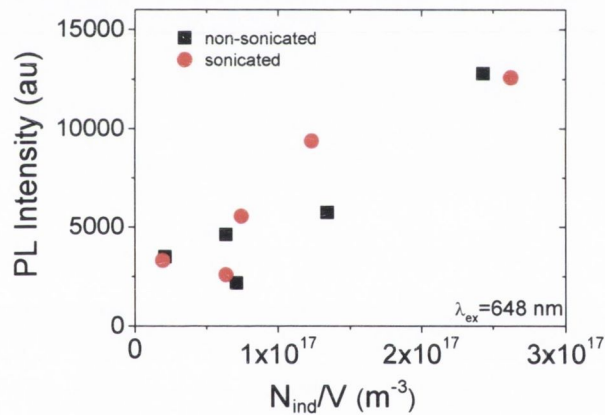A Pl contour map for SWNT dispersed in NMP at C=0.01 mg/ml.

Figure 5.6

Demonstration of linearity between Pl intensity and number density of individual nanotubes as measured by AFM. This is expected as Pl is thought to come predominately from individual nanotubes.

Thermodynamics of Mixing

Spontaneous exfoliation implies solubility and so a negative ΔG_{Mix}. To understand this, it is important to estimate the magnitude of the contributions of ΔH_{Mix} and ΔS_{Mix}.

Calculation of Entropy of Mixing[3]

The entropy of mixing can by calculated using Flory's equation to be extremely small[10, 11]. The entropy of mixing, S_{Mix}, of an isotropic array of rigid rod molecules, in this case nanotubes, can be expressed as[11]

$$S_{Mix} = k \ln Z = -k \left[n_S \ln(1-\phi) + n_{NT} \ln \frac{\phi}{\sigma x} + n_{NT}(x-1) \right] \qquad (5.2)$$

Where Z is the partition function of the system, n_S and n_{NT} are the numbers of solvent molecules and nanotubes, respectively, σ is the rotational degeneracy factor, and x is the nanotube aspect ratio. The number of molecules of each phase, n_i, can be related to the volume fraction, ϕ_i by $n_i = N_A \phi V_{Mix} / \overline{V_i}$, where $\overline{V_i}$ is the molar volume of the species and V_{Mix} is the total volume, giving, when multiplied by the absolute temperature, T

$$T \frac{\Delta S_{mix}}{V_{mix}} = -\frac{RT}{\overline{V_s}} \left[(1-\phi)\ln(1-\phi) + \frac{\overline{V_s}}{\overline{V_{NT}}} \phi \left(\ln\left(\frac{\phi}{\sigma x}\right) + (x-1) \right) \right] \qquad (5.3)$$

Thus a mixture of nanotubes in a given solvent will be a solution when $\Delta G_{Mix} < 0$, ie when

$$-\frac{RT}{\overline{V_s}} \left[(1-\phi)\ln(1-\phi) + \frac{\overline{V_s}}{\overline{V_{NT}}} \phi \left(\ln\left(\frac{\phi}{\sigma x}\right) + (x-1) \right) \right] > \chi \frac{RT}{\overline{V_s}} \phi(1-\phi) \qquad (5.4)$$

Expanding the natural log in the first term in the square brackets as a Taylor series and neglecting quadratic and higher terms of V_f, and setting $x-1 \approx x$ we get

$$\chi < \left(1 - \frac{\overline{V_s}}{\overline{V_{NT}}} x\right) - \frac{\overline{V_s}}{\overline{V_{NT}}} \ln\left(\frac{\phi}{\sigma x}\right) \qquad (5.5)$$

In terms of the lattice model used to derive this equation, $\overline{V_{NT}} / \overline{V_S} \equiv x$. This means the first term can be eliminated, allowing us to write

$$\chi < \frac{\overline{V_s}}{\overline{V_{NT}}} \ln\left(\frac{\sigma}{\phi} \frac{\overline{V_{NT}}}{\overline{V_s}}\right) \qquad (5.6)$$

The molar volume of NMP is 96×10^{-6} m^3/mol. Calculating the molar volume of SWNT from their average molecular weight (700,0000g/mol) taking the nanotube density to be ~1830 kg/m^3 (this figure is calculated taking an average diameter of 1.0nm and including the contribution of residual catalytic iron; see appendix) gives a figure of $\overline{V_{NT}}$ =0.39

---

[3] This calculation was carried out by Prof. JN Coleman, *Sch. of Physics, TCD.*

m^3/mol. While the value for the rotational degeneracy factor is not known we conservatively set σ=1. Thus for nanotubes to be soluble in the concentration range studied: χ<0.005.

Modeling the Enthalpy of Mixing[3]

For solubility, $\Delta H_{Mix} < T\Delta S_{Mix}$, and thus ΔH_{Mix} must be extremely small or negative. To estimate the enthalpy of mixing for nanotubes in a solvent, we estimate the energy balance between isolated nanotubes and solvent and the nanotube-solvent mixture. We calculate the energy required to remove all solvent molecules and all nanotubes from the starting material to infinity. This involves the solvent cohesive energy and the effective nanotube surface energy (as discussed in the appendix). We then calculate the energy gained by assembling nanotubes into bundles of a given radius, R_{bun}, and by re-assembling the solvent molecules into the bulk phase, but leaving voids for the nanotubes. Finally, we calculate the energy of interaction when the nanotubes are placed in the solvent voids. The difference between the first 2 terms and the final 3 terms gives the enthalpy of mixing per unit volume of mixture:

$$\frac{\Delta H_{Mix}}{V_{Mix}} \approx \frac{2}{R_{Bun}}\left(\delta_{NT} - \delta_{sol}\right)^2 \phi \qquad (5.7)$$

where $\delta_i = \sqrt{E_{Sur}^i}$, and ϕ is the nanotube volume fraction. Thus, the enthalpy of mixing is dependent on the balance of nanotube and solvent surface energies. This equation is very similar to the famous Hildebrand-Scratchard equation[12] with the surface energy taking the role normally occupied by the cohesive energy density in molecular mixtures. (see appendix for calculation of Enthalpy of Mixing)

Equation 5.7 predicts that ΔH_{Mix} is minimised when the effective nanotube surface energy matches that of the solvent. To test this we measured the dispersibility of nanotubes in a large range of solvents by monitoring the absorbance before and after a mild centrifugation step. The 11 best solvents investigated are shown in table 1 showing the fraction of SWNTs remaining after weak centrifugation. The dispersibility is plotted as a function of solvent surface tension in figure 5.7, and shows a strong peak around 40 mJ/m^2. The solvent surface tensions can be transformed into surface energy using a universal value for surface entropy of ~0.1 mJ/m^{2}K[13, 14] (the top axis of figure 5.7) demonstrating that successful solvents have a surface energy very close to literature values of nanotube/graphite surface energy[15-18], which we can estimate from the peak position to be

[3] Modelling and calculation carried out by Prof. JN Coleman, *Sch. of Physics, TCD.*

~70 mJ/m^2. Coupled with Equation 5.7, this strongly suggests that the enthalpy of mixing for nanotubes dispersed in good solvents such as NMP is in fact very close to zero. In addition, it predicts that good solvents are characterised by surface tensions in the region of 40 mJ/m^2. Among the solvents with high dispersability in figure 5.7 are dimethylformamide (DMF) and dimethylacetamide (DMA), both well known for their nanotube dispersal properties[5, 6].

Solvent name (abbreviation)	Remaining sample after centrifugation (%)	Standard deviation
1-Methyl-2-pyrrolidinone (NMP)	68	13
3-Aminopropyltriethoxysilane	31	18
1-Dodecyl-2-pyrrolidinone (N12P)	30	4
1-Octyl-2-pyrrolidone (N8P)	25	13
1,3-Dimethyl-2-Imidazolidinone (DMEU)	25	13
N,N-Dimethylformamide (DMF)	24	10
N,N-Dimethylacetamide (DMA)	18	12
3-Aminopropyltrimethoxysilane	16	12
γ-Butyrolactone	9	4
1-Vinyl-2-pyrrolidone (NVP)	7	2
Chloroform	6	3

Table 5.1 Percentage remaining sample after centrifugation for range of solvents.
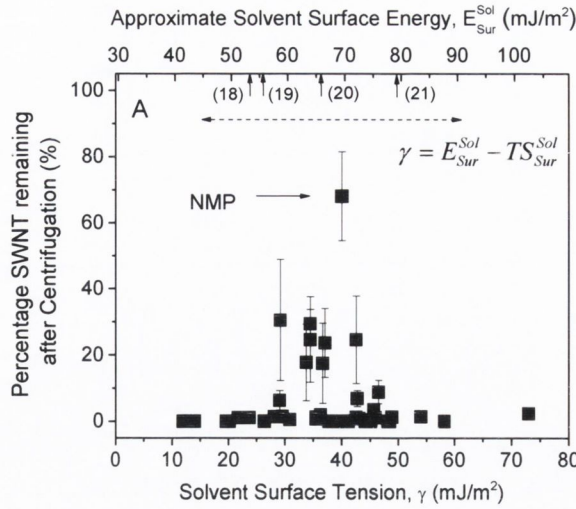
Figure 5.7

Fraction of nanotubes remaining after centrifuging dispersions (C=0.1 mg/ml) made in a range of solvents as a function of solvent surface tension (bottom axis). The best 11 solvents were measured 5 times and the mean and standard deviation plotted (Table 1). The top axis shows the approximate solvent surface energy. The horizontal arrow shows the approximate range of measurements of nanotube and graphite surface energy reported in the literature. The vertical arrows indicate four typical literature values.

Measurement of the Enthalpy of mixing

To quantify these observations we note that ΔH_{Mix} can be expressed in terms of the Flory-Huggins parameter[19], χ, which for our purposes can be written as:

$$\frac{\Delta H_{Mix}}{V_{Mix}} = \chi \frac{RT}{\overline{V}_s} \phi(1-\phi) \tag{5.7}$$

where $\overline{V}_S$ is the solvent molar volume and ϕ is the nanotube volume fraction. An absolute measurement of the free energy of mixing can be achieved by measuring χ. In an ideal solution, χ is zero, but in general is non-zero and is related to the second virial coefficient (B_2) in the expansion of osmotic pressure in terms of solute content by[20]:

$$\chi = \frac{1}{2} - B_2 \overline{V}_S \rho_{NT}^2 \tag{5.8}$$

where ρ_{NT} is the nanotube density (See Appendix for justification).

The second virial coefficient was determined by measuring the elastically scattered light intensity from our nanotube dispersions, using a Static Light Scattering (SLS) Photon

Counting Spectrometer[ξ] (See appendix). The scattering intensity, usually expressed via the Rayleigh ratio, is related to C_{NT} via B_2 through the Debye light scattering equation [21, 22], which for experimental convenience can be expressed as

$$\frac{C_{NT}}{S - S_0} = \frac{B_2}{K'} C_{NT} + \frac{1}{M_w K''} \tag{5.9}$$

where S and S_0 are dimensionless numbers proportional to the solution and pure solvent scattering intensities respectively[20]. The quantities K' and K'' are instrumental constants unique to the SLS instrument and were obtained from plots of $C/(S-S_0)$ vs C for the known molecular weight (M_w) standards and literature values for B_2 to be $K'=1.0325(5)$m^{3}mol/kg and $K''=9.0570(5)$m^{3}mol/kg^2. Subsequent measurement of B_2's and χ's for known materials were uniformly within a few percent of the literature values [23]. A plot of $C_{NT}/(S-S_0)$ vs. C_{NT} for SWNT in NMP (Figure 5.8) was fit with Equation 5.9 giving $B_2=1.78\times10^{-3}$m^{3}mol/kg. Taking the density of HiPCO nanotubes as 1830 kg/m^3 (See Appendix) and $\overline{V}_S=96\times10^{-6}$ m^3/mol we calculate a value for $\chi= -0.074$. The assumption of $\rho_{NT}=1830$ kg/m^3 is the limiting factor in the accuracy of χ. In fact, χ, and so ΔH_{Mix}, is negative as long as the nanotube density is greater than 1700 kg/m^3, suggesting that only nanotubes with diameters less than 1nm are soluble (Appendix). This is supported by the lack of high diameter nanotubes observed in the PL.
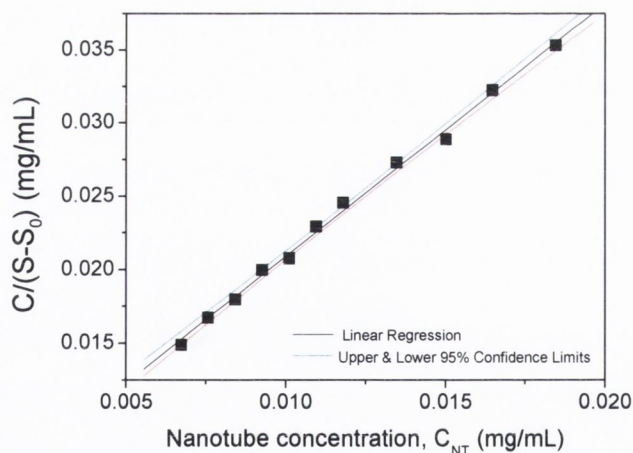

Figure 5.8

The slope of an inverse scattering intensity plot yields the 2nd virial coefficient, B_2, used to determine the Flory Huggins parameter.

Scanning Tunnelling Microscopy[φ]

Finally, we address the role of the initial sonication, and the affinity of NMP for the nanotubes themselves. NMP was evaporated from nanotube solutions to form a dry powder, which was transferred to a fiberglass substrate and used in a contact-transfer process[24] to deposit tubes on a Si(100)-2×1 surface under UHV (3×10^{-11} mbar) conditions. Figure 5.9A shows two bundles on what was initially an atomically clean surface. Neither the surface nor the tubes can be imaged with atomic resolution. Figure 5.9B shows a similar sample which had been outgassed for 30 s at approx. 300C in ultra high vacuum. Both the surface and tubes are now atomically resolved. Similar results are routinely obtained when pristine, non-solvent treated tubes are used, indicating that the poor resolution in figure 5.9A is due to the presence of NMP molecules on the surface. NMP is expected to chemisorb on the Si(100) surface through the nitrogen-containing group[25, 26], so that, on contact, the surface effectively titrates molecules that are present *in the dried bundles*. In addition some NMP remains tenaciously bound to the tubes even under UHV conditions. However, the reversibility of the NMP-tube binding interaction is clearly evident from the perfection of the bundle surface after annealing (Figure 5.9B), indicating the NMP physisorbs onto the nanotube surface, a prerequisite for any effective solvent. Remarkably, we often find evidence for molecules emerging from bundles (circle in figure 5.9B), but which ultimately migrate and become irreversibly bound to the Si(100) surface, leaving behind defect-free tubes (Figure 5.9C and D). Based on these results and the data in figures 5.2 and 5.3, we speculate that the role of the initial sonication is to promote the insertion of solvent molecules into bundles. Solvent intercalation weakens the inter-tube interaction, thus facilitating the formation of solvated tubes.
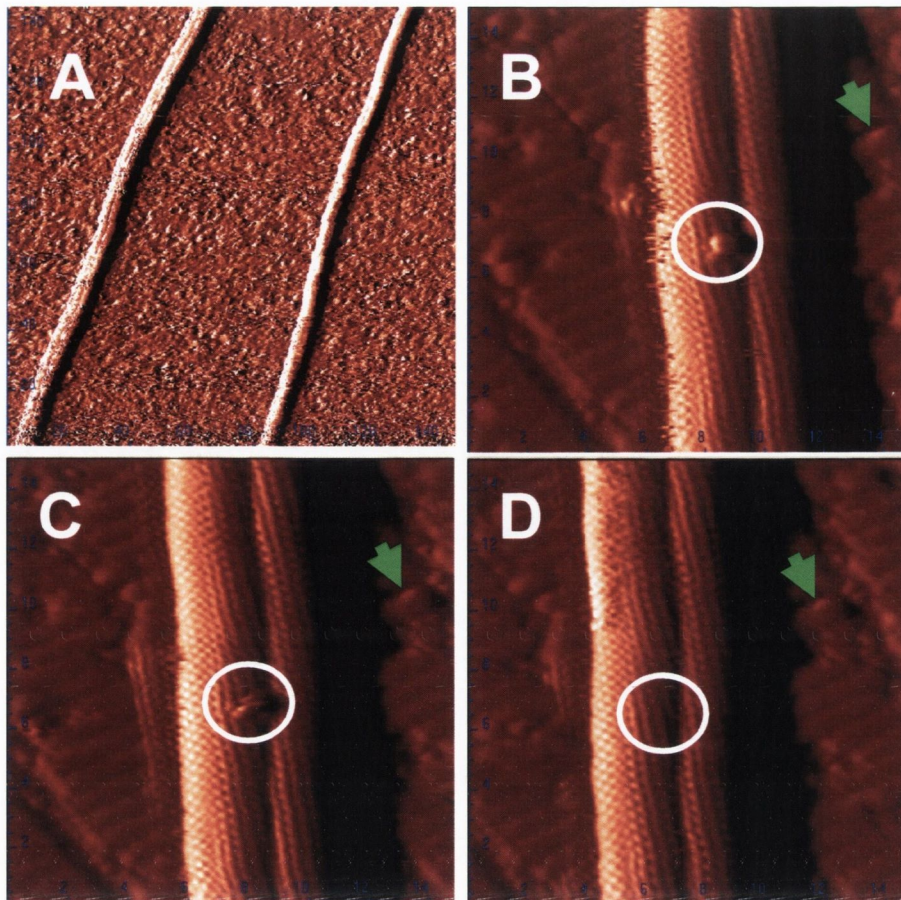
Figure 5.9

STM images of SWNTs deposited on Si(001) surfaces. A) Following transfer of dried solvent-processed nanotubes (1.2V, 80pA) B)-D) Following brief degas (300 C) prior to transfer to Si(100)(0.44V, 120pA). Note evidence of molecule migration on SWNTs (circles). Green arrow is a reference point on the surface.

5.4 Conclusions

In conclusion, we have presented evidence that nanotubes, dispersed in NMP, can spontaneously exfoliate on dilution resulting in a decrease in bundle diameter and an increase in population of individual nanotubes to equilibrium values. We show that nanotube dispersibility is maximised in solvents whose surface energy matches that of graphitic surfaces, consistent with NMP dispersions having close to zero enthalpy of mixing. This has been confirmed by a measurement of the Flory-Huggins parameter showing that the enthalpy of mixing is negative and confirming true solubility of SWNT in NMP. STM measurements show that NMP enters the bundles during sonication and

remains strongly bound even at UHV. However, it can be removed by heating to 300C, leaving perfect nanotubes showing that the NMP was physisorbed, probably by Van der Waals interactions, onto the nanotube surface. This work not only answers the fundamental question of solubility of nanotubes but elucidates the solvent properties required for solubility. This provides a template to choose from a range of potential nanotube solvents, opening up an array of solution based experimental and processing procedures.

5.5 Appendix

Calculation of Enthalpy of Mixing[3]

Consider an isolated volume of solvent, V_{sol}, and an isolated mass of nanotubes, M_{NT}. The nanotubes can be considered as arranged in bundles of radius R_1 and length, L_1. The number of such bundles is $N_1 = M_{NT} / \rho_{NT} \pi R_1^2 L_1$, where ρ_{NT} is the nanotube density.

The enthalpy of mixing of solvent and nanotubes can be found by calculating the energy required to separate all molecules to infinity minus the energy to bring them back in the form of a solvent-nanotube dispersion. This can be divided into five energetic components.

1. The energy required to separate all nanotubes to infinity is given by the energy required to create the surfaces associated with the individual nanotubes and so is related to the effective nanotube surface energy, E_{Sur}^{NT}, which can be thought of as the inter-nanotube binding energy per unit area of surface.

$$E_1^{NT} = N_1 \left[\left(\frac{\pi R_1^2 L_1}{\pi r^2 l} \right) - 2\pi R_1 L_1 \right] E_{Sur}^{NT} \qquad (X1)$$

where the term in the round brackets represents the number of nanotubes per bundle (r being the radius of a single nanotube) and the second term in the square brackets represents a correction for the outer surface of the bundle.

2. The energy required to remove all the solvent molecules to infinity is given by

$$E_1^{Sol} = V_{sol} E_{Coh}^{Sol} - A_1^{Sol} E_{Sur}^{Sol} \qquad (X2)$$

where E_{Coh}^{Sol} is the solvent cohesive energy, E_{Sur}^{Sol} is the solvent surface energy and A_1^{Sol} is the external surface area of the solvent.

---

[3] This calculation was carried out by Prof. JN Coleman, *School of Physics, TCD*

3. The energy retrieved by bringing the nanotubes back from infinity to form N_2 bundles of radius, R_2, and length, L_2, is similar to E_1^{NT} and is given by

$$E_2^{NT} = N_2 \left[\left(\frac{\pi R_2^2 L_2}{\pi r^2 l} \right) - 2\pi R_2 L_2 \right] E_{Sur}^{NT} \qquad (X3)$$

Where $N_2 = M_{NT} / \rho_{NT} \pi R_2^2 L_2$

4. We can also calculate the energy released by bringing the solvent molecules back from infinity to form a liquid but leaving voids *to accommodate the nanotube bundles*:

$$E_2^{Sol} = V_{sol} E_{Coh}^{Sol} - A_2^{Sol} E_{Sur}^{Sol} - A_{Inter}^{NT-sol} E_{Sur}^{Sol} \qquad (X4)$$

Here A_2^{Sol} is the new solvent (outer) surface area, while A_{Inter}^{NT-sol} is the surface area of the voids which will accommodate the bundles.

5. Finally we must calculate the interfacial energy associated with placing the bundles in the voids:

$$E_2^{NT-Sol} = 2 A_{Inter}^{NT-Sol} E_{Inter}^{NT-Sol} = 2 N_2 2\pi R_2 L_2 E_{Inter}^{NT-Sol} \qquad (X5)$$

where E_{Inter}^{NT-Sol} is the solvent nanotube binding energy per unit area. The factor of two comes from the fact that we are passivating two surfaces, that of the nanotube and that of the solvent.

The enthalpy of mixing is given by

$$\Delta H_{Mix} = E_1^{NT} + E_1^{Sol} - (E_2^{NT} + E_2^{Sol} + E_2^{NT-Sol}) \qquad (X6)$$

This can be calculated using the expressions outlined above. A number of approximations can be made. One is that the solvent external surface area is the same before and after mixing with the nanotubes ($A_2^{Sol} \approx A_1^{Sol}$), a reasonable approximation at low nanotube content. In addition, we assume that the bundles that exist in the nanotube powder are much larger than those in the dispersion ($R_1 \gg R_2$). Including these approximations, this works out to be

$$\Delta H_{Mix} \approx 2 \frac{M_{NT}}{R_2 \rho_{NT}} \left[E_{Sur}^{NT} + E_{Sur}^{Sol} - E_{Inter}^{NT-Sol} \right] \qquad (X7)$$

Finally, we note that the volume fraction of nanotubes, ϕ, is given by $\phi = M_{NT} / \rho_{NT} V_{Mix}$, where V_{Mix} is the volume of the mixture. Then:

$$\frac{\Delta H_{Mix}}{V_{Mix}} \approx 2 \frac{\phi}{R_2} \left[E_{Sur}^{NT} + E_{Sur}^{Sol} - E_{Inter}^{NT-Sol} \right] \qquad (X8)$$

In general, for materials that interact predominately by dispersive interactions we can estimate E_{Inter}^{NT-sol} from the geometric mean approximation[12, 27]:

$$E_{Inter}^{NT-sol} \approx \left[E_{Sur}^{NT} E_{Sur}^{Sol} \right]^{1/2} \tag{X9}$$

Substituting this in above we get

$$\frac{\Delta H_{Mix}}{V_{Mix}} \approx \frac{2}{R_{Bun}} \left(\delta_{NT} - \delta_{sol} \right)^2 \phi \tag{X10}$$

where

$\delta_i = \sqrt{E_{Sur}^i}$ and where we write R_2 as R_{bun} for clarity.

The solvent surface energy, E_{Sur}^{Sol}, is related to the surface tension, γ^i, by [13]:

$$\gamma = E_{Sur}^{Sol} - TS_{Sur}^{Sol} \tag{X11}$$

where S_{Sur}^{Sol} is the solvent surface entropy. The surface entropy is a generic liquid property that tends to have values in the range 0.07-0.14 mJ/m^{2}K. Liquids of a given class tend to have very similar values of S_{Sur}^{Sol}, with DMF and toluene for example shown to have values close to $S_{Sur}^{Sol} = 0.11 mJ/m^2 K$ [14]. Thus, we take the universal value to be ~0.1 mJ/m^{2}K and use this to transform between γ and S_{Sur}^{Sol} in figure 5.7.

It should be pointed out that, in the literature, the enthalpy of mixing is generally expressed as

$$\Delta H_{Mix} = \chi R T n_1 \phi \tag{X12}$$

where χ is the Flory Huggins parameter and n_1 is the number of moles of solvent present. However substitution of n_1 by

$$n_1 = \frac{(1-\phi)V_{Mix}}{\overline{V}_S} \tag{X13}$$

gives the expression quoted in equation 5.7 (main text) ie

$$\frac{\Delta H_{Mix}}{V_{Mix}} = \chi \frac{RT}{\overline{V}_s} \phi(1-\phi)$$

Free energy and the virial coefficient

The osmotic pressure of a solution is related to the free energy of mixing by [19]

$$\Pi = -\frac{\partial G_{Mix}}{\partial V_{Mix}} \tag{Y1}$$

Inserting equations 5.7 and 5.3 (from main text) in the expression $\Delta G_{Mix} = \Delta H_{Mix} - T\Delta S_{Mix}$, we get an expression for the free energy of mixing for rigid rods dispersed in a solvent:

$$\Delta G_{mix} = V_{mix} \frac{RT}{\overline{V}_s}\left[\chi\phi(1-\phi) + (1-\phi)\ln(1-\phi) + \frac{\overline{V}_s}{\overline{V}_{NT}}\phi\left(\ln\left(\frac{\phi}{\sigma x}\right) + (x-1) \right) \right] \qquad (Y2)$$

Differentiating with respect to V and noting that the concentration, C_{NT}, is related to the volume fraction, ϕ, by $C_{NT} = \rho_{NT}\phi$ (ρ_{NT} is the nanotube density), gives the virial expansion for the osmotic pressure

$$\frac{\Pi}{C_{NT}} = RT\left[\frac{1}{\rho\overline{V}_{NT}} + \frac{(1/2-\chi)}{\overline{V}_S\rho^2}C_{NT} \right] \qquad (Y3)$$

The second virial coefficient is

$$B_2 = \frac{(1/2-\chi)}{\overline{V}_S\rho_{NT}^2} \qquad (Y4)$$

And $\rho_{NT}\overline{V}_{NT} = \overline{M}_{NT}$, the nanotube molecular weight.

Light Scattering[ξ]

The second virial coefficient is measured through its relationship to the intensity of elastically scattered light expressed via R_θ in the Debye Equation:

$$\frac{KC_{NT}}{R_\theta} = \frac{1}{M_w P_\theta} + 2B_2 C_{NT} \qquad (Z1)$$

In this equation, K is a combination of material constants; R_θ is the Rayleigh ratio (Eq Z2) - the ratio of the intensity of the light scattered from a volume V at a distance r from the collection lens; M_W is the weight-averaged molecular weight of the solute; $P(\theta)$ is an angle dependent scattering factor; and B_2 is the 2nd virial coefficient of the solute in the solvent. $P(\theta)$ is important in M_W determination for higher M_W polymers but is not needed in this work since we are only using the slope of the line and not the intercept.

$$R_\theta = \frac{Ir^2}{I_0 V} \qquad (Z2)$$

The Static Light Scattering (SLS) experiments were carried out with a photon counting SLS spectrometer of specific design. The device was mounted on a small optical table and consisted of a 2 mW, 543 nm HeNe laser, a translatable cuvette holder, focusing and collection lenses, and two green narrow bandpass filters. An uncooled EMI 891 PMT collected scattered light at 90 degrees. The PMT's output signal ran to an NIMBIN based photon counting system, which included an Ortec 113 Pre-amplifier, a Canberra 2015A

[ξ] Experiment carried out by PV Streich, JP Hamilton, *Department of Chemistry and Engineering Physics, University of Wisconsin, Platteville, Platteville, WI 53818, USA*

Amplifier and Pulse Shaper, and a Canberra 1481LA Pulse Discriminating Attenuator Rate Meter. The output voltage of the rate meter was connected to a Vernier Serial Box computer interface and collected in time using Vernier Logger Pro software.

Following initial alignment of the laser, cuvette, and collection optics, a sample of pure CCl_4 was used to optimize the scattering signal. During data analysis, digitisation noise of 1-2% was later found in the raw data and can be eliminated by rerunning the data at higher gain, but was found not to affect the linear correlations or the significant figures in our final calculations so the data was used as is.

The photon counting spectrometer directly generates a voltage proportional to I, the scattering intensity, and it was found convenient to plot $C/(S-S_0)$ vs. C, where S and S_0 are dimensionless numbers proportional to the solution and pure solvent scattering intensities, respectively[20].

$$\frac{C_{NT}}{S-S_0} = \frac{B_2}{K'}C_{NT} + \frac{1}{M_w K''} \tag{Z3}$$

The quantities K' and K" in equation Z3 are therefore instrumental constants unique to our SLS instrument and were obtained from calibrating the slopes and/or y-intercepts of plots of $C/(S-S_0)$ vs. C for the known molecular weight (M_w) standards and literature values for B_2 [23]. K' and K" were determined to be 1.0325^{11} and 9.0570^{11}, respectively, and determination of B_2's and χ's for known materials found in a polymer handbook[23] were uniformly within a few percent of the literature values. Once calibrated, from the slope of the $C/(S-S_0)$ vs. C plot, the second virial coefficient can be extracted.

All light scattering experiments were performed at lab temperature (circa 23 °C) and all instrument settings were calibrated or held constant throughout. Samples were prepared by sequential dilution and sonication steps and were interchanged by manual injection into a 1 mm path-length flow cell cuvette and run sequentially from low to high concentration. Following injection, the samples were allowed to equilibrate for approximately five minutes until turbulence from sample injection stopped and a 10 minute time average with a 40 second output time constant on the ratemeter used to photon count was used to determine the scattering intensities from the individual samples.

Stock solutions of nanotubes for light scattering measurements were prepared in NMP solvent and polystyrene calibration samples from polystyrene standards were made with Optima grade toluene used as purchased. In order to calibrate and qualify the instrument, narrow distribution polystyrene standards (150kD M_w/M_n=1.09, 100 kD M_w/M_n=1.07, and 1kD M_w/M_n= 1.05) for making calibration samples were purchased from Scientific Polymer Products, Inc. (Kit LOT #02, CAT# 542). NMP was obtained from

BASF Corp. and stored over 4 Ångstrom molecular sieves to maintain solvent dryness. Using a Mettler Toledo M100 analytical balance, SWNTs and polystyrene were massed to five significant figures and placed into sample vials to which solvents were added. The concentration range for SWNTs was to be below the general dispersion limit for nanotubes in NMP to avoid bundling and aggregates[2]. The concentration range for the polystyrene samples was chosen based on the approximate concentration range used in the literature to measure the B_2 for polystyrene[14] in toluene. All sample solvents were filtered with a Millipore Millex-FG 0.2 μm Hydrophobic PTFE filter before making the solutions to eliminate scattering sources like dust and other particulates. After adding the solvent, each nanotube sample was sonicated for 2 minutes with a VC 130PB Ultrasonic Probe Tip from Sonics and Materials Inc. and the polystyrene samples were sonicated for 20 minutes in a Fisher Scientific FS20H Ultrasonic Bath. Figures Z1 and Z2 are evidence that the SLS system performs as excepted and are representative of the calibrations used to extract the information used in this paper.
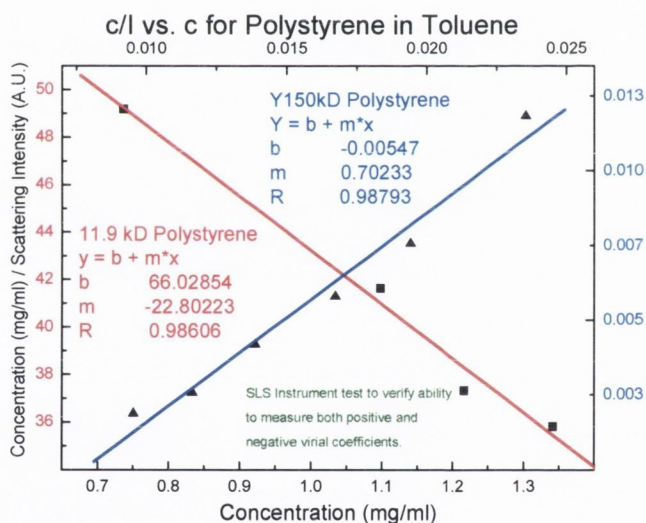
Figure Z1

Positive & Negative 2nd Virial Coefficient of two different polystyrenes in toluene. Used for instrument calibration for use with nanotubes in solvent and polymer systems and determination of K'.
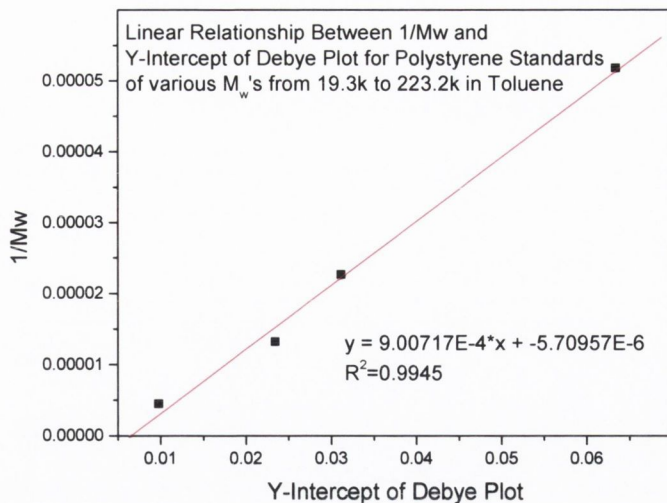
Figure Z2

Using polystyrene molecular weight standards, the SLS instrument used to determine the virial coefficient and hence, χ, was calibrated and checked for consistency by M_W determination used to verify the instrument constant, K". Linearity of the curve gives confidence in the instrument.

Sample	Slope of Debye Plot	Reported B2 (Polymer Handbook, Ref. 6)	Calcul ated K'	Calculated B2 Using average K' = 0.0010324	%er ror
150 kD Polystyrene in Benzene	0.37919	0.000395	0.0010 417	0.000391	- 0.89 %
100 kD Polystyrene in Toluene	-22.8022	-0.0237	0.0010 395	-0.02354	- 0.67 %
1 kD Polystyrene in Toluene	0.81198	0.000825	0.0010 16	0.000838	1.61 %
		Avg K'=	0.0010 324		

While it does not rule out systematic errors, with linear regression coefficients of better than 0.996, we can be confident in our extrapolations.

Table Z1

Internally consistent calibration of Debye Plots and Second Virial Coefficient data from literature[12], used to confirm and validate light scattering instrument function and calibration.

Nanotube density

Accurate estimation of the nanotube density is crucial for the calculation of χ. We can estimate the density associated with the carbon component from the nanotube mass divided by the excluded volume:

$$\rho_C = \frac{M_C}{V_C} = \frac{\pi DL(M/A)}{\pi(D+d)^2 L/4} = \frac{4D(M/A)}{(D+d)^2} \tag{Z4}$$

where D and L are the nanotube diameter and length, respectively. The van der Waals distance is represented by d while the mass per unit area associated with the graphitic sidewall is represented by M/A.

However this expression needs to be corrected for the presence of residual iron to give the true density, ρ:

$$\rho = \frac{4D(M/A)}{(D+d)^2} \frac{(m_{Fe}+m_C)/m_C}{(V_{Fe}+V_C)/V_C} = \frac{4D(M/A)}{(D+d)^2} \frac{(1+m_{Fe}/m_C)}{(1+\rho_C m_{Fe}/\rho_{Fe}m_C)} \tag{Z5}$$

where m, V and ρ represent mass, volume and density and the subscripts Fe and C represent iron and carbon, respectively. M/A can be found either from the density of graphite or from theory to be 7.7×10^{-7} kg/m^2. Thermogravimetric analysis gives a value of $m_{Fe}/m_C = 0.08$ for the nanotubes used in this work. This leads to a density of ~1830 kg/m^3 for nanotubes of diameter 1nm, in the mid range of the nanotubes used here.

5.6 References

1.   Submitted to NanoLetters.
2.   Giordani, S. et al. Debundling of single-walled nanotubes by dilution: Observation of large populations of individual nanotubes in amide solvent dispersions. Journal of Physical Chemistry B 110, 15708-15718 (2006).
3.   Zhang, S. J., Kinloch, I. A. & Windle, A. H. Mesogenicity drives fractionation in lyotropic aqueous suspensions of multiwall carbon nanotubes. Nano Letters 6, 568-572 (2006).
4.   Liu, J. et al. Controlled deposition of individual single-walled carbon nanotubes on chemically functionalized templates. Chemical Physics Letters 303, 125-129 (1999).
5.   Furtado, C. A. et al. Debundling and dissolution of single-walled carbon nanotubes in amide solvents. Journal of the American Chemical Society 126, 6095-6105 (2004).
6.   Landi, B. J., Ruf, H. J., Worman, J. J. & Raffaelle, R. P. Effects of alkyl amide solvents on the dispersion of single-wall carbon nanotubes. Journal of Physical Chemistry B 108, 17089-17095 (2004).
7.   Moore, V. C. et al. Individually suspended single-walled carbon nanotubes in various surfactants. Nano Letters 3, 1379-1382 (2003).
8.   Everett, D. H. Basic Principles of Colloid Science. (Royal Society of Chemistry Paperbacks).
9.   Bachilo, S. M. et al. Structure-assigned optical spectra of single-walled carbon nanotubes. Science 298, 2361-2366 (2002).
10.   Flory, P. J. Statistical Thermodynamics of Semi-Flexible Chain Molecules. Proceedings of the Royal Society of London Series a-Mathematical and Physical Sciences 234, 60-73 (1956).
11.   Ciferri, A. Liquid Crystallinity in Polymers (Wiley, New York, 1991).
12.   Hildebrand, J. H., Prausnitz, J. M. & Scott, R. L. Regular and related solutions (Van Nostrand Reinhold Company, New York, 1970).
13.   Lyklema, J. The surface tension of pure liquids - Thermodynamic components and corresponding states. Colloids and Surfaces a-Physicochemical and Engineering Aspects 156, 413-421 (1999).
14.   Tsierkezos, N. G. & Filippou, A. C. Thermodynamic investigation of N,N-dimethylformamide/toluene binary mixtures in the temperature range from 278.15 to 293.15 K. Journal of Chemical Thermodynamics 38, 952-961 (2006).
15.   Benedict, L. X. et al. Microscopic determination of the interlayer binding energy in graphite. Chemical Physics Letters 286, 490-496 (1998).

16. Girifalco, L. A. & Lad, R. A. Energy of Cohesion, Compressibility, and the Potential Energy Functions of the Graphite System. Journal of Chemical Physics 25, 693-697 (1956).

17. Hodak, M. & Girifalco, L. A. Fullerenes inside carbon nanotubes and multi-walled carbon nanotubes: optimum and maximum sizes. Chemical Physics Letters 350, 405-411 (2001).

18. Zacharia, R., Ulbricht, H. & Hertel, T. Interlayer cohesive energy of graphite from thermal desorption of polyaromatic hydrocarbons. Physical Review B 69 (2004).

19. Rubinstein, M. & Colby, R. H. Polymer Physics (Oxford University Press, Oxford, 2003).

20. Sperling, L. H. Introduction to Physical Polymer Science (John Wiley and Sons, New York, 1992).

21. Debye, P. Journal of Physical Chemistry 51, 18 (1946).

22. Flory, P. J. Principles of Polymer Chemistry (Cornell University Press, 1953).

23. Brandrup, J., Immergut, E. H., Grulke, E. A., Akihiro, A. & Bloch, D. R. Polymer Handbook (1999).

24. Albrecht, P. M. & Lyding, J. W. Ultrahigh-vacuum scanning tunneling microscopy and spectroscopy of single-walled carbon nanotubes on hydrogen-passivated Si(100) surfaces. Applied Physics Letters 83, 5029-5031 (2003).

25. Bozso, F. & Avouris, P. Reaction of Si(100) with Nh3 - Rate-Limiting Steps and Reactivity Enhancement Via Electronic Excitation. Physical Review Letters 57, 1185-1188 (1986).

26. Grujicic, M., Cao, G. & Roy, W. N. Atomistic simulations of the solubilization of single-walled carbon nanotubes in toluene. Journal of Materials Science 39, 2315-2325 (2004).

27. Girifalco, L. A. & Good, R. J. A Theory for the Estimation of Surface and Interfacial Energies .1. Derivation and Application to Interfacial Tension. Journal of Physical Chemistry 61, 904-909 (1957).

Chapter 6

Exfoliation in Ecstasy: Liquid Crystal Formation and Chirality Dependent Debundling Observed for Single Walled Nanotubes Dispersed in the Liquid Drug γ-Butyrolactone[1]

6.1 Introduction

This chapter will present results on the dispersion of SWNTs in γ-Butyrolactone. This liquid, sometimes referred to as "liquid ecstasy", is well known for its narcotic properties. At high concentrations the dispersions form an anisotropic, liquid crystalline phase which can be removed by mild centrifugation. At lower concentrations an isotropic phase is observed with a biphasic region at intermediate concentrations. The nature of these phases is discussed in this chapter, outlining vital advantages and limitations for the implementation of SWNTs into composites.

6.2 Background

Now that a small number of solvents, capable of dispersing SWNTs, have been discovered, it is imperative to rapidly expand this cohort to discover as many good solvents for nanotubes as possible. The expansion of the number of such solvents is necessary to allow a much greater choice to experimenters who may require certain solvents with certain properties under certain circumstances. One of the most promising of these solvents is γ-Butyrolactone (GBL). This solvent is a pro-drug (in-vivo precursor) of the drug γ-hydroxybutric acid (GHB)[2, 3], but is also a potent narcotic in its own right. Both GBL and GBH are sometimes known as "liquid ecstasy"[4]. While GHB has received a great deal of

101

attention in recent years as it is a drug of abuse, GBL is more lipid soluble than GHB and is said to be more potent.

Carbon nanotubes can be thought of as exceptionally stiff polymeric molecules[5], and thus like other rigid chain polymers, such as tobacco mosaic virus[6], should form a lyotropic liquid crystalline phase in a suspension above a critical concentration[7]. Based on this, Windle showed experimental evidence of liquid crystallinity of multiwalled carbon nanotubes in an aqueous suspension[8], with a following paper from Rice reporting the liquid crystalline behaviour of SWNTs in a superacid suspension[9]. The ability of a rod-like object to form a liquid crystalline phase – its mesogenicity, depends on its straightness and aspect ratio. For a lyotropic system, the greater the mesogenicity of the rods, the lower the volume fraction required to form a liquid crystalline phase. Figure 6.1 shows a typical polymer/solvent phase diagram showing the liquid crystalline and isotropic phases to be separated by a biphasic region (labelled as the so called Flory Chimney)[10]. This chimney extends over a fixed range of compositions, the bounds of which are dependent on the mesogenicity and strength of the rod-rod interaction divided by temperature.
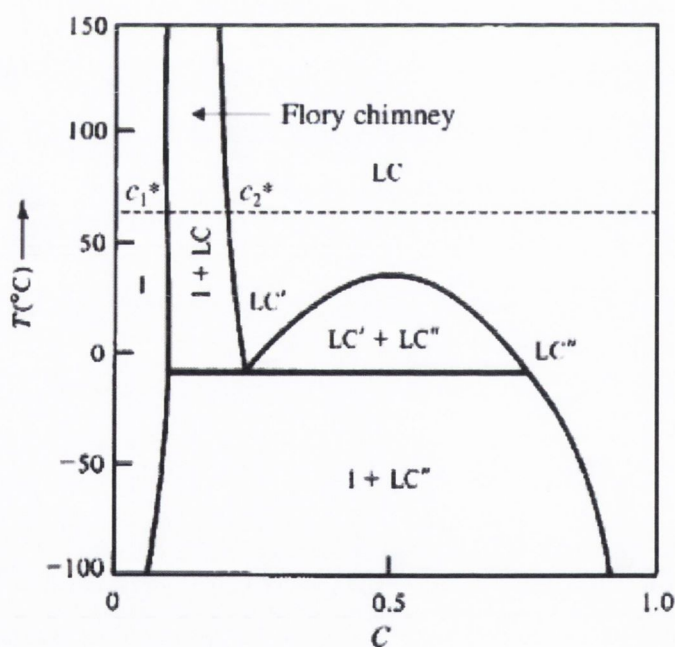

Figure 6.1

The phase diagram for a lyotropic liquid crystalline material in a solvent. The Flory Chimney contains the biphasic region, with the critical concentrations for the lower and upper limits of the chimney marked as c_1* and c_2* respectively.

Windle has recently described a method for separating nanotubes on the basis of their mesogenicity by fractionating biphasic aqueous suspensions within the Flory Chimney of the lyotropic phase diagram. Separation was facilitated by centrifuging the biphasic nanotube suspension.

In this work we use crossed polarised microscopy, atomic force microscopy, UV-vis-NIR absorption and Raman spectroscopy to show that single-walled nanotubes can be dispersed effectively in GBL. These dispersions exhibit liquid crystalline behaviour, allowing us to separate the anisotropic phase from the isotropic phase by centrifugation. The SWNT can be debundled simply by reducing the isotropic nanotube concentration in GBL dispersions. We find that the average bundle diameter decreases with decreasing concentration before saturating at approximately 2.4 nm below a concentration of $\sim 10^{-2}$ mg/mL. In addition a population of individual nanotubes is present at all concentrations. While we attempted to use infra red photoluminescence measurements as an in-situ probe to confirm the AFM measurements, no PL was observed for any concentration. We believe that the strong nanotube-solvent interaction is responsible for efficient photoluminescence quenching in these systems.

6.3 Experimental Procedure

For this study, purified single-walled carbon nanotubes (HiPCO) were purchased from Carbon Nanotechnologies, Inc., (www.cnanotech.com, Lot number: P0288) and used as supplied. Thermogravimetric studies confirmed the residual iron content to be ~6wt%. Microscopy studies showed no evidence of non-nanotube carbon. γ-Butyrolactone (GBL) (Product number: B103608-500ML, Batch number: 029H07091) was purchased from Aldrich and also used as supplied. The molecular structure of GBL is shown as an inset in figure 6.2. SWNT dispersions in GBL were prepared as follows. A high concentration stock dispersion of SWNT in GBL was prepared at a concentration of 0.5mg/mL. This dispersion was subjected to 2 minutes high power sonication, using an ultrasonic tip processor (Model GEX600; 120W, 60kHz). Subsequently, a range of dispersions was prepared by successive dilution (concentration range: $0.5\text{-}6 \times 10^{-4}$ mg/ml), each subjected to 2 minutes sonication prior to further dilution. All dispersions were then mildly sonicated using a low-power ultrasonic bath (Model Ney Ultrasonic) for 4 hours followed by a further 1 minute high power sonication. In all cases this resulted in a very uniform "black" dispersion with varying degrees of darkness, depending on the concentration. However, for the higher concentrations, large aggregates were also observed. These large aggregates

were removed from these dispersions by mild centrifugation (CF) (6000 rpm, ~ 3000g, for a period of 90 mins).

Removal of aggregates by CF, results in two phases, the sediment and supernatant, which can be separated by decantation. To quantify the relative amounts of each phase, UV-Vis absorbance measurements of each dispersion were carried out before and after CF. The concentration of the dispersions prior to CF is referred to as C_i, while the true concentration of the supernatant after CF and decantation is refered to as C_{NT}. Sonication is known to damage nanotubes under certain circumstances. In order to probe the level of damage to the SWNTs due to sonication, Raman spectroscopy was employed to compare the raw HiPCO powder with the sediment and supernatant separated after CF. To facilitate this, the sediment and supernatant were dried on a filter paper using a Buchner funnel allowing comparable, solid phase measurements to be made for all three samples. The normalised spectra, as shown in figure 6.2, were virtually identical, no observable damage to the SWNTs after sonication indicating minimal chemical modification to the nanotubes during sample preparation.
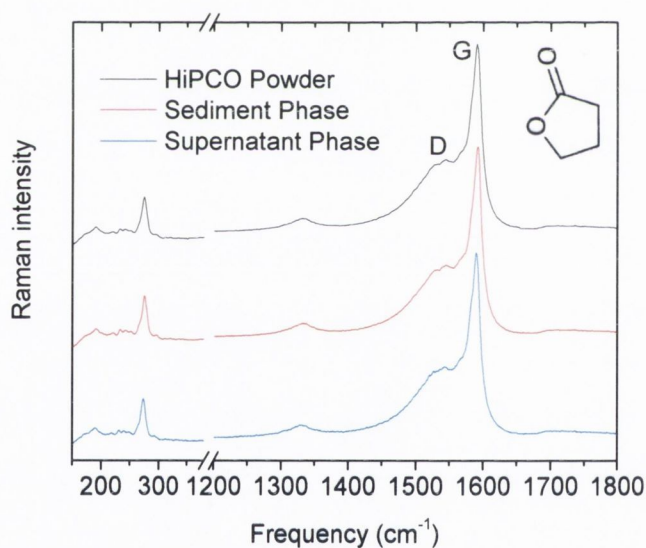

Figure 6.2

Raman spectra of the raw HiPCO SWNT powder, the sedimented phase, and the supernatant phase. The laser excitation wavelength used was 532nm. Also shown is the molecular structure for γ-Butyrolactone.

The biphasic nature of SWNTs dispersions was investigated, before and after CF using a cross-polarised microscope used in transmission mode (Leica Microscope fitted

with JVC colour video camera). The samples were prepared by dropping the dispersion on a glass slide and covering it with a cover-slip. The structure of the sedimented phase was investigated using scanning electron microscopy.

The stability of the supernatant phase was investigated, after CF, by monitoring the optical transmission of a high concentration dispersion, C=0.032mg/mL, over a period of 55 days. It should be pointed out that GBL is very hygroscopic. Exposure to moisture rapidly destabilised the dispersions. As such efforts were made to avoid exposure to water, however it was not found necessary to store the dispersions under inert gas.

To investigate possible time dependent aggregation, a small volume of each supernatant was drop-cast onto cleaned silicon substrates for AFM measurements. Samples were placed in a vacuum oven at 80C for a period of 4 hours to allow solvent to evaporate. To test the reversibility of the dilution process, one of the low concentration dispersions, $C_i=5\times10^{-3}$ mg/mL, that had been made using the procedure described above, was allowed to evaporate in a controlled manner, thus increasing the SWNT concentration. Similarly, AFM samples were prepared at set intervals throughout the evaporation process.

Raman measurements were made on a Jobin Yvon Raman system, fitted with with a HeNe 20 mW laser (λ = 532nm). SEM images were taken using a Hitachi S-4300 (operated with an acceleration of 25kV). UV-Vis absorbance measurements were carried out using a Cary 6000i. Centrifugation was carried out using a Hettich EBA-12 centrifuge. Tapping mode atomic force microscopy (AFM) was carried out on all these samples, using a Multimode Nanoscope IIIA. Pointprobe silicon nitride cantilevers (force constant = 42 Nm^{-1}, resonant frequency = 330kHz) were used for all measurements. High-resolution transmission electron microscopy (HR TEM) measurements were carried out using an FEI Tecnai F20 operated at 200kV[†]. Samples were prepared by placing a small drop of the dispersion on holey carbon grids (mesh size 400).

6.4 Results

Liquid Crystal Formation

Absorption spectra, taken before CF are shown in figure 6.3. These spectra show features typical for dispersions of SWNT. Spectra taken after CF were similar in spectral profile. In order to quantify its concentration dependence, the absorbance measured both

---

[†] HRTEM measurements carried out by Dr. Valeria Nicolosi, Sch. of Physics, TCD

before and after CF (λ=660nm) has been plotted as A/l versus nanotube concentration in figure 6.4A (l is the cell length). Before centrifugation, the absorbance of the dispersions behaves, at low concentration, according to the Beer-Lambert law: $A = \alpha C_i l$, where α is the extinction co-efficient and C_i is the concentration in mg/ml. Taking the slope of this curve at low concentration, we find the absorption coefficient, α_{660nm}, to be 3426 mL mg^{-1}m^{-1}. This value compares favourably with the reported values of 3264 mLmg^{-1}m^{-1} for SWNTs dispersed in N-methyl-pyrrolidone (NMP)[11] and values of α_{700nm} in the range 3000–3470 mLmg^{-1}m^{-1} for various other amide solvents[12]. The data in figure 6.4A was then divided by initial concentration to show weak variation of α_{660nm} with concentration (figure 6.4B), probably due to the presence of aggregates at high concentration. At high concentrations, α_{660nm} is relatively low (~2400 mLmg^{-1}m^{-1}). As the dispersions become isotropic (see below), α_{660nm} increases, approaching values of ~3700 mLmg^{-1}m^{-1} at low concentration. This value is expected to reflect the true extinction coefficient for dispersed nanotubes.
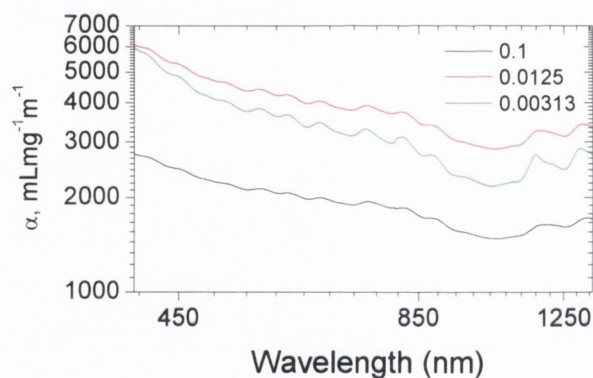
Figure 6.3

Absorbance spectra taken before centrifugation. The extinction coefficient, α, is plotted against wavelength for the three concentrations, C_i, marked in the figure.

The absorbance of the supernatants after CF did not scale linearly with concentration as aggregated material had been removed at each concentration by centrifugation. The mass fraction of nanotube material removed by centrifugation, χ_{Agg}, can be described [11], by

$$\chi_{Agg} = \frac{A_{660,Intial} - A_{660,Final}}{A_{660,Intial}} \tag{6.1}$$

This has been calculated and is shown in figure 6.4C. At high concentration, the fraction of material removed by centrifugation approaches one, but falls off gradually to close to zero for the low concentration samples. Visual inspection confirmed that CF had removed the aggregates described previously. The fact that $\chi_{Agg} \approx 0$ at low concentration would suggests that good dispersions can be obtained at low concentration. However, this does not explain why we get a phase separation at high concentration into two phases.
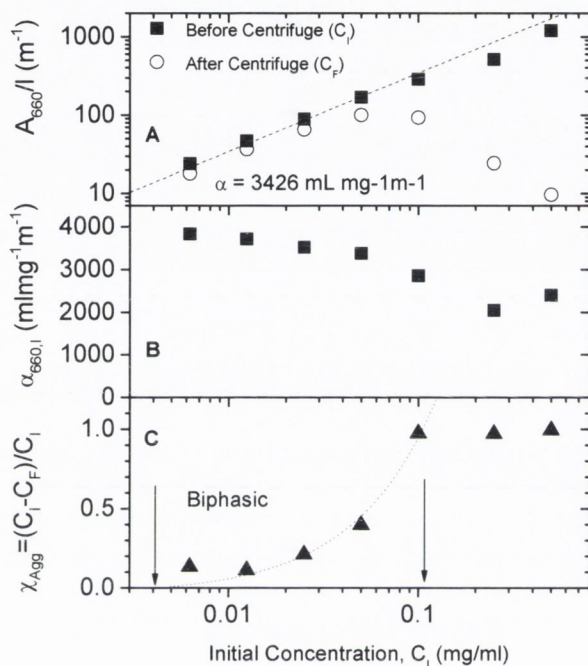
Figure 6.4

(A) Absorbance per unit length, A/l, (at $\lambda = 660nm$) measured before and after centrifugation. The extinction coefficient shown was calculated from the slope of the low concentration before-centrifuge data (dashed line). (B) Absorption coefficient before centrifuge. (C) Fraction of SWNTs that are found to exist as large aggregates, as a function of the initial concentration. The dashed line represents a linear fit for the data in the biphasic region (delineated by the arrows) that can be described by equation (6.2).

Windle et al.[8, 13] have recently shown that functionalised nanotubes form an anisotropic, lyotropic liquid crystalline phase in a suspension or solution above a critical concentration, C_2. In addition, an isotropic phase exists where the bundles of nanotubes are randomly orientated below another critical concentration, C_1. The relevant nanotube/solvent equilibrium diagram shows these phases to be separated by a biphasic region, classified as the 'Flory-Chimney'[10]. Within this biphasic region, both isotropic and

anisotropic regions co-exist with the relative amounts of each dependent on the concentration. Windle et al have also shown that the anisotropic phase can be removed by centrifugation[14]. We suggest that the aggregates observed in our high concentration dispersions, and subsequently removed by centrifugation, correspond to an anisotropic liquid crystalline phase. Thus, χ_{Agg} corresponds to the fraction of anisotropic phase in the biphasic region. Figure 6.4C, then outlines how our system moves through these phases. Low concentrations, where χ_{Agg} is effectively zero, correspond to the isotropic phase and high concentrations, where χ_{Agg} is ≈ 1, correspond to the anisotropic phase. In between we have the biphasic region. In general, the concentration dependence of χ_{Agg} in the biphasic region is given by the Lever rule[14]:

$$\chi_{Agg} = \frac{(C_i - C_1)}{(C_2 - C_1)} \tag{6.2}$$

Fitting equation (6.2) to the data in figure 6.4C, C_1 and C_2 were found to be ~0.004 and 0.105 mg/mL respectively. The lower value can be considered the dispersion limit of SWNTs in γ-Butyrolactone; i.e. the maximum concentration below which nanotube bundles exist in an isotropic phase. Onsager predicts that the rod-solvent system forms an anisotropic liquid-crystalline phase at a concentration of $C_2 \approx 3.3 \rho d / l$, where ρ is the mass density and d/l is the rod aspect ratio[15]. Applying this to the measured value of C_2 gives a value of l/d~50,000. This is far too high for the dimensions of the bundles or indeed the nanotubes used in this study (see below). This means that our measured C_2 value lies far below the theoretical value for athermal (zero enthalpy of mixing) solutions. This strongly suggests that the dispersions studied here, un-surprisingly have a positive enthalpy of mixing[10].

The association of the aggregates with the anisotropic liquid crystalline phase suggests that the aggregates must consist of aligned nanotubes. This alignment was examined by crossed polarised microscopy for a range of concentrations before and after CF. Any anisotropic features will appear bright whereas isotropic features will remain dark. Shown in figure 6.5 are crossed polarised microscope images for three of the dispersions before and after CF (C_i = 0.5mg/mL, 0.1 mg/mL and 0.05mg/mL). In all cases, bright regions are observed, indicating the presence of an aligned phase. For the highest concentration, much of the image is bright. While this sample has concentration greater than C_2, and hence should be all bright, some of the sample remained dark due to light absorption by the high concentration dispersion. The coverage of the bright areas falls off as the SWNT concentration decreases. This concurs with the fall in χ_{Agg} with

concentration. Sample images before CF for samples with concentrations $< C_1$ appeared completely black, indicating no aligned aggregates. The corresponding supernatants were also examined after centrifugation as shown in the right hand panels of figure 6.5. After CF, the coverage of bright regions fell dramatically, indicating that the supernatants were comprised almost entirely of isotropically dispersed carbon nanotube bundles.
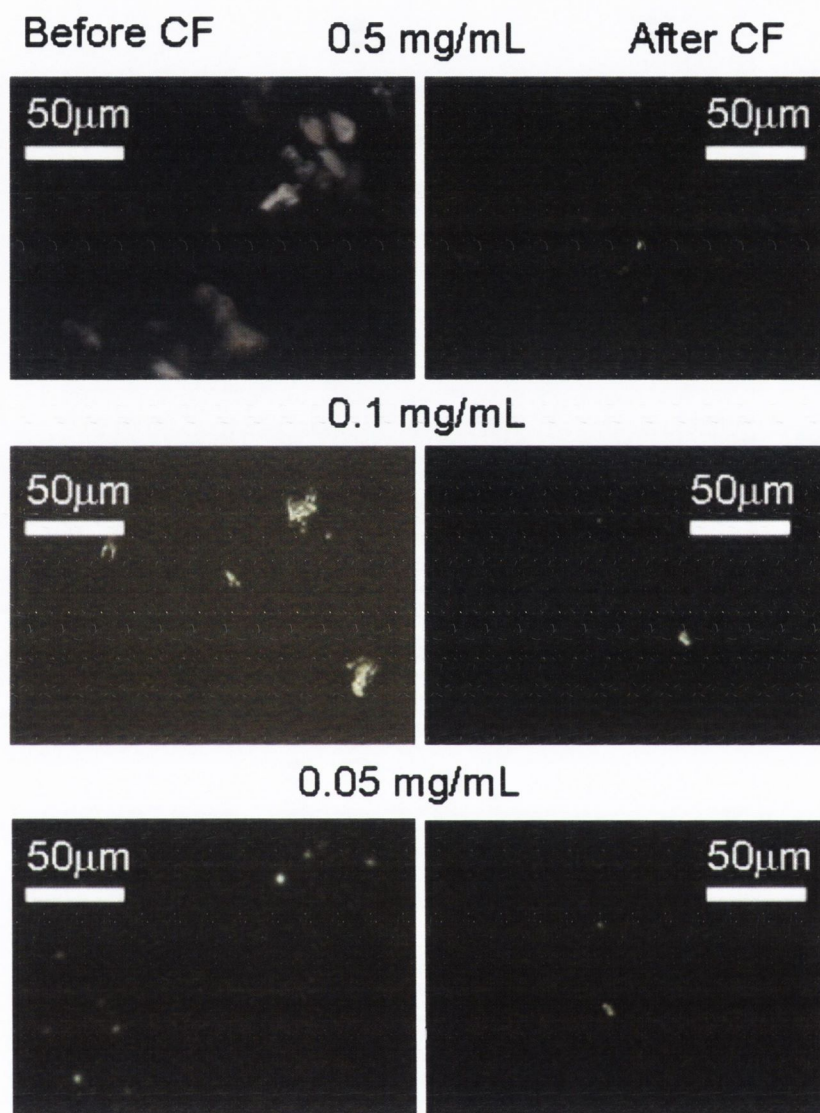

Figure 6.5

Cross-Polarised Microscopy of γ-Butyrolactone/SWNT dispersions before and after centrifugation. The presence of bright anisotropically aligned bundles is shown to scale with concentration before centrifugation. In all cases, the coverage of bright regions dramatically decreases after centrifugation.

SEM of the sedimented phase, separated after centrifugation, shown in figure 6.6, shows highly aligned structures, clearly evidencing an anisotropic phase. The inset in the bottom left shows a magnified view of one of these structures showing an array of aligned bundles each of order of 100 nm in diameter (including gold coating for SEM).
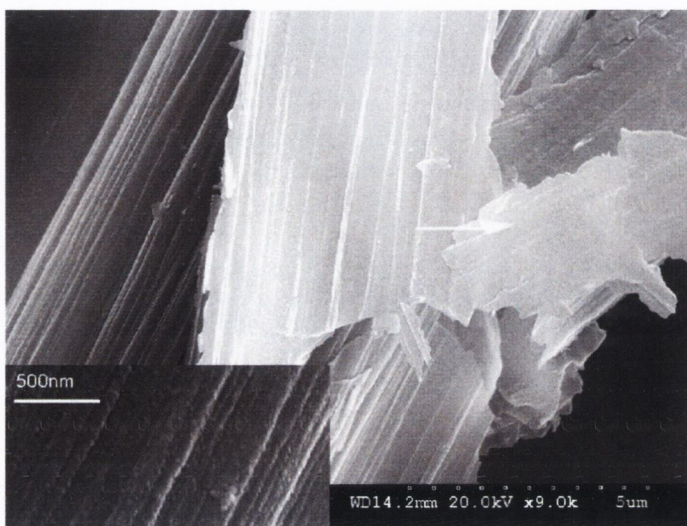
Figure 6.6

SEM of SWNT sedimented phase, showing the presence of anisotropically aligned bundles. Shown in the bottom left corner is a magnified region showing aligned (gold coated) bundles with diameters of order 100nm.

While nematic liquid crystalline phases have been observed previously in nanotube dispersions by Windle, Pasquali and others[8, 9, 13, 14, 16, 17], all of these results were for relatively complex dispersions. In general, these observations have been made for three phase dispersions where nanotubes have been dispersed in a solvent with the aid of a dispersant, i.e. a surfactant[16], an acid[9] or DNA[17]. Alternatively, in a number of cases the nanotubes have been oxidized to introduce polar surface groups to aid interaction with a polar solvent[8, 13, 14]. We believe that this is the first example of liquid crystallinity in a simple, two phase system of nominally pristine nanotubes dispersed in a solvent.

The Isotropic Phase: Stability

A dispersion consisting solely of the isotropic phase of nanotubes can be prepared by removal of the anisotropic phase by mild centrifugation followed by decantation. Using the measured mass fraction, χ_{Agg}, the true concentration of the supernatants was calculated as $C_{NT} = C_i(1-\chi_{Agg})$. The stability of the isotropic phase with time was investigated by taking a high-concentration, C_{NT} = 0.032mg/mL, isotropic-phase dispersion and monitoring transmission through it over a period of 55 days. Absorbance (at 650nm) through the sample as a function of time was monitored using an in-house-built apparatus [18]. As illustrated in figure 6.7A, the absorbance was shown to remain stable over this timeframe, showing that subsequent sedimentation did not occur. Furthermore, a drop of the dispersion for AFM analysis was taken immediately after CF and again after 55 days. AFM images showed a high population of 1-dimensional objects, typically microns long and with heights of a few nanometers. As HiPCO SWNTs nanotubes typically have diameters in the range 0.7 –1.4nm, the majority of objects observed are bundles of nanotubes. By measuring the height profile of many of these objects, statistical analysis of the nanotube bundle diameter can be carried out. The bundle diameter distribution of the sample prepared immediately after CF is shown, in figure 6.7, to be statistically indistinguishable to that of the sample prepared 55 days after centrifugation. This shows that no aggregation, or indeed exfoliation occurs after CF.
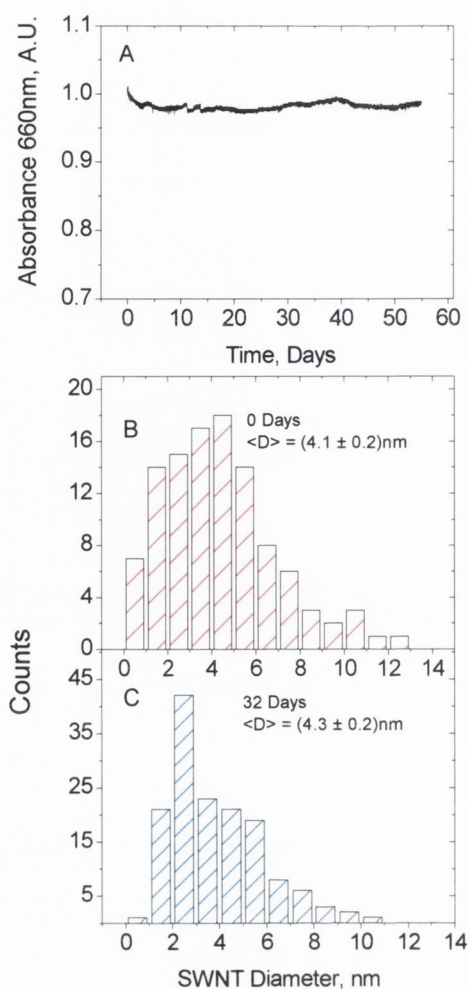
Figure 6.7

(A) Absorbance (at 650nm) of a γ-Butyrolactone/SWNT dispersion (C_{NT} = 0.032 mg/mL demonstrating stability over a period of 55 days. (B) & (C) AFM diameter distributions of bundle heights at 0 days and 55 days respectively. Statistical analysis shows the diameter distributions to be indistinguishable.

The Isotropic Phase: Bundle Diameter distributions

In order to fully understand the dispersive effect of GBL on SWNTs, AFM studies were made on each of the supernatants. Figures 6.8A and 6.8B show AFM images of a high (C = 0.03mg/mL) and low (5.8×10^{-4} mg/mL) concentration dispersions. Corresponding height profiles (for the black lines in each image) are shown in figures 6.8C and 6.8D. A high coverage of 1-D objects is evident in both images. However, the objects observed at high concentration have much larger heights compared to the objects at low concentrations. In fact, many of the objects observed at low concentration have heights of ~1nm, commensurate with individual nanotubes as observed previously for NMP based dispersions[11].
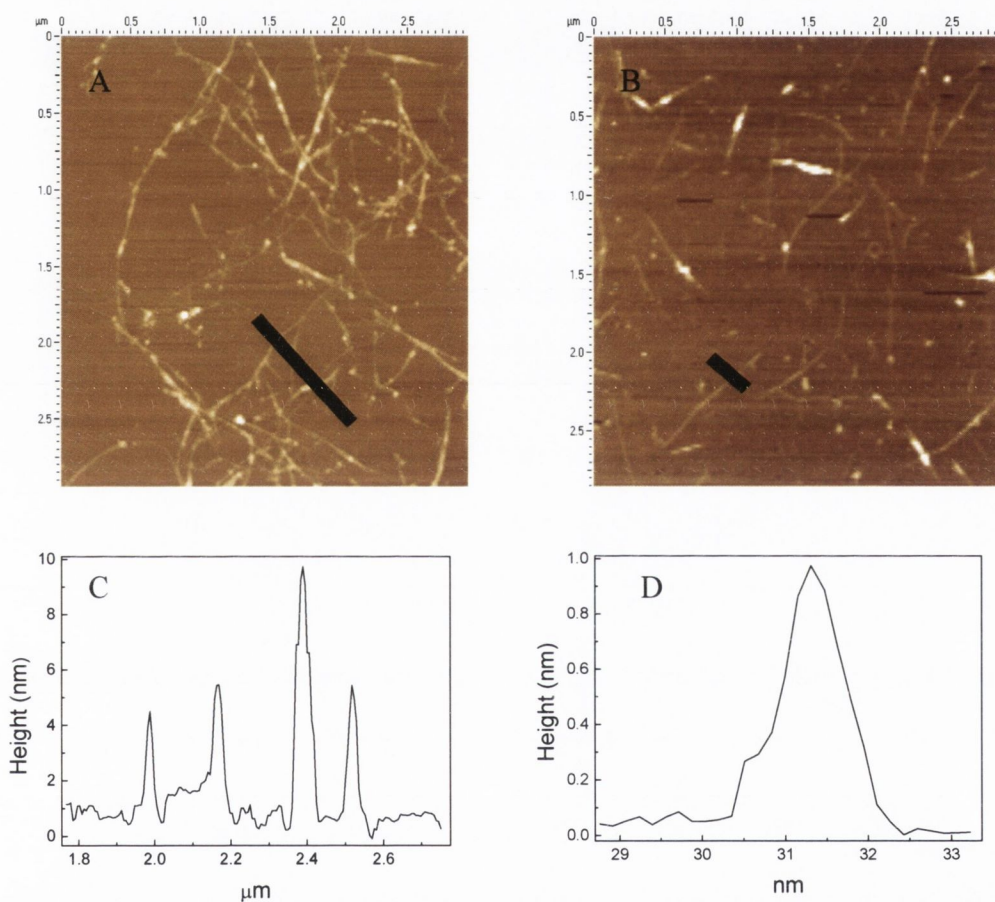
Figure 6.8

AFM images of SWNT dispersions at concentrations of (A) 0.03mg/mL and (B) 6×10^{-4} mg/mL. Their corresponding cross-sections are shown in (C) and (D) respectively. These images are representative of the entire dispersion set.

To investigate this further, statistical analysis was carried on the AFM images for all concentrations. A large set of bundle heights (approximately 150) was accumulated, from random positions on each sample. It should be noted that measurements were not

made near bundle-bundle junctions to avoid artificially high results. Shown in figure 6.9 are the resulting bundle diameter distributions as a function of concentration. As the nanotube concentration falls, the distribution is clearly shifted to bundles of small diameters as has been observed previously for SWNT in NMP[11], SWNT in DNA/H$_2$0 dispersions[19] and nanowires in various organic solvents[18, 20].
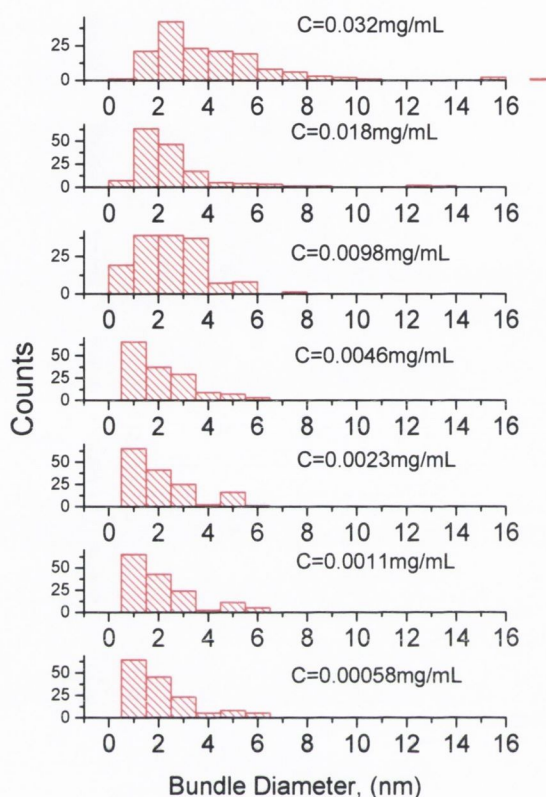
Figure 6.9

Histograms of bundle diameters for SWNTs dispersed in γ-Butyrolactone. The concentration of each dispersion examined is also shown. Approximately 150 bundle heights per concentration were measured.

Plotting the root-mean-square of the bundle diameter, ($D_{rms} = \sqrt{<D^2>}$), against SWNT concentration on a log-log plot, as shown in figure 6.10, clearly demonstrates the decrease in bundle diameter with decreasing SWNT concentration. Root mean square bundle diameters are seen to decrease linearly with concentration, from D$_{rms}$=4.8nm at C=0.03mg/mL, until C=0.005mg/mL where the diameter levels off at D$_{rms}$≈2.4nm. To illustrate the reversibility of this process, an existing low concentration dispersion, C = 0.006mg/mL was allowed to evaporate in a graduated container. At pre-selected points during the evaporation, drops were taken from the dispersion and samples for AFM

analysis were made. Figure 6.10 shows that as the SWNT concentration rose, the measured RMS bundle diameter increases, following the same trend as the initial diluted dispersions.
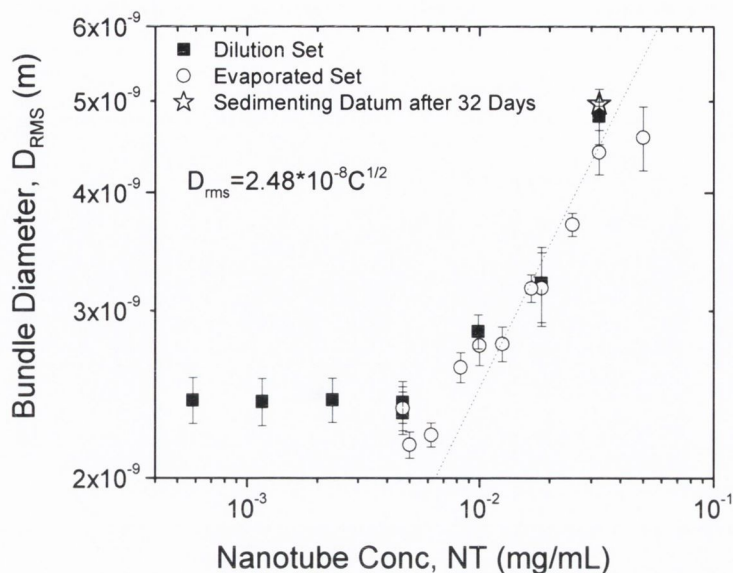
Figure 6.10

SWNT bundle diameter as a function of SWNT concentration. The black squares represent the initial dilution based dispersions. The data saturates at low concentrations, with a mean bundle diameter of 2.4nm. The circles represent the evaporation data, where a dispersion, $C_{NT}= 0.006$mg/mL, was allowed to evaporate and the bundle diameter monitored with rising concentration. The star datum represents a sample, C= 0.032mg/mL, allowed to stand for 55 days. The dashed line corresponds to a fit of equation (6.3) to the dilution data. The fit parameters are given in the figure.

The fact that that D_{rms} follows the same curve for both dilution and evaporation strongly suggests that a concentration dependent equilibrium exists. It is interesting that we should reach the same equilibrium, diluting with sonication as we reach during a slow evaporation. This suggests that the main role of sonication is to affect the kinetics of the debundling process. That this equilibrium is stable can be shown by the invariance of the diameter distribution over the course of 55 days after preparation (figure 6.7). The measured D_{rms} falls perfectly on the equilibrium curve as shown in figure 6.10, indicating that rebundling did not occur over this time period. This suggests that the bundle diameter reached for each concentration has reached equilibrium and that only varying the concentration of SWNTs will affect the bundle diameter.

The average length of all bundles (including individual SWNT) observed in the AFM was found to be $L_{Bun}=(2.2\pm1.3)$ μm while the average length of all individual

nanotubes (i.e. those with diameters less than 1.4nm) was found to be L_{Ind} = (0.9±0.4) μm. The difference between these numbers is somewhat surprising. Measurements in SWNT/NMP dispersions show that bundle and individual nanotube lengths were identical within error, suggesting inter-nanotube sliding to maximise their binding energy[11]. This has also been observed for bundles of inorganic nanowires.[18] That we do not observe this to occur for the GBL based dispersions suggests that, for some reason, the nanotubes may be somewhat impeded from relative motion.

It has previously been suggested that the equilibrium discussed above can be quantified in terms of an equilibrium bundle number density[11, 20]. As shown in the previous chapter, this leads to an expression for the concentration dependence of the root mean square bundle diameter

$$D_{RMS} = \sqrt{<D^2>} \approx \left[\frac{4C_{NT}}{\rho_{NT} \pi L_{Bun} (N/V)_{eqm}} \right]^{1/2} \qquad (6.3)$$

where ρ_{NT} is the nanotube density, L_{Bun} is the mean bundle length (approximated as concentration independent) and $(N/V)_{eqm}$ is the equilibrium bundle number density. This equation has been fitted to the data set in figure 6.10. Using this fit and the measured values of L_{Bun}, from AFM, a value for $(N/V)_{eqm}$ was found to be (6.0±4.5)×10^{17} m^{-3}. Inverting this term, gives the equilibrium solvent volume per bundle to be V_{Sol}^{Eqm} (1.97±1.25)×10^{-18} m^3. This value compares to that for NMP, where $V_{Sol}^{Eqm-NMP}$=(6.7±2.7) ×10^{-19}m^3. One explanation of the difference between these two numbers is that GBL is not as effective a dispersant of SWNTs as NMP[11]. Thus a larger volume of GBL is required to disperse each bundle at equilibrium when compared with the volume of NMP needed. It should also be noted that the average saturated bundle diameter at low concentrations for GBL (2.4nm) is slightly higher than that for NMP (1.9nm) again suggesting that NMP is a better dispersant[11].

The Isotropic Phase: Population of Individual Nanotubes

HiPCO nanotubes generally have a diameter range of 0.7<D<1.4nm. Thus, objects observed by the AFM with heights of less than 1.4nm can be classified as individual nanotubes. It should be noted that a population of individual nanotubes was seen to be present at all concentrations investigated. Shown in figure 6.11 is a HR-TEM image, typical of a low concentration (C =0.002 mg/mL) dispersion. Large numbers of individual nanotubes are observed in the HRTEM images.
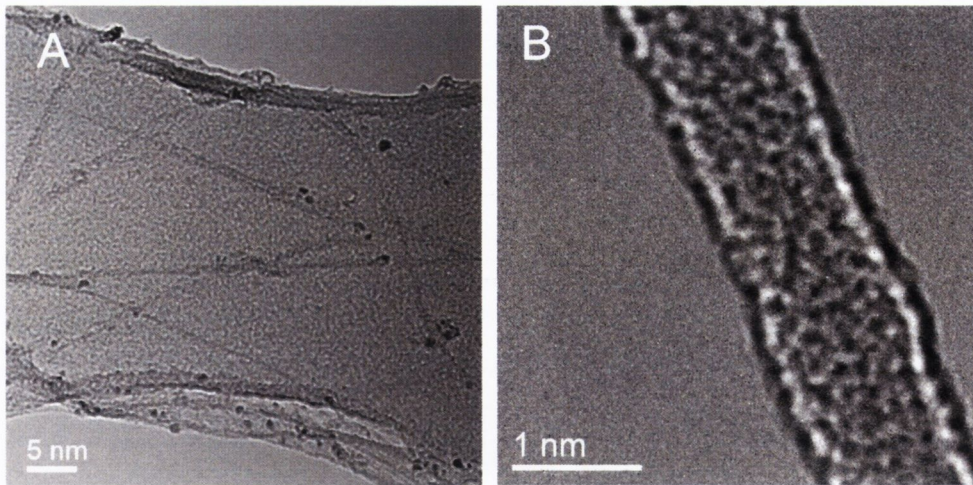
Figure 6.11

High Resolution-Transmission Electron Microscopy image of A) individual SWNT and small bundles (C=0.002mg/mL) and B) an individual SWNT.

Using the criterion above, we can deduce the number-fraction of individual nanotubes, N_{Ind}/N_T, for each concentration from the AFM data. Figure 6.12A shows that at higher concentrations (C=0.032mg/mL) only 7% of objects counted could be classified as individual nanotubes. However, N_{Ind}/N_T increases steadily with decreasing concentration saturating at 38% at C=0.005mg/mL. The behaviour of the evaporated data set matches that of the diluted data set, further evidence of the concentration dependence of bundle size. This number fraction of individual nanotubes at lower concentrations, for GBL is not as high as that for NMP at a similar concentration (C=0.004mg/mL), which corresponded to ~70% individual nanotubes. In the absence of concentration dependent aggregation, the percentage of individual nanotubes would remain constant at all concentrations. Thus, deviation from the dashed line in figure 6.12A illustrates where the onset of bundling occurs.

The number fraction of individual tubes can be used to generate the absolute number of individual nanotubes per unit volume of solvent using[11]

$$\frac{N_{Ind}}{V} = \frac{N_{Ind}}{N_T}\frac{N_T}{V} \approx \frac{N_{Ind}}{N_T}\frac{4C_{NT}}{\rho_{NT}\pi <D^2> L_{Bun}} \tag{6.4}$$

Shown in figure 6.12B is the absolute number of individual nanotubes against concentration for both dilution and evaporation samples. This number density (N_{Ind}/V) does not increase linearly with concentration over the whole range, as would be expected in the absence of rebundling. As the concentration is increased, a maximum number of individual nanotubes is reached at C~0.01 mg/mL. At higher concentrations N_{Ind}/V falls

117

off, clearly indicating concentration dependent re-aggregation. The fact that this peak is observed for both the dilution and evaporation samples is further evidence of the presence of a concentration dependent equilibrium. The presence of a concentration where N_{Ind}/V is maximised immediately suggests that this is the optimum starting point for fabricating composites/dispersions containing large quantities of individual nanotubes.

By averaging over all objects with diameter less than 1.4 nm we can estimate the average nanotube diameter in our sample to be 1.0±0.1 nm. Combining this with the average nanotube length determined above we can calculate the average nanotube mass, $\langle M_{NT} \rangle$, using $\langle M_{NT} \rangle \approx \pi \langle D_{NT} \rangle \langle L_{NT} \rangle M / A$ where M/A is the mass per unit area associated with a graphitic sheet (7.7×10^{-7} kg/m^2). This works out to be $\langle M_{NT} \rangle \approx 1380 \pm 700$ kg/mol, significantly larger than our previous estimate[11]. We can apply this to the data in figure 6.12b to work out the concentration of individual nanotubes as a function of concentration from $C_{Ind} = \langle M_{NT} \rangle N_{Ind} / V$. This is shown as the right axis in figure 6.12B demonstrating at at the optimum concentration of ~0.006 mg/ml the population of individual nanotubes approaches 10% by mass.
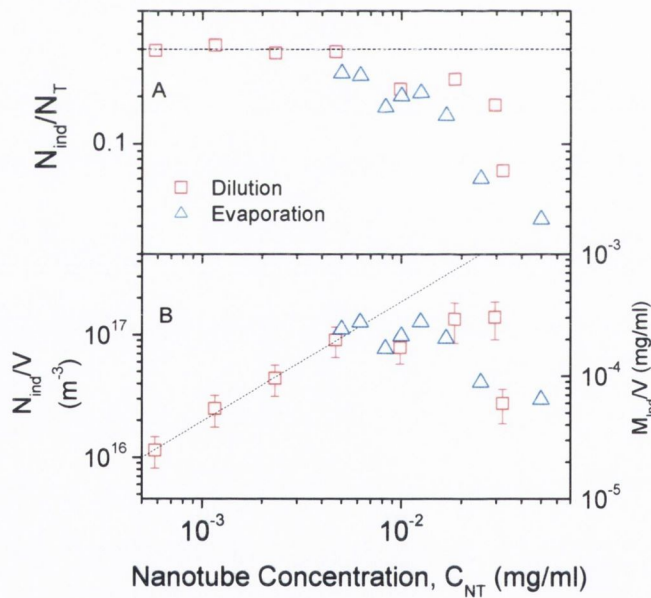

Figure 6.12

(A) Number of individual SWNTs as a fraction of the total. (B) Number of individual SWNTs per unit volume. The dashed line in both graphs indicates the low concentration regime where debundling has ceased. In (A) and (B) the dashed line is continued, illustrating what would be expected in the system if no concentration dependent bundling occurred.

It should be pointed out that such AFM measurements of bundle sizes and individual nanotube populations are generally confirmed by infra-red photoluminescence (PL) spectroscopy[11, 19]. In previous studies, the population of individual nanotubes has displayed the same concentration dependence as the PL intensity[11, 19]. This behaviour confirms that the AFM measurements reflect the state of the nanotubes in solution and are not simply due to drying effects. Such measurements were attempted as part of this study. However, no PL was observed for SWNT in GBL even though individual SWNT were unambiguously observed by AFM and HRTEM. However, PL intensities measured for nanotubes dispersed in solvents such as NMP have been extremely weak[11] suggesting that some as-yet unknown quenching process is present. It is likely that in the case of SWNT in GBL, the quenching is almost total, resulting in PL intensities below the sensitivity of our instrumentation. It is well known that optical transitions in SWNT are very sensitive to the local environment at the nanotube sidewall. The optical transition energies for both emission and absorption are extremely sensitive to both the permittivity[21] and pH[22] of the surrounding medium. More seriously, both absorptive and emissive transitions can be quenched by the presence of O_2 coupled with a low pH[23]. Thus both physical and chemical interactions, can affect nanotube PL. While it is not clear what mechanism is at work here, the fact that nanotubes dispersed in both NMP and GBL both display quenching is probably not coincidental. As we discuss below, successful solvents are those which interact strongly with the nanotube sidewall. It is likely that a secondary effect of this interaction is the quenching of the nanotube PL. In any case, as the concentrations used here are similar to those in previous studies where PL has confirmed the validity of the AFM results, we believe them to be valid in this case also.

6.5 Discussion

The question remains as to why γ-Butyrolactone is so effective at dispersing nanotubes. It certainly deviates for other successful solvents in that it is not an amide[11, 12, 24-26] or an amine[27]. In fact, to our knowledge, it is the first non-nitrogen-containing solvent to successfully disperse nanotubes (at least nanotubes without large quantities of functional groups). It seems reasonably clear that the major requirement for a successful solvent is that the energy cost of dispersing the nanotubes in solvent is not prohibitively high[11]. This cost can be expressed as the enthalpy of mixing, ΔH_{Mix}, is given by[28]: $\Delta H_{Mix} = z \Delta E n_1 \phi_2$, where z is the coordination number, n_1 is the number of moles of solvent and ϕ_2 is the

nanotube volume fraction. The parameter ΔE is the most important contributor here as it describes the balance of intermolecular interactions in the solvent-solute system. ΔE is given by

$$\Delta E = -\left(E_{11} + E_{22} - 2E_{12}\right) \tag{6.5}$$

where E_{11} is the solvent-solvent interaction energy, E_{22} is the nanotube-nanotube interaction energy and E_{12} is the nanotube-solvent interaction energy. This means that the more negative E_{12} becomes the smaller ΔE and hence ΔH_{Mix} become. We know from the value of C_2 that $\Delta H_{Mix} > 0$. This means that $|E_{12}| < (|E_{11}| + |E_{22}|)/2$. However for GBL to be a good dispersant, ΔE must be small meaning that $|E_{12}|$ must be close to its upper limit commensurate with $\Delta H_{Mix} > 0$. If the dominant type of interaction between solvent and nanotube is the dispersion interaction, then $|E_{12}| \propto \alpha_1 \alpha_2$, where α_1 and α_2 are the polarizabilities of solvent and nanotube respectively. Thus, it is likely that the success of GBL as a dispersant is due to the fact that α_1 is in just the right range such that $|E_{12}|$ is relatively large. However, it should be reiterated that $|E_{12}|$ is not large enough such that $\Delta H_{Mix} < 0$ and hence nanotubes are not truly soluble in GBL.

6.6 Conclusion

In conclusion, γ-Butyrolactone is an excellent dispersant for carbon nanotubes, rivalling amide solvents such as NMP. At higher concentrations, these dispersions display liquid crystalline behaviour as evidenced by absorption spectroscopy and crossed polarised microscopy. The aligned liquid crystalline phase can be removed by mild centrifugation. SEM measurements show the sediment to consist of aligned nanotube bundles. The boundaries between the isotropic and biphasic region and between the biphasic region and the anisotropic region of the phase diagram were determined by fitting absorbance data to the lever rule.

Sedimentation and AFM measurements show that, after mild centrifugation, the dispersions are stable against both sedimentation and aggregation. AFM further illustrates that the bundle diameters tend to decrease with concentration until very small bundles are found at low concentration. This can be explained by an equilibrium characterised by a maximum number density of bundles. This allows the calculation of the minimum solvent volume per bundle which is slightly higher than the equivalent value for NMP dispersions.

In addition, a population of individual nanotubes is present at all concentrations. The fraction of individual nanotubes increases as the concentration is decreased, approaching 40% at low concentration. We can also calculate the number density of individual nanotubes, which displays a maximum at approximately C_{NT}~0.01 mg/ml. This is then the optimum concentration for finding individual nanotubes.

The overall performance of γ-Butyrolactone as a solvent for carbon nanotubes can be measured using four parameters: dispersion limit, minimum value of D_{rms}, equilibrium volume of solvent per bundle and number fraction of individual nanotubes at low concentration. These values were (NMP values in brackets[11]): 0.004 mg/ml (~0.01 mg/ml), 2.4 nm (1.9 nm), $1.97 \pm 1.25 \times 10^{-18}$ m^3 ($6.7 \pm 2.7 \times 10^{-19}$ m^3) and 38% (70%). These values are all reasonable in comparison with NMP, which is regarded as the best known solvent for nanotubes. It seems clear that γ-Butyrolactone is a useful addition to the small but growing band of nanotube solvents.

6.6 References:

1. Accepted to Nanotechnology.
2. Galloway, G. P., Frederick-Osborne, S. L., Seymour, R., Contini, S. E. & Smith, D. E. Abuse and therapeutic potential of gamma-hydroxybutyric acid. Alcohol 20, 263-269 (2000).
3. Nicholson, K. L. & Balster, R. L. GHB: a new and novel drug of abuse. Drug and Alcohol Dependence 63, 1-22 (2001).
4. Piastra, M. et al. Lung injury from "liquid ecstasy" - A role for coagulation activation? Pediatric Emergency Care 22, 358-360 (2006).
5. Shaffer, M. S. P. & Windle, A. H. Analogies between Polymer Solutions and Carbon Nanotube Dispersions. Macromolecules 32, 6864-6866 (1999).
6. Bawden, F. The Isolation and some Properties of Liquid Crystalline Substances from Solanaceous Plants Infected with Three Strains of Tobacco Mosaic Virus Proceedings of the Royal Society of London. Series B, Biological Sciences 123, 243 (1937).
7. Somoza, A. M., Sagui, C. & Roland, C. Liquid-crystal phases of capped carbon nanotubes. Physical Review B 63, 081403 (2001).
8. Song, W. H., Kinloch, I. A. & Windle, A. H. Nematic liquid crystallinity of multiwall carbon nanotubes. Science 302, 1363-1363 (2003).
9. Davis, V. A. et al. Phase Behavior and rheology of SWNTs in superacids. Macromolecules 37, 154-160 (2004).
10. Donald, A. M. & Windle, A. H. Liquid Crystalline Polymers (Cambridge University Press, Cambridge, 1992).
11. Giordani, S. et al. Debundling of single-walled nanotubes by dilution: Observation of large populations of individual nanotubes in amide solvent dispersions. Journal of Physical Chemistry B 110, 15708-15718 (2006).
12. Landi, B. J., Ruf, H. J., Worman, J. J. & Raffaelle, R. P. Effects of alkyl amide solvents on the dispersion of single-wall carbon nanotubes. Journal of Physical Chemistry B 108, 17089-17095 (2004).

13. Song, W. H. & Windle, A. H. Isotropic-nematic phase transition of dispersions of multiwall carbon nanotubes. Macromolecules 38, 6181-6188 (2005).

14. Zhang, S. J., Kinloch, I. A. & Windle, A. H. Mesogenicity drives fractionation in lyotropic aqueous suspensions of multiwall carbon nanotubes. Nano Letters 6, 568-572 (2006).

15. Sabba, Y. & Thomas, E. L. High-concentration dispersion of single-wall carbon nanotubes. Macromolecules 37, 4815-4820 (2004).

16. Ko, H. & Tsukruk, V. V. Liquid-crystalline processing of highly oriented carbon nanotube arrays for thin-film transistors. Nano Letters 6, 1443-1448 (2006).

17. Badaire, S. et al. Liquid crystals of DNA-stabilized carbon nanotubes. Advanced Materials 17, 1673-+ (2005).

18. Nicolosi, V. et al. Solubility of Mo6S4.5I4.5 nanowires in common solvents: A sedimentation study. Journal of Physical Chemistry B 109, 7124-7133 (2005).

19. Cathcart, H. et al. Spontaneous Debundling of Single-Walled Carbon Nanotubes in DNA-Based Dispersions. J. Phys. Chem. C 111, 66-74 (2007).

20. Nicolosi, V., Vengust, D., Mihailovic, D., Blau, W. J. & Coleman, J. N. Debundling by dilution: Observation of significant populations of individual MoSI nanowires in high concentration dispersions. Chemical Physics Letters 425, 89-93 (2006).

21. Choi, J. H. & Strano, M. S. Solvatochromism in single-walled carbon nanotubes. Applied Physics Letters 90 (2007).

22. Fagan, J. A. et al. Comparative measures of single-wall carbon nanotube dispersion. Journal of Physical Chemistry B 110, 23801-23805 (2006).

23. Dukovic, G. et al. Reversible surface oxidation and efficient luminescence quenching in semiconductor single-wall carbon nanotubes. Journal of the American Chemical Society 126, 15269-15276 (2004).

24. Ausman, K. D., Piner, R., Lourie, O., Ruoff, R. S. & Korobov, M. Organic solvent dispersions of single-walled carbon nanotubes: Toward solutions of pristine nanotubes. Journal of Physical Chemistry B 104, 8911-8915 (2000).

25. Furtado, C. A. et al. Debundling and dissolution of single-walled carbon nanotubes in amide solvents. Journal of the American Chemical Society 126, 6095-6105 (2004).

26. Liu, J. et al. Controlled deposition of individual single-walled carbon nanotubes on chemically functionalized templates. Chemical Physics Letters 303, 125-129 (1999).

27. Maeda, Y. et al. Dispersion of single-walled carbon nanotube bundles in nonaqueous solution. Journal of Physical Chemistry B 108, 18395-18397 (2004).

28. Donald, A. M., Windle, A. H. & Hanna, S. Liquid Crystalline Polymers (Cambridge University Press, Cambridge, 2006).

Chapter 7

Large Populations of Individual Single Walled Nanotubes in Surfactant-Based Dispersions without the need for Ultracentrifugation

7.1 Introduction

This chapter demonstrates stable dispersions of single walled carbon nanotubes produced using the surfactant sodium dodecylbenzene sulphonate (SDBS). The sonicate/dilute/mild-centrifuge technique employed in the previous chapters has been extended to this tertiary system. As surfactant based dispersions are probably the most utilised, when it comes to implementing individual SWNTs into various composites this serves as a comparison for the two phase mixtures described in previous chapters. Furthermore, we investigate how the concentration dependent exfoliation method developed in this thesis can be used to improve the standard method of dispersing SWNTs in surfactant systems.

7.2 Background

Despite the large amount of research dedicated to finding innovative and effective methods for dispersing SWNTs, surprisingly little discussion has appeared on what constitutes a good dispersion. To first order, the answer appears simple: a perfect dispersion is one where all the nanotubes are dispersed individually. However due to their large surface energy[1], nanotubes tend to aggregate into bundles. Over the years much work has focused on debundling or exfoliating the nanotubes. However, to our knowledge, no reports exist of dispersions where the nanotubes are 100% exfoliated. Highly exfoliated

dispersions, where up to 90% of the objects observed were individuals have be reported only at low concentration[2, 3]. This brings us to the second condition for a good dispersion: large populations of individual nanotubes must exist at high concentration. This is crucial to many applications where scale-up is important. Here fundamental limitations come into play. For entropic reasons, dispersions of rods tend to align to form nematic arrays at concentrations above $C^* \approx 3.3\rho d/l$, where ρ is the mass density and d/l is the rod aspect ratio[4]. As the concentration gets higher, adjacent rods get closer and attractive van der Waals forces increase to the point that aggregation becomes inevitable no matter how the dispersion is stabilized. Even dispersed SWNT, stabilized by protonation in super-acids have not been realised above ~80 mg/mL[5]. Thus it is not realistic to expect to achieve large scale exfoliation at arbitrarily high concentrations. However one can ask; what is the maximum partial concentration of individual SWNTs achievable in a given system? For SWNTs dispersed in the solvent NMP, this has been measured to be ~10^{-3} mg/mL individuals in a total concentration of ~8×10^{-3} mg/mL[3]. However, it is probable that this quantity is much higher in other systems.

For some applications such as composite formation, it is not absolutely necessary to produce dispersions with very high populations of individual nanotubes. For example, to produce highly conductive composites, it can be sufficient to prepare a dispersion containing a very large quantity of small bundles. To achieve this we need to know what is the maximum number of rods we can obtain per volume of solvent. This means balancing exfoliation with maximisation of concentration while maintaining dispersion. To our knowledge, neither the question of the maximum partial concentration of individual SWNTs nor maximum number densities of rods achievable have been addressed for the vast majority of systems.

It is generally agreed that surfactants are the dispersant of choice for SWNTs[6]. However, standard processing techniques remain limited. Typically, a nanotube/surfactant dispersion is produced by sonication and then ultracentrifuged at up to 122,000g to remove most of the bundles[7]. This results in significant mass loss[8], and leaves the researcher with very little control over the properties of the resultant dispersion once he has chosen his surfactant. This is in contrast to recent studies which have shown that the bundle diameter distribution and the population of individual SWNTs can be controlled in certain solvent based dispersions by controlling the nanotube concentration[3]. Similar behaviour was subsequently demonstrated for dispersions of SWNT in genomic DNA[9]. The aim of this study is to investigate whether such nano-scale control is possible in SWNT dispersions based on common surfactants. We have chosen to use the surfactant sodium

dodecylbenzene sulphonate (SDBS) for a number of reasons. SDBS is a commonly used surfactant which is known to readily disperse nanotubes with no strong diameter dependence[10, 11]. Furthermore small angle neutron scattering measurements on SDBS/SWNT dispersions show Q^{-1} dependence demonstrating that the nanotubes are dispersed as 1D rigid rods (i.e. well dispersed)[12]. As such we propose to use SDBS as a model dispersant to investigate the possibility of concentration dependent effects in surfactant systems.

In this chapter, it will be shown that nanotubes dispersed in SDBS can be exfoliated simply by dilution while keeping the SDBS concentration constant. We find that the root mean square bundle diameter falls monotonically with concentration before saturating at ~2 nm at concentrations below 0.05 mg/mL. The total number of rods per volume increases with increasing concentration, saturating at ~6 μm^{-3} at concentrations above 0.05 mg/mL. Furthermore large populations of individual SWNT were observed at all concentrations, reaching a maximum partial concentration of individuals of ~0.006 mg/mL individuals at a total concentration of ~0.07 mg/mL.

7.3 Experimental Procedure

Purified single-walled carbon nanotubes (SWNT) were purchased from Carbon Nanotechnologies Inc. (HiPCO, www.cnanotech.com, Lot number: P0288) and used as received. Sodium dodecylbenzene sulphonate, $C_{18}H_{29}NaO_3S$, (SDBS) was purchased from Alrdich (lot no. 065K2511). A stock solution of SDBS, of concentration 5mg/mL in Millipore water, was prepared by stirring overnight. This concentration was chosen such that it was well above the critical micelle concentration for SDBS (~0.5 mg/mL). In addition, Small-Angle Neutron Scattering (SANS) studies on Triton X-100 dispersions show that the optimum surfactant concentration is in the range 4-20 mg/mL, independent of nanotube concentration[13]. Assuming that the equivalent values for SDBS are similar, we chose 5 mg/mL as a reasonably low surfactant concentration consistent with the conditions described above.

Some of this solution was used to prepare a stock composite dispersion by adding single-walled carbon nanotubes such that the SDBS:SWNT mass ratio was 5:1 (nanotube concentration, C_i=1 mg/mL). This mass ratio was chosen with care. The effective area of an SDS headgroup (SDBS is expected to be similar) is ~0.5 nm^2.[14] This means that the minimum mass ratio of surfactant:SWNT required to completely coat an individual SWNT is ~2. In any real dispersion, the surfactant coating will be in equilibrium with individually

dispersed surfactant molecules and surfactant molecules in micelles. This means that the minimum SDBS:SWNT mass ratio must be greater than 2. Thus, allowing some margin of error leads to our choice of 5:1.

A volume of 8mL of this stock dispersion was then subjected to 5mins high power sonication with ice cooling (Model GEX600; 240W, 60kHz). A range of dispersions, of varying nanotube concentrations, was made by blending the stock nanotube dispersion with the stock SDBS solution. After each dilution, the dispersions were tip-sonicated for 5 minutes. This resulted in an initial concentration range of C_i=1mg/mL to 0.004mg/mL. It should be noted that the SDBS concentration was 5mg/mL in each dispersion. The entire dispersion set was then placed in a sonic bath (Model Ney Ultrasonic) for 1 hr and then each was again subjected to 5 mins of high power sonication. Samples were mildly centrifuged at 5500rm for 90mins (~ 3000g) followed by decantation of the supernatant. The UV-Vis-NIR absorbance was recorded (Cary 5000i) for each concentration before and after centrifugation

Samples were prepared for Atomic Force Microscopy (AFM) characterisation by soaking functionalised silicon discs[15] in the dispersions for approximately 3 hours. The samples were then rinsed with methanol and lightly blow dried. This method removed any residual SDBS from the Si surface. Tapping mode AFM (Multimode Nanoscope IIIA, using Pointprobe silicon cantilevers with force constant = 42 Nm^{-1} & resonant frequency = 330kHz) was carried out on each sample and a distribution of the SWNT diameters for each sample was recorded and statistical data relating to the debundling process extracted[3]. A dispersion with a mid-range concentration was prepared directly, i.e. without successive dilutions from a starting stock solution. Thus, this sample received considerably less sonication and it was used to prepare a sample for AFM analysis. The dispersion was then allowed to evaporate in a controlled manner and an AFM sample of the more concentrated dispersion was prepared.

Near-IR photoluminescence (IRPL) maps were compiled by scanning the emission from dispersed SWNTs for incrementing excitation wavelengths (Edinburgh Instruments FLS 920 fluorescence spectrometer fitted with a Hamamatsu R5509 near-IR photo-multiplier tube). A IRPL map consisted of scanning emission spectra (900–1400nm, in 4nm steps) for incrementing excitation wavelengths in the range of 550–890nm (also in 4nm steps). These maps were recorded at various points in the concentration range investigated. Line spectra, exciting at 740 and 660nm, show the trend of IRPL intensity with concentration.

The stability of the dispersions was investigated by monitoring the transmission through a medium range concentration (C_{NT}= 0.01mg/mL) over a 35 day period[16, 17]. It should be pointed out that the dilution series reported was prepared by diluting with surfactant solutions rather than pure water as high quality nanotube dispersions cannot be prepared unless the surfactant concentration is above the CMC[10]. To confirm this, we prepared and characterised a dilution series diluting with water. For all dilutions, the quality of the dispersions as measured by both AFM and IRPL was very poor compared to the surfactant diluted series.

7.4 Results

Debundling by Dilution.

The sample preparation described results in black homogeneous dispersions. Any micron sized aggregates were removed by mild centrifugation. Absorbance before and after centrifugation was used to quantify the percentage of aggregates removed for each concentration dispersion, as shown in figure 7.1A. Before centrifugation the absorbance (660 nm) scaled linearly with concentration yielding an extinction coefficient of 3389 $mLmg^{-1}m^{1}$ (see figure 7.1B). After CF the absorbance had decreased indicating the removal of aggregates. Calculating the ratio of absorbance at a fixed wavelength before and after CF allows us to quantify the concentration of SWNT remaining in each supernatant (this concentration will be referred to as C_{NT} and should not be confused with the initial concentration, C_{i}).[3] After centrifugation between 22wt% and 65wt% of the nanotubes remained depending on the concentration, as outlined in figure 7.1C.
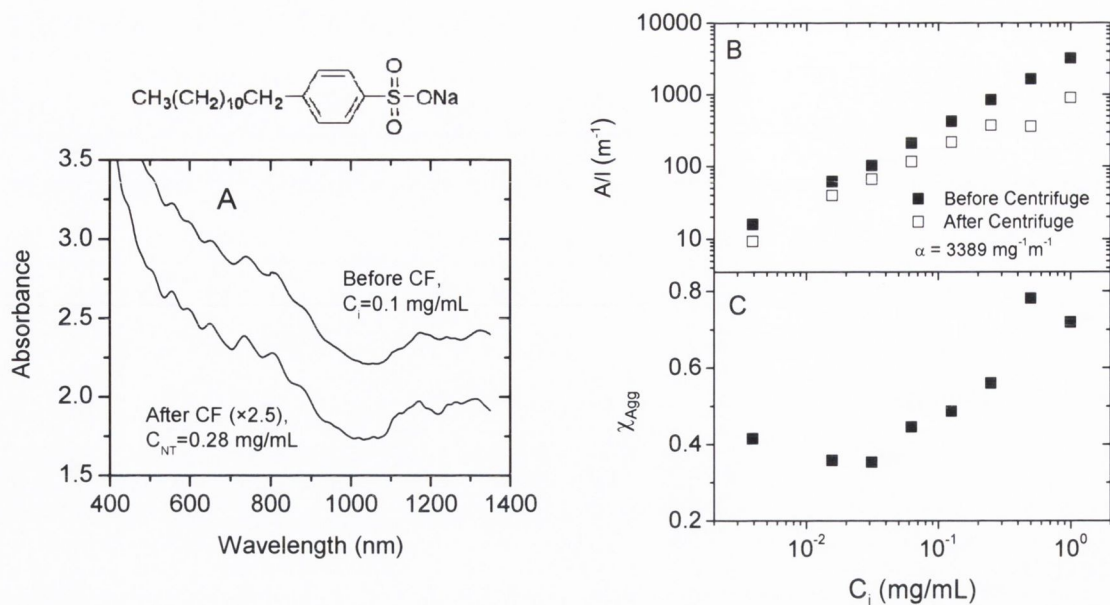
Figure 7.1

A) Absorption spectra taken before and after centrifugation for the $C_i=1mg/mL$ sample. B) Absorbance per unit length (A/l), at 660nm, is plotted against initial SWNT concentration, C_i. The extinction coefficient is calculated at low concentrations to be 3389 mg^{-1}m^{-1}. The chemical structure of sodium dodecylbenzenesulfonate (SDBS) is also inserted. C) The percentage of aggregates present, as function of C_i is shown, where $\chi_{Agg}=(C_i-C_f)/C_i$.

The stability of these dispersions has been monitored by measuring the optical absorbance as a function of time, demonstrating no sedimentation over at least 35 days as shown in figure 7.2[18].
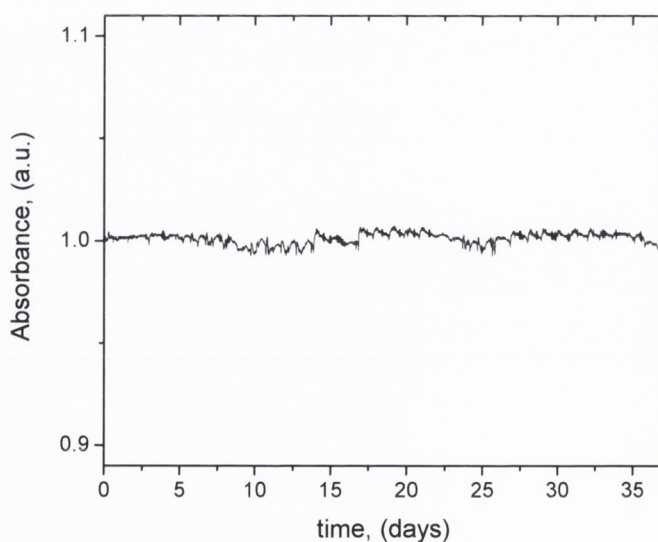
Figure 7.2

Normalised absorbance (at 650nm) as a function of time, for NT-SDBS dispersion at C=0.01mg/mL.

Here we are interested in characterising the state of the nanotubes at the nano-scale. To do this we examine deposited samples with tapping-mode atomic force microscopy (AFM). Large populations of 1-dimensional objects, consistent with bundles of SWNT, were clearly present at all concentrations. Figures 7.3A and 7.3B show images for two concentrations C_{NT}=0.28mg/mL and C_{NT}=0.01mg/mL, respectively.

Figure 7.3

AFM images for (A) C=0.28mg/mL and (B) C=0.01mg/mL.

To quantify the nature of these objects, the heights of 150 bundles were measured for each concentration. These heights correspond to the bundle diameters, the distributions of which are shown in figure 7.4. Moving from high to low SWNT concentrations, the distribution of bundle diameters narrows and shifts to lower diameter values.

Figure 7.4
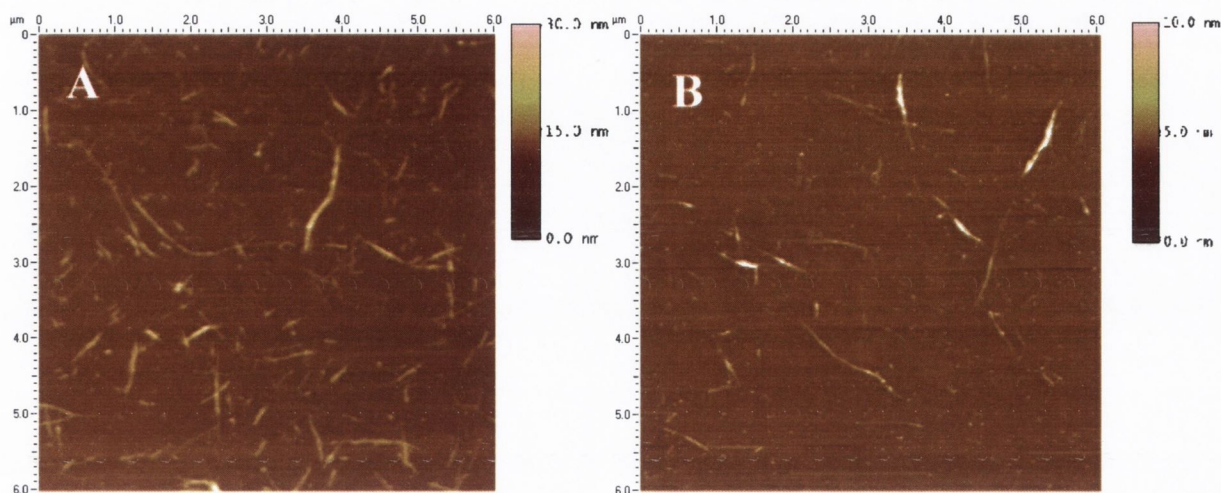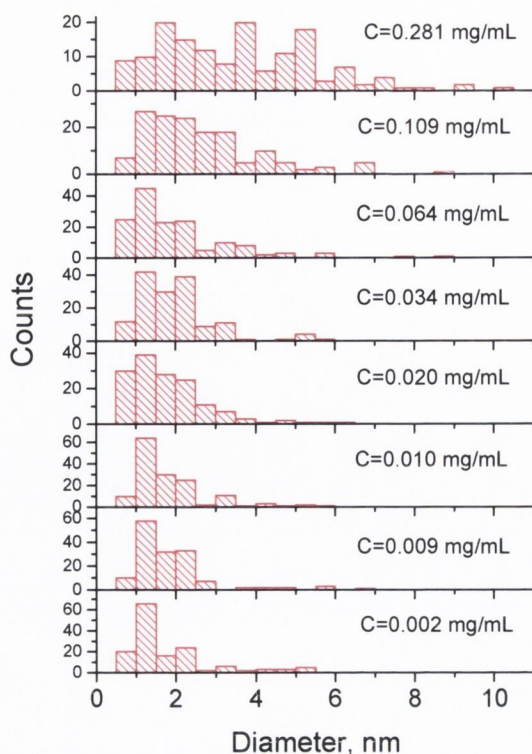
Bundle diameter distributions are shown for all concentrations investigated. The broad distribution at higher concentrations narrows as the concentration lowers. Objects with diameters less than 1.4nm which represent individual SWNTs are present at all concentrations.

Representing the diameter distribution by its root-mean-square, ($D_{rms} = \sqrt{<D^2>}$), shows clear debundling with decreasing concentration between 0.3 and 0.03 mg/ml (figure 7.5A). Below 0.03mg/mL, D_{rms} saturates at (2.1±0.1)nm. This trend is consistent with the debundling by dilution recently demonstrated for amide solvents such as NMP[3]. However, as shown in figure 7.5, debundling in SDBS dispersions occurs at significantly higher concentrations compared to NMP dispersions. The average length of all objects observed (bundles and individual nanotubes) was measured to be concentration independent over the whole range with an overall average of $<L>=(1.4\pm0.1)\mu m$. By considering only objects with D<1.4nm we could estimate the individual SWNT length to be $<L_{Ind}>=(0.9\pm0.1)\mu m$.

Such concentration dependent debundling has been modelled in terms of an equilibrium characterised by a concentration invariant number density of bundles[3]. Such a scenario leads to a well defined concentration dependence of D_{rms}:

$$D_{rms} = \sqrt{\langle D^2 \rangle} \approx \left[\frac{4C_{NT}}{\rho_{NT} \cdot \pi \langle L \rangle (N/V)_{Eq}} \right]^{1/2} \qquad (7.1)$$

where ρ_{NT} is the nanotube density and $(N/V)_{eq}$ is the equilibrium bundle number-density. Fitting this equation to the data in figure 7.2 gives (N/V_{eq})=5.8 μm^{-3}. This value is significantly higher than that measured for the amide solvent NMP (1.5 μm^{-3}) indicating that bundles can be stably dispersed at closer proximity in dispersions based on SDBS compared to NMP.
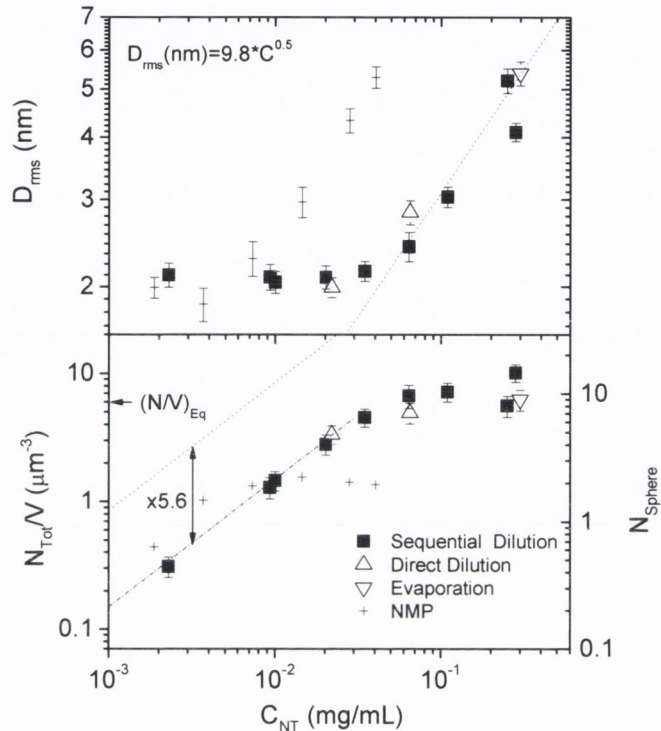
Figure 7.5

Data derived from statistical analysis of the AFM images for samples   A) The measured diameter distributions, presented as D_{RMS}, plotted against SWNT concentration. Bundles sizes reduce with concentration until they saturate at 2.1nm. The dotted line is a fit to equation (7.1) B) Total number density of all bundles and individuals as calculated using equation (7.2) The value of $(N/V)_{Eq}$, calculated from the fit in figure 7.5A is indicated by the arrow. The lower dotted line is a linear fit to the low concentration portion of the curve. The upper dotted line is the theoretical curve, calculated using equation (7.2), assuming all nanotubes are individuals.

To demonstrate that this equilibrium is independent of preparation conditions (i.e. sonication/dilution), samples of mid-range concentration (C_{NT}=0.065 & 0.022mg/mL) were prepared directly from the centrifuged stock solution thus receiving minimal

sonication. As shown in figure 7.5, the resulting D_{rms} values fall on the trend line discussed above. In addition, after increasing the concentration by controlled solvent evaporation, from C_{NT}=0.022mg/mL to 0.3 mg/mL, D_{rms} again falls on the trend line confirming the concentration dependent equilibrium.

For many applications, such as composite formation, high quality dispersions are required at high concentration. However, we have just seen that the quality of the dispersion, as measured by the extent of nanotube exfoliation, decreases as the concentration is increased. A criterion that takes this into account would be that the number of all bundles and individual nanotubes per unit volume is maximized. We can calculate the number of bundles/individuals per volume to be:

$$\frac{N_{Tot}}{V} = \frac{4C}{\rho_{NT}\pi\langle D^2\rangle\langle L\rangle} \qquad (7.2)$$

(N.B. $\langle D^2\rangle = D_{rms}^2$). This quantity is plotted in figure 7.5B for all the data presented in figure 7.5A. As can be seen, for all the samples prepared using SDBS, N_{Tot}/V falls on a single curve. At low concentration, this data increases linearly with concentration as illustrated by the dash-dot line. At concentrations above ~0.04 mg/mL, the curve turns over slightly as bundling at higher concentration takes effect. Ultimately, N_{Tot}/V saturates, approaching 6 μm^{-3} at high concentrations. This is a reasonably high population; ~6 micron long objects dispersed in a micron sized cube. In the ideal case we would have dispersions of only individual SWNT. Using equation (7.2) and the known dimensions for individual SWNT (D~1nm, L~1000nm) we can plot the theoretical maximum value of N_{Tot}/V as the dotted line in figure 7.5B. Low concentration dispersions of SWNT in SDBS are only a factor of ~6 below this maximum. We can contrast data for N_{Tot}/V measured for SWNT dispersed in NMP. At low concentrations N_{Tot}/V is slightly higher for NMP dispersions than SDBS dispersions. However, as nanotube bundling becomes significant at lower concentrations for the NMP based dispersions (~5×10^{-3} mg/mL), N_{Tot}/V tends to saturate at lower concentrations (~2×10^{-2} mg/mL) compared to the SDBS samples. More tellingly, the maximum value of N_{Tot}/V is almost a factor of 10 lower in the NMP dispersions.

To understand the proximity of adjacent SWNT, it is worth considering the volume of solvent defined by the sphere traced by the ends of an average bundle. As the mean bundle length is concentration independent, so is the volume of this sphere. For NMP dispersions at higher concentrations, such a sphere contains on average slightly less than one bundle thus ensuring stability against aggregation due to rotational diffusion[3]. The number of bundles occupying this sphere, N_{sphere}, can be calculated using

$$N_{sphere} = \frac{N_{Tot}}{V} \frac{4}{3} \pi \left(\frac{L_{Bun}}{2} \right)^3 \qquad (7.3)$$

N_{sphere} is plotted as a function of nanotube concentration in figure 7.5B (right axis). As the concentration increases, N_{sphere}, increases steadily, approaching 10 at 0.3 mg/ml, significantly greater than the value of ~1 observed for NMP. The fact that so many bundles can stably occupy such a small volume confirms that surfactant dispersed nanotubes are effectively stabilised by inter-surfactant repulsion. Such stabilisation has previously been demonstrated for acid based SWNT dispersions where up to ~30 protonated individual nanotubes were observed per spherical volume[5]. However, to have comparable values of N_{sphere} in such a benign system as SDBS/H_2O is extremely useful.

When the population of dispersed rods is so large that N_{sphere} is significantly greater than 1, we can no longer consider this dispersion as dilute[3]. It may be more appropriate to consider the system as a loose network of rods. This has previously been observed for dispersions of SWNT in SDBS by SANS where a transition from Q^{-1} to Q^{-n} (n>1) behaviour in the vicinity of Q=0.003A^{-1} indicates a changeover from 1D to network character at length-scales above ~150 nm[12]. The existence of such networks has previously allowed the measurements of both thermal conductivity[19] and electrical percolation in nanotube/surfactant dispersions[20, 21].

Population of Individual nanotubes

By counting the fraction of objects with diameters less than 1.4 nm one can obtain information about the population of individual nanotubes[3, 9]. Figure 7.6A shows the number fraction of individual SWNTs, (N_{Ind}/N_T), as a function of SWNT concentration. At high concentrations N_{Ind}/N_T is of the order of 10%. As the concentration is lowered, debundling results in an increase in the fraction of individual nanotubes, saturating around 45% at low concentration. In comparison, while dispersions of SWNT in NMP display N_{Ind}/N_T at low concentration as high as 65%[3] much lower fractions of individual nanotubes are seen at high concentration.
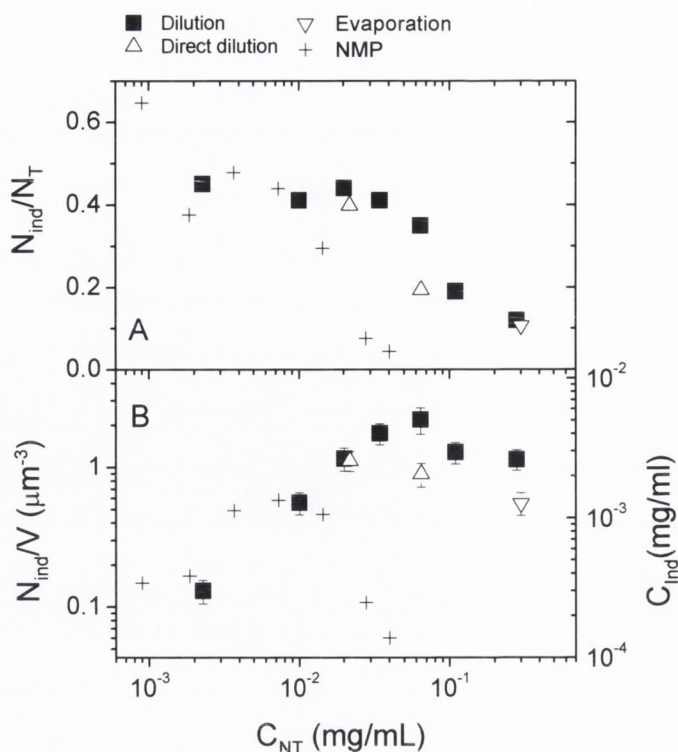
Figure 7.6

(A) The number fraction of individual SWNTs is plotted against SWNT concentration. (B) Using equation (7.2) the corresponding number of individual SWNTs per unit volume, is shown as a function of SWNT concentration.

The number fraction of individual tubes can be used to generate the absolute number of individual nanotubes per unit volume (figure 7.6) of solvent using[3]

$$\frac{N_{Ind}}{V} \approx \frac{N_{Ind}}{N_T} \frac{4C_{NT}}{\rho_{NT} \cdot \pi \langle D^2 \rangle \langle L \rangle} \tag{7.2}$$

As the concentration is decreased the population of individual nanotubes actually increases as debundling outpaces the reduction in concentration. As the concentration is reduced below ~0.03 mg/mL debundling ceases resulting in a linear decrease in the population of individual nanotubes as the concentration is further decreased. While the population of individual nanotubes observed here is comparable to that for NMP at low concentration, much larger populations are observed in the higher concentration; ($\sim 2 \ \mu m^{-3}$@0.04 mg/mL) compared with NMP dispersions ($\sim 0.05 \ \mu m^{-3}$@0.04 mg/mL)[3]. This is the true advantage of surfactant based dispersions; good dispersions, characterised by high concentrations of individual nanotubes, can be maintained up to high concentrations.

By carefully measuring the diameters and lengths of the individual nanotubes observed in this study we can estimate the average nanotube molar mass to be 1380

134

kg/mol. We can use this value to transform the data in figure 7.6B into the partial concentration of individual nanotubes, C_{Ind} (right axis, figure 7.6B). Thus value peaks at approximately 5×10^{-3} mg/ml at a concentration of C_{NT}=0.06 mg/ml. This value is significantly higher than the maximum attained using NMP, or indeed any dispersant/solvent known to the authors. At this concentration, nearly 10% by mass of the nanotubes are individually dispersed.

Correlation of AFM with IRPL

The AFM results are supported by IRPL measurements. Figure 7.7 shows an IRPL excitation-emission map for C_{NT}=0.01mg/mL and C_{NT}=0.002mg/mL respectively, both demonstrating strong IRPL. Emission line spectra were recorded for all concentrations, exciting at 660nm. The IRPL intensity (λ_{Em}=1307nm) is shown versus concentration in figure 7.8A. As the IRPL intensity is proportional to the number of individual SWNT in the dispersion, concentration dependent measurements have previously been used to confirm the results of AFM analysis[3, 9]. However, those reports studied low concentration dispersions. For the higher concentration dispersions studied here, inner-filter and reabsorption effects, which reduce the IRPL intensity at higher concentrations, become important[22, 23].
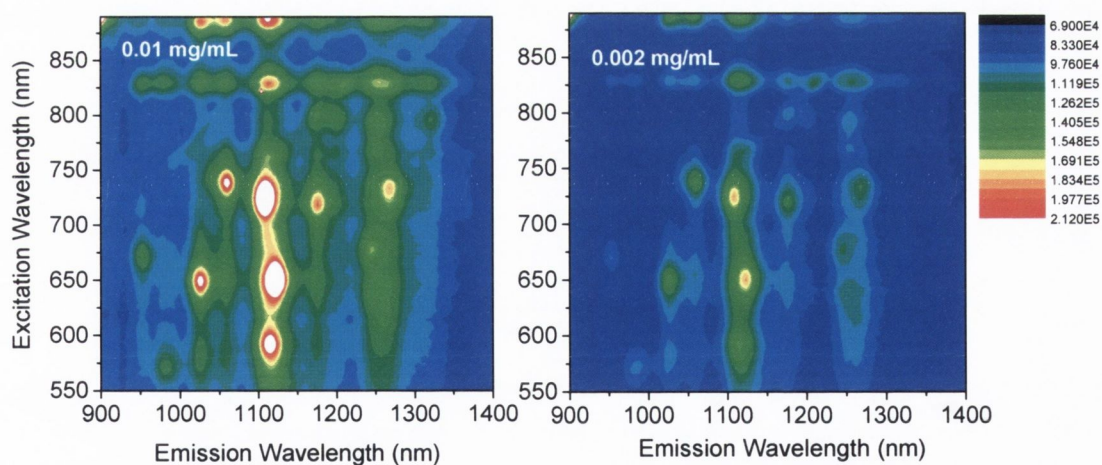

Figure 7.7

Photoluminescence (IRPL) maps of SWNTs dispersed in SDBS at concentrations 0.01mg/mL and 0.002mg/mL respectfully.

As shown in figure 7.8A, the lower concentration portion of the observed IRPL data scales linearly with concentration (dotted line). In this concentration range, the

fraction of individual tubes is constant so the linearity of the curve means that inner-filter and reabsorption effects are negligible below ~0.005 mg/mL ($A/l < 20m^{-1}$). Using the slope of this curve it is possible to use a simple model[24] to predict the IRPL intensity as a function of concentration taking into account inner-filter and reabsorption effects *but not aggregation*. This curve is shown in figure 7.8A and matches the observed data reasonably well. This shows that inner-filter and reabsorption effects dominate the PL intensity at concentrations below ~0.005 mg/mL. However, the observed IRPL intensity is lower than predicted at high concentration. We believe this discrepancy is due to the IRPL quenching associated with bundling at high concentrations[3, 9]. The ratio of observed to predicted IRPL is given in figure 7.8B, clearly showing a deviation from 1 at C_{NT}~0.015 mg/mL suggesting that bundling becomes significant above this concentration. To compare this with the AFM data, the N_{Ind}/V data from figure 7.6B is reproduced in figure 7.8C. The dotted line demonstrates the trend predicted if bundling didn't occur at higher concentrations. The deviation of observed N_{Ind}/V from predicted N_{Ind}/V is illustrated by plotting the ratio of these quantities in figure 7.8D. This ratio deviates from 1 at a concentration of C_{NT}~0.025 mg/mL, due to the presence of concentration dependent aggregation at higher concentrations. That this concentration is so close to that where IRPL quenching is first observed strongly supports the validity of our AFM analysis. That an in-situ measurement such as IRPL gives similar results to AFM measurements in deposited samples gives confidence that the AFM data is not tainted by drying effects.
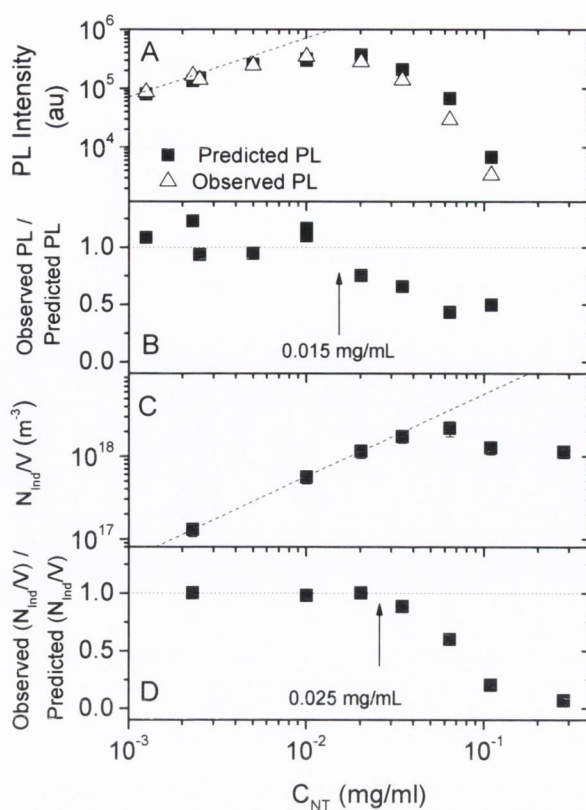
Figure 7.8

(A) The intensity of IRPL emission line-spectra (where λ_{ex}=660nm), both observed and predicted, is plotted against SWNT concentration. (B) Deviation of Observed IRPL from predicted IRPL at high concentration is due to bundling induced quenching. C) N_{Ind}/V reproduced from figure 7.6B. The dotted line represents the trend in the absence of high concentration bundling. D) Deviation of observed N_{Ind}/V from predicted N_{Ind}/V is due to bundling at high concentration. The onset concentration is very similar to the onset of quenching.

7.5 Conclusion

In conclusion, we have produced stable dispersions of suspended SWNTs using SDBS in water. The SWNTs are in the form of individuals and small bundles with no aggregates. This has been achieved without the need for ultracentrifugation at nanotube concentrations of up to 0.28 mg/mL. As the concentration is reduced by dilution with surfactant solution, exfoliation of the nanotubes from the bundles is observed, manifesting itself as a reduction in bundle diameter and increase in the number fraction of individual SWNTs. Larger bundle diameters, at higher concentrations, result in saturation of the total

number density of bundles and individuals at ~6 rods per cubic micron. As the concentration was decreased the number fraction of individual SWNTs increased from ~20% to ~50%. The maximum concentration of individuals was measured to be 5×10^{-3} mg/ml at a total SWNT concentration of C_{NT}=0.06 mg/ml. At this concentration, nearly 10% by mass of the nanotubes are individually dispersed. The onset of aggregation at higher concentration has been confirmed by lower than expected PL intensity at concentrations above 0.015 mg/mL.

Qualitatively, the concentration dependence of the bundle statistics measured here are similar to those for solvents such as NMP. However, the big difference is that, for SDBS dispersions, similar results, in terms of dispersion quality, are obtained at significantly higher concentrations. This means that smaller bundle diameters and hence larger number densities of bundles can be attained at a given concentration in SDBS compared to NMP. This is likely due to the inter-bundle repulsion induced by the (an)ionic surfactant head groups. This is an important result in terms of applications based on solution processing of SWNTs. While high quality, two phase dispersions based on NMP and other solvents are aesthetically attractive compared to surfactant dispersions, the low concentrations required are prohibitive. In simple terms of attainable rod number density, these results confirm that SDBS dispersions are superior to dispersions of SWNT in NMP or other solvents. In addition, using centrifugation rather than ultracentrifugation means that the mass loss is much lower leading to higher yield and less wastage. We expect that the actual mass loss on centrifugation could be reduced significantly by careful optimisation of the dispersion procedure. Overall, we believe these results will have an impact in areas from nanotubes sorting to composite formation.

7.6 References

1.   Nuriel, S., Liu, L., Barber, A. H. & Wagner, H. D. Direct measurement of multiwall nanotube surface tension. Chemical Physics Letters 404, 263-266 (2005).
2.   Furtado, C. A. et al. Debundling and dissolution of single-walled carbon nanotubes in amide solvents. Journal of the American Chemical Society 126, 6095-6105 (2004).
3.   Giordani, S. et al. Debundling of single-walled nanotubes by dilution: Observation of large populations of individual nanotubes in amide solvent dispersions. Journal of Physical Chemistry B 110, 15708-15718 (2006).
4.   Sabba, Y. & Thomas, E. L. High-concentration dispersion of single-wall carbon nanotubes. Macromolecules 37, 4815-4820 (2004).

5. Davis, V. A. et al. Phase Behavior and rheology of SWNTs in superacids. Macromolecules 37, 154-160 (2004).

6. Vaisman, L., Wagner, H. D. & Marom, G. The role of surfactants in dispersion of carbon nanotubes. Advances in Colloid and Interface Science 128, 37-46 (2006).

7. O'Connell, M. J. et al. Band gap fluorescence from individual single-walled carbon nanotubes. Science 297, 593-596 (2002).

8. Moore, V. C. et al. Individually suspended single-walled carbon nanotubes in various surfactants. Nano Letters 3, 1379-1382 (2003).

9. Cathcart, H. et al. Spontaneous debundling of single-walled carbon nanotubes in DNA-based dispersions. Journal of Physical Chemistry C 111, 66-74 (2007).

10. McDonald, T. J., Engtrakul, C., Jones, M., Rumbles, G. & Heben, M. J. Kinetics of PL quenching during single-walled carbon nanotube rebundling and diameter-dependent surfactant interactions. Journal of Physical Chemistry B 110, 25339-25346 (2006).

11. Okazaki, T. et al. Photoluminescence mapping of "as-grown" single-walled carbon nanotubes: A comparison with micelle-encapsulated nanotube solutions. Nano Letters 5, 2618-2623 (2005).

12. Zhou, W. et al. Small angle neutron scattering from single-wall carbon nanotube suspensions: evidence for isolated rigid rods and rod networks. Chemical Physics Letters 384, 185-189 (2004).

13. Wang, H. et al. Dispersing single-walled carbon nanotubes with surfactants: A small angle neutron scattering study. Nano Letters 4, 1789-1793 (2004).

14. Strano, M. S. et al. The role of surfactant adsorption during ultrasonication in the dispersion of single-walled carbon nanotubes. Journal of Nanoscience and Nanotechnology 3, 81-86 (2003).

15. Liu, J. et al. Controlled deposition of individual single-walled carbon nanotubes on chemically functionalized templates. Chemical Physics Letters 303, 125-129 (1999).

16. Nicolosi, V. et al. Solubility of Mo6S4.5I4.5 nanowires in common solvents: A sedimentation study. Journal of Physical Chemistry B 109, 7124-7133 (2005).

17. Nicolosi, V. et al. Solubility of Mo6S4.5I4.5 nanowires. Chemical Physics Letters 401, 13-18 (2005).

18. See supplemental Information.

19. Huxtable, S. T. et al. Interfacial heat flow in carbon nanotube suspensions. Nature Materials 2, 731-734 (2003).

20. Lisunova, M. O., Lebovka, N. I., Melezhyk, E. V. & Boiko, Y. P. Stability of the aqueous suspensions of nanotubes in the presence of nonionic surfactant. Journal of Colloid and Interface Science 299, 740-746 (2006).

21. Vigolo, B., Coulon, C., Maugey, M., Zakri, C. & Poulin, P. An experimental approach to the percolation of sticky nanotubes. Science 309, 920-923 (2005).

22. Miller, J. N. Standards in fluorescence spectrometry (Chapman and Hall, London, 1981).

23. Parker, C. A. Photoluminescence of solutions, with applications to photochemistry and analytical chemistry (Elsevier, 1968).

24. Rickard, D., Giordani, S., Blau, W. J. & Coleman, J. N. Journal of Luminescence (In press) (2007).

Chapter 8

Conclusions & Future Work

The aim of this thesis was to demonstrate the exfoliation of single walled carbon nanotubes (SWNTs) in various media, whilst garnering a solid understanding of the physical processes that govern the debundling process. Initially, using NMP it has been shown that good quality SWNT dispersions can be routinely fabricated without the need for ultracentrifugation. A sonication/dilution/mild-centrifuge preparation scheme was employed resulting in a concentration range of dispersions, the centrifuge removing large aggregates present in the dispersion. UV-vis-NIR absorbance spectra, recorded for each concentration before *and* after centrifugation, showed no aggregates to be present below $C_{NT}=0.02$mg/mL: this is referred to as the dispersion limit of NMP. A concentration dependent process of debundling by dilution was demonstrated based on statistical data taken from AFM images of the dispersions over the concentration range prepared. Bundle diameter was seen to fall off with concentration, until reaching a plateau of 1.9nm. Populations of individual nanotubes were observed for every concentration investigated approaching 70% at low concentration. Furthermore, the partial concentration of individual SWNTs was found to be maximised at $C_{NT}\sim0.01$ mg/ml. This was reasoned as the best possible starting concentration for implementing the maximum number of individual SWNTs into a composite requiring such. The presence and quantity of individual nanotubes in each concentration dispersion was confirmed by IRPL. IRPL maps showed peaks corresponding to various chiralities of individual semiconducting SWNTs.

Further information on the nature of SWNT debundling in two phase media was ascertained from studying the debundling by dilution of SWNTs in the street drug γ-Butyrolactone: a new, previously unknown, solvent for SWNTs. At higher concentrations, these dispersions displayed liquid crystalline behaviour as evidenced by absorption spectroscopy and crossed polarised microscopy. The aligned liquid crystalline phase was shown to be removed by mild centrifugation. SEM measurements showed the sediment to

consist of aligned nanotube bundles. The boundaries between the isotropic and biphasic region and between the biphasic region and the anisotropic region of the phase diagram were determined by fitting absorbance data to the lever rule. The dispersions in the isotropic range were investigated with AFM in an analogous manner to the dispersion study for NMP. The overall performance of γ-Butyrolactone as a solvent for carbon nanotubes was measured using four parameters: dispersion limit, minimum value of D_{rms}, equilibrium volume of solvent per bundle and number fraction of individual nanotubes at low concentration. These values were (NMP values in brackets): 0.004 mg/ml (~0.01 mg/ml), 2.4 nm (1.9 nm), $1.97\pm1.25\times10^{-18}$ m^3 ($6.7\pm2.7 \times10^{-19}$m^3) and 38% (70%). These values are all reasonable in comparison with NMP, which is regarded as the best known solvent for nanotubes.

Serious consideration was given to the thermodynamics of SWNT debundling in two phase media. The literature in this area is peppered with references to SWNT *solutions/suspensions/dispersions* etc. without much thought as to the thermodynamics of the system in question. Evidence has been presented showing that nanotubes, dispersed in NMP, can spontaneously exfoliate on dilution resulting in a decrease in bundle diameter and an increase in population of individual nanotubes to equilibrium values. It was also demonstrated that nanotube dispersability is maximised in solvents whose surface energy matches that of graphitic surfaces, consistent with NMP dispersions having close to zero enthalpy of mixing. This was confirmed by a measurement of the Flory-Huggins parameter showing that the enthalpy of mixing to be negative and confirming true solubility of SWNT in NMP. STM images showed NMP to be physisorbed to SWNTs. This is the first reported evidence of a SWNT solution clearly outlining the solvent properties required for solubility. This provides a template to choose from a range of potential nanotube solvents, opening up an array of solution based experimental and processing procedures.

Stable dispersions of SWNTs suspended using SDBS in water were produced using a similar sonication/dilution/mild-centrifuge preparation scheme to the two phase media described previously. The SWNTs were found to be in the form of individuals and small bundles with no aggregates. This has been achieved without the need for ultracentrifugation at nanotube concentrations of up to 0.28 mg/mL. An analogous characterisation of these dispersions to those of NMP was carried out: the concentration dependence of the bundle statistics measured for the SDBS dispersions were similar to those for solvents such as NMP. However, the big difference was that, for SDBS dispersions, similar results, in terms of dispersion quality, were obtained at significantly

higher concentrations. This meant that smaller bundle diameters and hence larger number densities of bundles can be attained at a given concentration in SDBS compared to NMP.

Whilst carrying out the thermodynamic investigations of SWNTs in various solvents, a large list of previously unknown solvents for debundling SWNTs was found. These solvents are currently the subject of a further study[1]. The dispersive capability of the six most effective solvents is being investigated thoroughly with AFM and IRPL. It is known that the interaction between each of these solvents and SWNTs will differ slightly and so a crucial aspect of this study is to ascertain if there is any selective debundling (i.e. (n,m) type or nanotube diameter) from using any of these solvents. IRPL will outline any selective dispersion for semiconducting SWNTs. In order to quantify any differences in the debundling rates of the various metallic tubes, Raman spectroscopy could be employed to observe dispersed individual nanotubes giving a fuller picture to any selective debundling. Similarly, the six optimum surfactants for the dispersion of SWNTs, chosen from an extensive list constructed from relevant literature are being characterised with a view to determine if there is selective dispersion[1]. Initial results from this work have shown a common liquid soap to be an excellent dispersant. Coupled with the fact that this soap forms stable bubbles it is hoped that films of dispersed SWNTs can be transferred to various substrates. Furthermore, a dispersion study of functionalised SWNTs, commonly used in SWNT composites is being carried out in this laboratory[1]. This study is based on the methods described in this thesis, where the best solvents found are characterised by Hildebrand solubility parameters close to the various functional groups of the functionalised SWNTs.

As a result of the work carried out in this group, and the other relevant literature, NMP remains the best dispersant of SWNTs in a two phase media, thus making it an attractive candidate for those interested in making composites based on debundled SWNTs. However, the boiling point of NMP is $\approx 200°c$, making it quite restrictive for such composite experiments. The possibility of using solvent blends to ascertain the optimum solvent surface energy for dispersion, with the lowest possible boiling point is something that this group wish to investigate in the near future.

The methods described in this thesis for preparing the various dispersions and solutions of SWNTs in various media has been utilised by others both at this laboratory and elsewhere. Debundling by dilution has been demonstrated for SWNTs in bio-dispersants[2-4]. This affirms the robust nature of this technique. It is hoped that this technique can be extended to inorganic nanotubes in the near future. One of the most effective ways of transferring the properties of debundled SWNTs to a macro scale has

been the production of 'bucky papers' – a free-standing film of nanotubes. Recent work in this group has investigated such films made from dispersions of nanotubes using the sonication/dilution/mild-centrifuge methodology described in this thesis. Structural factors affecting the conductivity of nanotube films have been examined[1]. Their findings include the fact that as the film porosity and mean bundle diameter increase, the conductivity falls. They demonstrate that the conductivity scales approximately with the number density of inter-nanotube junctions as calculated from the porosity and mean bundle size: these findings show the critical importance of dispersions rich in small bundles. This work is aimed at producing highly conductive transparent SWNT films – a significant road-block for many applications. The factors controlling the mechanical properties of such nanotube films have also received considerable attention at this laboratory[1]: this work shows the topological properties of the nanotube network to be the strongest controlling factors of their mechanical properties. The various mechanical properties of these films are found to scale with the number density of the inter-bundle junctions which in turn is related to the mean bundle diameter. Small changes in the mean bundle diameter are shown to have dramatic consequences on the mechanical properties of the films.

To reiterate, repeatable and accessible methods for the exfoliation of SWNTs in various media have been presented. A solid understanding of the thermodynamics of such mixtures has shown the criteria for the solubilisation of such macromolecules in regular solvents. These findings have now been employed elsewhere in composites requiring high populations of debundled SWNTs, with a noticeable enhancement in their properties. It is hoped that this will continue and that newer, more prescriptive, methods of debundling will result from the findings of this thesis.

References

1. In Preparation.
2. Nicolosi, V., Vengust, D., Mihailovic, D., Blau, W. J. & Coleman, J. N. Debundling by dilution: Observation of significant populations of individual MoSI nanowires in high concentration dispersions. Chemical Physics Letters 425, 89-93 (2006).
3. Nicolosi, V., Cathcart, H., Dalton, A. B., Dieckmann, G. R. & Coleman, J. N. Spontaneous Exfoliation of Single Walled Carbon Nanotubes Dispersed Using Synthetic Peptides. In Preparation (In Prep).
4. Cathcart, H. et al. Spontaneous Debundling of Single-Walled Carbon Nanotubes in DNA-Based Dispersions. J. Phys. Chem. C 111, 66-74 (2007).

Chapter 9

Appendix

9.1 Colloidal Dispersions[1, 2]

A colloidal dispersion is a heterogeneous system in which particles of solid or droplets of liquids with dimensions of the order of 10μm or less are dispersed in a liquid medium. Familiar examples include paints, ink, mayonnaise, and milk. One of the defining characteristics of a colloidal dispersion is the extremely high area of interface: associated with this is a substantial amount of interfacial energy and thus the question arises as to why the dispersed particles don't combine to form larger aggregates and reduce this interfacial energy. To that end, understanding the stability of colloidal dispersions is critical. A delicate balance between gravity, Brownian motion, electrostatic forces, and others combine to result in such dispersions.

The motion observed in a dilute suspension of colloidal spheres can be described by Brownian motion - a phenomenon used to describe atoms and molecules in constant thermal motion. This motion is seen to have the character of a random walk: here if the displacement vector after time t, is $\mathbf{R}(t)$, then

$$\left\langle \left(\mathbf{R}(t) \right)^2 \right\rangle = \alpha t \tag{9.1}$$

Where the constant α is found to be related to the diffusion coefficient, D. Stokes and Einstein described the diffusion coefficient as

$$D = \frac{k_B T}{6\pi\eta a} \tag{9.2}$$

for a sphere of radius a in a liquid of viscosity η, where k_B is the Boltzmann constant, and T the temperature. This relation is often used to determine the size of unknown colloidal particles, where the diffusion coefficient can be measured from dynamic light scattering.

Associated with the large surface areas observed in colloidal systems is an energy whose origin lies in the fundamental forces between the atoms or molecules that constitute the dispersed phase. Typical interfacial energies between the particles are generally orders of magnitude higher than the value of $k_B T$ at room temperature. Thus, other forces must be acting between the particles preventing them from aggregating. All such forces in colloidal systems are fundamentally electrostatic in nature but the manifestation of these forces can be dramatically different.

Perhaps the most obvious force is the van der Waals force. Arising from the interaction between fluctuating dipoles between two atoms, this is an attractive force seen for atoms or molecules even when they are uncharged and have no dipole moment associated with them. Extending this, when two surfaces interact, there is a resultant force arising between the mutual interactions of all the pairs of molecules on the opposite surfaces. The potential of such an interaction can be expressed as

$$V(r) = -\frac{3}{4}\left(\frac{1}{4\pi\varepsilon_0}\right)^2 \frac{\alpha^2}{r^6}\hbar\omega \qquad (9.3)$$

where $V(r)$ varies as the inverse sixth power of the separation, r. α is the polarisability, and $\hbar\omega$ is the ionization energy. This can be extended from a knowledge of the forces between two atoms to the total force between two macroscopic bodies: the simplest approach simply summing the interactions between all pairs of atoms in each of the bodies.

One important aspect of van der Waals forces between bodies is their magnitude. When moving from the micro scale to the macro we can simply sum the forces. This means that even though between two individual atoms the force is relatively weak, between larger bodies the force is very strong. If two macroscopic bodies can be brought together close enough to be approaching the atomic scale over significant areas, they will stick together quite strongly. In practice we do not observe this for most macroscopic solids, because their surfaces are too rough to attain such contact. This accounts for the attractive van der Waals forces that cause single walled carbon nanotubes to bundle so strongly.

Another force to be considered is electrostatic double layer forces. Many surfaces are charged, and so one may expect electrostatic interactions to be important in determining the forces between colloidal objects with charged surfaces. However, when the objects are suspended in water, dissolved ions are always present and thus the interaction of the charged bodies with the ions profoundly changes the nature of the electrostatic interaction. Consequently, electrostatic interactions are screened by the dissolved ions – the screened Coulombic interaction is seen to decay exponentially in

strength with distance. If we consider a surface that is ionised, overall charge neutrality is maintained by a layer of counterions which are attracted to the surface by the electrostatic field. If two such surfaces are brought together, we would expect a repulsive force to arise: the source of this repulsion is however, not a direct effect of electrostatics. The combination of the charged surface and the attracted counterions must be overall charge neutral. Instead the repulsive force is due to excess osmotic pressure of the counterions in the gap between the two surfaces.

The stabilisation of colloidal particles with grafted polymer layers is seen to lead to another repulsive force. Polymers can be attached chemically or by physical interactions. The associated polymer is solvent friendly and this stabilises the colloidal particle in the solvent. Furthermore, when two such grafter colloids come close to one another the local concentration of polymer within the gap between them rises. This leads to an excess in osmotic pressure thus repelling the two colloids.

Finally, we consider the attractive forces caused by depletion interactions. Such interactions occur when the dispersion contains, in addition to the suspended particles, other particles of intermediate size that do not bind to the colloids. As a consequence of their inability to bind to the colloid a depletion layer is formed around the colloid. When the depletion zones of two such colloids meet, there is a net attraction between the particles, once more due to unbalanced osmotic pressure.

As stated, a colloidal dispersion can be considered as a system consisting of small particles dispersed in some continuous fluid. These particles are found to be undergoing Brownian motion, and thus will be colliding with one another remaining as individual particles only if those collisions do not result in permanent associations. Thus for lyophobic (solvent hating) colloidal systems, where the free energy of the system is lowest when the particles are all condensed together in one large lump, the particles can remain as individual blocks for an appreciable time only if some mechanism prevents aggregation during collision, by the processes described above.

References

1.   Hunter, R. J. Foundations of Colloid Science (Oxford Universtiy Press, Oxford, New York, 2001).
2.   Jones, R. A. L. Soft Condensed Matter (Oxford University Press, Oxford, New York, 2002).

9.2 List of Publications

Giordani, S.[1], Bergin, S. D.[1], Nicolosi, V.[1], Lebedkin, S.[2], Kappes, M. M.[2], Blau,W.J.[1], Coleman, J.N.[1] *Debundling of single-walled nanotubes by dilution: Observation of large populations of individual nanotubes in amide solvent dispersions.* Journal of Physical Chemistry B 110, 15708 – 12718 (2006).

Giordani, S., Bergin, S. D., Nicolosi, V., Lebedkin, S., Kappes, M. M., Blau,W.J., Coleman, J. N. *Fabrication of stable dispersions containing up to 70% individual carbon nanotubes in a common organic solvent.* Physica Status Solidi B-Basic Solid State Physics 243, 3058 – 3062 (2006).

Bergin, S.D., Nicolosi, V., Giordani, S., de Gromard, A.[1], Carpenter, L.[1,6], Blau, W.J., Coleman, J.N. *Exfoliation in Ecstasy: Liquid crystal formation and chirality dependent debundling observed for single wall nanotubes dispersed in the liquid drug γ-Butyrolactone.* Nanotechnology, 18, 45 (2007).

Bergin, S.D., Nicolosi,V., Streich, P.[3], Giordani, S., Sun, Z.[1], Windle, A.H.[4], Ryan, P.[5], Nirmalraj, P.P.N.[5], Wang, Z.T.[4], Carpenter, L.[6], Blau, W.J., Boland J.J.[4], Hamilton J.P.[3], Coleman J.N. *Towards Solutions of SWNT in Common Solvents.* Advanced Materials, In Press (2008).

Bergin, S.D., Nicolosi, V., Cathcart, H.[1], Lotya, M.[1], Rickard, D.[1], Sun, Z., Blau, W.J., Coleman, J.N. *Large populations of individual SWNT in surfactant based dispersions without the need for ultracentrifugation.* Journal of Physical Chemistry C, 112, 4, 972-977 (2008).

Amiran, J., Nicolosi, V., Bergin, S.D., Khan, U., Lyons, P.E., Coleman, J.N. *High quality dispersions of functionalised single walled nanotubes at high concentrations.* Journal of Physical Chemistry C, 112, 10, 3519-3524 (2008).

1   School of Physics, Trinity College Dublin, University of Dublin, Dublin 2, Ireland

2   Universität Karlsruhe, Institut für Physikalische Chemie, 76128 Karlsruhe, Germany

3   Department of Chemistry and Engineering Physics, University of Wisconsin – Platteville, Platteville, WI 53818, USA

4   Department of Materials Science and Metallurgy, University of Cambridge, Pembroke Street, Cambridge, CB2 3QZ, UK

5   School of Chemistry, Trinity College Dublin, University of Dublin, Dublin 2, Ireland

6   Dow Corning Corporation, 3901 S. Saginaw Rd, Midland, MI 48640, USA